August 2018

Graphene/P(VDF-TrFE) Heterojunction Based Wearable Sensors with Integrated Piezoelectric Energy Harvester

Soaram Kim
Clemson University, soaramk@clemson.edu

GRAPHENE/P(VDF-TrFE) HETEROJUNCTION BASED WEARABLE SENSORS WITH INTEGRATED PIEZOELECTRIC ENERGY HARVESTER

A Dissertation
Presented to
the Graduate School of
Clemson University

In Partial Fulfillment
of the Requirements for the Degree
Doctor of Philosophy
Electrical Engineering

---

by
Soaram Kim
August 2018

Accepted by:
Dr. Goutam Koley, Committee Chair
Dr. William Rod Harrell
Dr. Pingshan Wang
Dr. Apparao M. Rao

ABSTRACT

Graphene, with its outstanding material properties, including high carrier mobility, atomically thin nature, and ability to tolerate mechanical deformation related strain up to 20% before breaking, make it very attractive for developing highly sensitive and conformable strain/pressure sensor for wearable electronics. Unfortunately, graphene by itself is not piezoresistive, so developing a strain sensor utilizing just graphene is challenging. Fortunately, graphene synthesized on Cu foil can be transferred to arbitrary substrates (preserving its high quality), including flexible polymer substrates, which will allow the overall flexibility and conformability of the sensing element, to be maintained. Furthermore, a graphene/polymer based sensor devices can be easily patterned into an array over dimensions reaching several feet, taking advantage of large area synthesis of graphene, which will make the ultimate sensor very inexpensive. If a piezo-electric polymer, such as P(VDF-TrFE), is chosen to form a heterojunction with graphene, it will strongly affect the carrier density in graphene, due to the fixed charge developing on its surface under strain or pressure. Taking advantage of the high carrier mobility in graphene, such a charge change can result in very high sensitivity to pressure and strain. Hence, these features, coupled with the flexible nature of the device and ease of fabrication, make it a very attractive candidate for use in the growing wearable technology market, especially biomedical applications and smart health monitoring system as well as virtual reality sensors.

In this dissertation, various unique properties of graphene and P(VDF-TrFE), and their current applications and trends are discussed in chapter 1. Additionally, synthesis of

graphene and P(VDF-TrFE) and their characterizations by various techniques are investigated in chapter 2. Based on piezoelectric property of P(VDF-TrFE), a highly flexible energy harvesters on PDMS as well as PET substrates have been developed and demonstrated their performances in chapter 3. As follow-up research, graphene/P(VDF-TrFE) heterojunction based wearable sensors with integrated piezoelectric energy harvester on flexible substrates have also been fabricated and demonstrated for practical wearable application in chapter 4. Finally, major findings and future directions of the project are discussed in chapter 5.

DEDICATION

I dedicate this dissertation to my beloved mother and younger brother who supported and encouraged me to pursue my doctoral program.

ACKNOWLEDGMENTS

I would like to express the deepest appreciation to my advisor Dr. Goutam Koley for the continuous support of my doctoral program, for his patience, motivation, and immense knowledge. His guidance encouraged me in all the time of research, and I could not have imagined finishing this dissertation without his guidance. I am also very thankful for giving me the opportunity to pursue my Ph.D with state of the art research, in the area of graphene, at Nanoscale Electronics and Sensors Laboratory as research assistant.

Beside my advisor, I would like to thank the rest of my Ph.D committee: Dr. William Rod Harrell, Dr. Pingshan Wang, and Dr. Apparao M. Rao, for their insightful comments and encouragement. I remember the wonderful time I had when I took classes in Physics of Semiconductor Devices by Dr. Harrell, and interesting questions regarding my research area, which incented me to widen my research from various perspectives, we would have in classroom and his office hours. I would like to thank Dr. Wang, who generously allowed me to use his lab facilities such as wire bonding machine, and high performance computer resource for simulations. I would also like to express my graditude to Dr. Rao who gave me the opportunity to collaborate with Dr. Yongchang Dong for energy harvesting research, COMSOL simulations, and Raman spectrascopy, which helped achieve successful publications.

I thank my labmates, Sean Gorman, Ferhat Bayram, Digangana Khan, Md Maksudul Hossain and Robert Irvine, in for the discussions, for the sleepless nights we were working together before deadlines, and for all the fun we have had in the last three

years. My success at research would not have been possible without their help and support.

Last but not least, I would like to thank my family: my beloved mother and younger brother for supporting and encouraging me all the time throughout my doctoral program and my life in general.

TABLE OF CONTENTS

Page

Table of Contents (continued) Page

LIST OF TABLES

LIST OF FIGURES

List of Figures (continued)

Figure Page

List of Figures (continued)

Figure Page

List of Figures (continued)

List of Figures (continued)

CHAPTER ONE

INTRODUCTION

1.1 Graphene

Graphene has attracted tremendous research interest in transparent electronics [1], flexible electronics [2], field effect transistor [3], chemi-diode [4], and high speed and/or frequency devices [5] since the graphene was discovered by Novoselove et al. [6] (2004), and the discovery was led to a Nobel Prize in physics (2010). The graphene, with its outstanding material properties, including high carrier mobility [7], atomically thin nature [8], high thermal conductivity [9], high optical transparency in the visible range [10], and ability to tolerate mechanical deformation related strain up to 20% before breaking [11], is a purely two dimensional (2D) material with an arranged hexagonal lattice of carbon atoms (C-C bond length is 1.42 Å) as shown in Fig. 1.1. In addition, it can be formed into wrap in 0D as fullerene molecules, roll in 1D as carbon nanotubes, and 3D as pyrolytic carbon [12]. All these structure have superior and unique optical, mechanical, magnetic, and electrical properties, making them a strong candidate for future nanotechnology. Another part of advantage for graphene with unique properties is inexpensive process of synthesizing high quality single or multi-layer graphene by mechanical exfoliation [6] or chemical vapor deposition (CVD) [13]. In this chapter, the electrical, optical, mechanical properties of graphene, and its applications will be introduced.

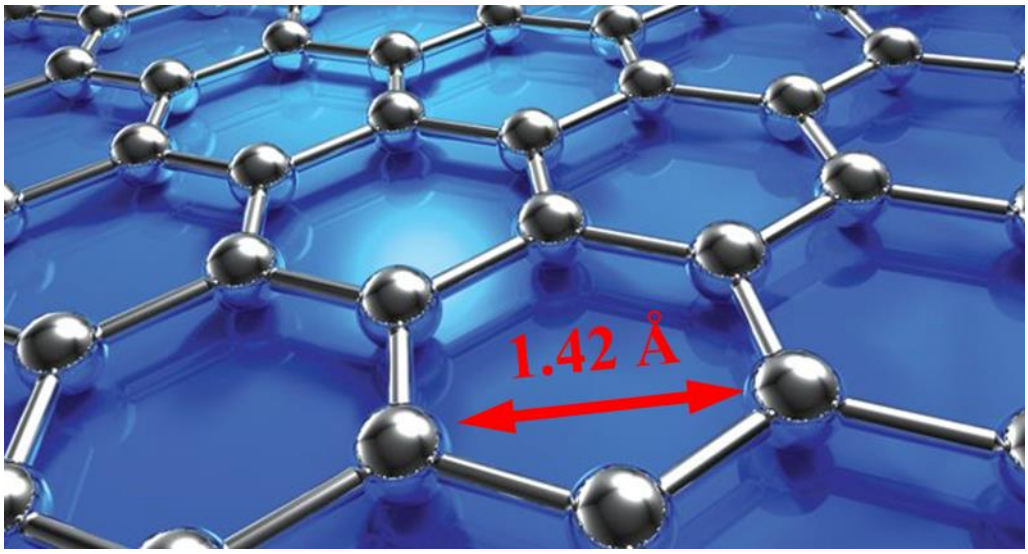

Figure 1.1 Schematic of periodic repetition of hexagonal unit resulting in 2D honeycomb structure of graphene [14].

1.1.1 Electrical properties

The hexagonal lattice of carbon atoms for graphene apart from its 3 nearest neighbors in a plane and shares a sp^2 hybridized σ bond with them, the forth orbital (p_z, single electron) is in z direction which perpendicular to the graphene plane and the p_z electrons from each carbon atom hybridize to form π and π^* bands. These bands are responsible for most of the electronic properties of graphene [15].

Figure 1.2 shows the schematic of (a) honeycomb lattice of graphene and (b) Brillouin zone. The basis of unit cell consists of two atoms (i.e. A and B), which the two interpenetrating triangular lattice that make up the honeycomb lattice. The lattice and reciprocal lattice vectors are given by Equation 1.1 and 1.2, respectively.

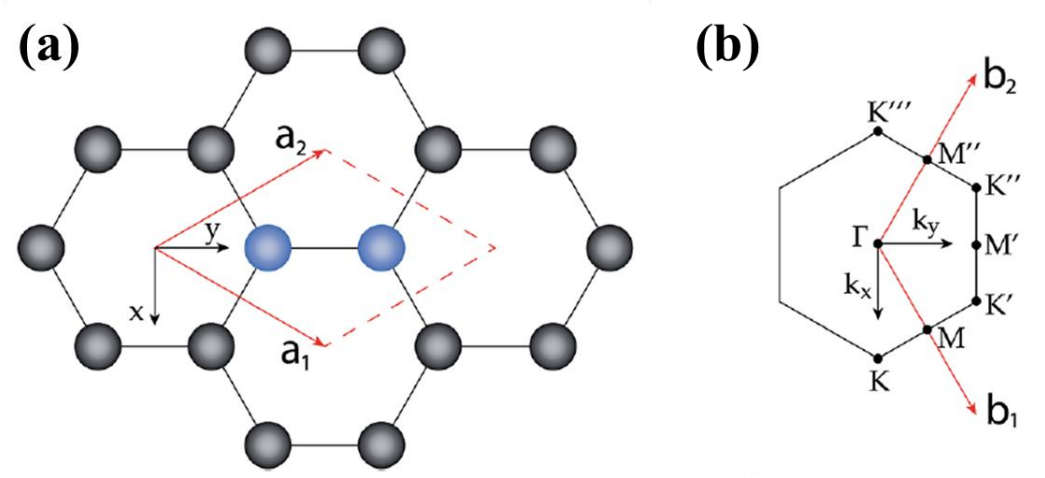

Figure 1.2 Schematic of (a) Honeycomb lattice, and (b) its first Brillouin zone. The lattice vectors are denoted by a_1 and a_2. The reciprocal lattice vectors are represented by b_1 and b_2. The parallelogram formed by a_1 and a_2 represents the unit cell [16].

$$\boldsymbol{a_1} = \frac{a}{2}(3, \sqrt{3}),\ \boldsymbol{a_2} = \frac{a}{2}(3, -\sqrt{3}) \tag{1.1}$$

$$\boldsymbol{b_1} = \frac{2\pi}{3a}(1, \sqrt{3}),\ \boldsymbol{b_2} = \frac{2\pi}{3a}(1, -\sqrt{3}) \tag{1.2}$$

The theoretical investigations on the band structure of graphene were first determined by Wallace in 1947 [17] who reported tight binding model or linear combination of atomic orbitals.

In addition, it is important to consider the interaction of carbon atoms to nearest and next nearest neighboring carbon atoms to obtain dispersion relationship or band structure. The nearest neighbor distance a = 142 pm, the lattice constant is $\sqrt{3}$a (i.e., 246 pm), and the ***M*** (zone boundary) which is half the reciprocal lattice vectors ($\boldsymbol{b_1}$ and $\boldsymbol{b_2}$) is $2\pi/3a$. The coordinates of ***K*** (corner point) are ($2\pi/3a$, $\pi/3\sqrt{3}a$) so that the distance from

the origin to $\boldsymbol{K}$ is $4\pi/(3\sqrt{3}a)$. We have $k_F = |K|$ and the Fermi wavelength $k_F = 2\pi/k_F = 3\sqrt{3}a/2 = 369$ pm since the conduction and valence bands touch at K. In order to express the conduction band and valence band touch each other at Dirac point at 6 places on the corner of a graphene's Brillouin zone referred as $\boldsymbol{K}$ and $\boldsymbol{K'}$ points with the following position vectors in the reciprocal space.

$$\boldsymbol{K} = \left(\frac{2\pi}{3a}, \frac{2\pi}{3\sqrt{3}a}\right), \ \boldsymbol{K'} = \left(\frac{2\pi}{3a}, -\frac{2\pi}{3\sqrt{3}a}\right) \tag{1.3}$$

The dispersion relation at K and K' points are given by the following equation.

$$E(\boldsymbol{k}) = \pm\hbar v_F |\boldsymbol{k}| = \pm v_F \sqrt{k_x^2 + k_y^2} \tag{1.4}$$

Where $v_F = 0.9 \times 10^6$ m/s which is Fermi velocity calculated by

$$v_F = \frac{3at}{2\hbar} \tag{1.5}$$

Therefore, charge particles (i.e., electrons and holes) close to Dirac point in graphene is called as Dirac fermions because electrons and hole move with v_F as Eq. 1.5 in the dispersion relationship at low energy points in reciprocal lattice space. Figure 1.3 shows energy bands in monolayer graphene describing the upper and lower bands were derived from the $2p_z$ orbital of carbon.

In general, the mobility is strongly dependent on the quality of graphene and corresponding target substrates because of scattering mechanism in graphene. The main scattering mechanism in graphene are short range scattering, Coulomb scattering, and phonon scattering, resulting from defects in graphene (i.e., vacancies and cracks). Moreover, surface polar phonons and defects are main reason of scattering mechanism for graphene at the room temperature. Up to date, there are lots of researchers have been

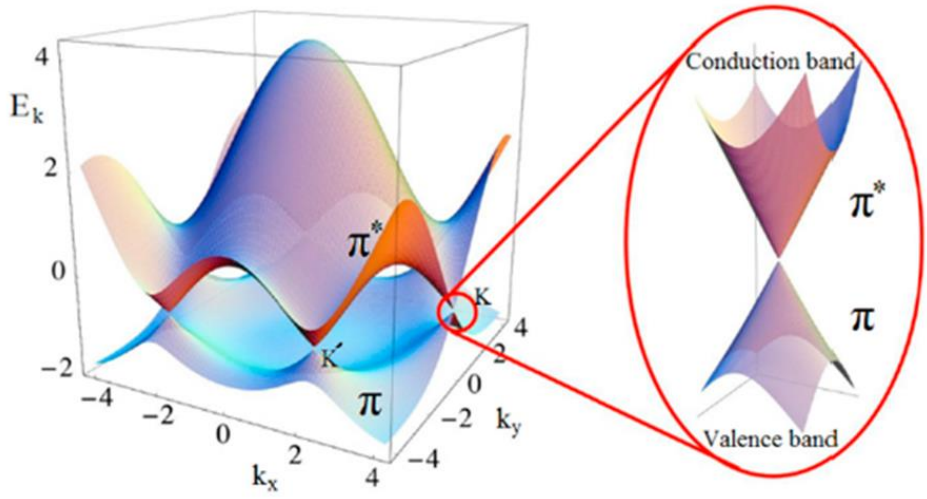

Figure 1.3 Schematic of energy bands in monolayer graphene (π and π^* bands). The upper and lower bands are conduction and valence bands, respectively. The Dirac points are the linear energy dispersion, present near the neutral K, K'[15].

working on graphene and they have improved the quality and mobility of graphene. To the best of my knowledge, the graphene with hexagonal boron nitride has high carrier mobility and its maximum reported value is ~350,000 $cm^2V^{-1}s^{-1}$ [7], which is about 20 and 1.75 times higher than SiO_2 (10,000 to 15,000 $cm^2V^{-1}s^{-1}$) [18] and Si/SiO_2 (~200,000 $cm^2V^{-1}s^{-1}$) [19], respectively. In addition, graphene has high breakdown current density (10^8 A/cm^2) [20], which make the graphene a strong candidate for electronic devices with high current density, high speed and low power consumption.

1.1.2 Optical properties

Graphene also possesses high optical transmittance (~97% transmission of the visible light) [10]. This is because monolayer graphene has atomic layer thickness, which makes the graphene absorbing ~3% of visible light. It is notable that multilayer of graphene does not interact optically because of 2D electron gas (2DEG) properties, and the absorbance of multilayer of graphene is proportional to number of layers. In addition, in the ultraviolet and infrared region, the graphene absorb ~3% of electromagnetic spectrum compared to other transparent materials [21]. Therefore, the graphene with high transparency, high carrier mobility is a strong candidate for transparent electronics and solar cell.

1.1.3 Mechanical properties

Graphene has superior mechanical properties and been reported as one of the strongest materials in the world. The tensile strength of graphene is 200 times higher than steel, with a tensile modulus of 1 TPa [22]. The Young's modulus of graphene is about 700 ~ 1000 GPa. The graphene also has ability to tolerate mechanical deformation related strain up to 20% before breaking (breaking strength: 40 N/m) [11]. Moreover, the graphene is available to have suspended structure using its unique mechanical properties, which is different with bulk graphite. Hence, the graphene is suitable for nanoelectromechanical system (NEMS) and flexible electronics such as strain/pressure sensor and resonators.

1.1.4 Applications and trends

The unique electrical, optical, and mechanical properties of graphene combined with its cheap and easy synthesis allow the graphene to be used for applications in a variety of diverse areas such as optoelectronics, energy harvesting, flexible electronics, and NEMS, etc. Here, some of the applications of graphene are briefly discussed, and Figure 1.4 shows major graphene applications in a variety of diverse areas.

Transparent, conductive, and ultra-thin graphene films could be a candidate for window electrodes for optoelectronics such as solar cells [23]. Also, the graphene transparent electrode with high electrical conductivity can be used for energy harvester acoustic actuator [24] combined with piezoelectric properties materials such as P(VDF-TrFE). In addition, graphene has remarkably superior mechanical strength, which makes it suitable for flexible electronics such as strain/pressure sensor [25]. The graphene has an ability to be suspended over open cavities; it can be developed for NEMS based pressure sensor and high frequency resonator, etc [26]. Furthermore, there are plenty of other graphene applications such as batteries [27], ultracapacitors [28], chemical/biological sensors [29], and infrared photodetectors [30].

Although there are still challenges in the fabrication and transfer of large area graphene sheets that must be overcome to succeed in commercial and technological devices, graphene has enormous potential in a variety of diverse areas and the graphene will lead future technology after controlling and understanding the dependence of its unique properties reasonably.

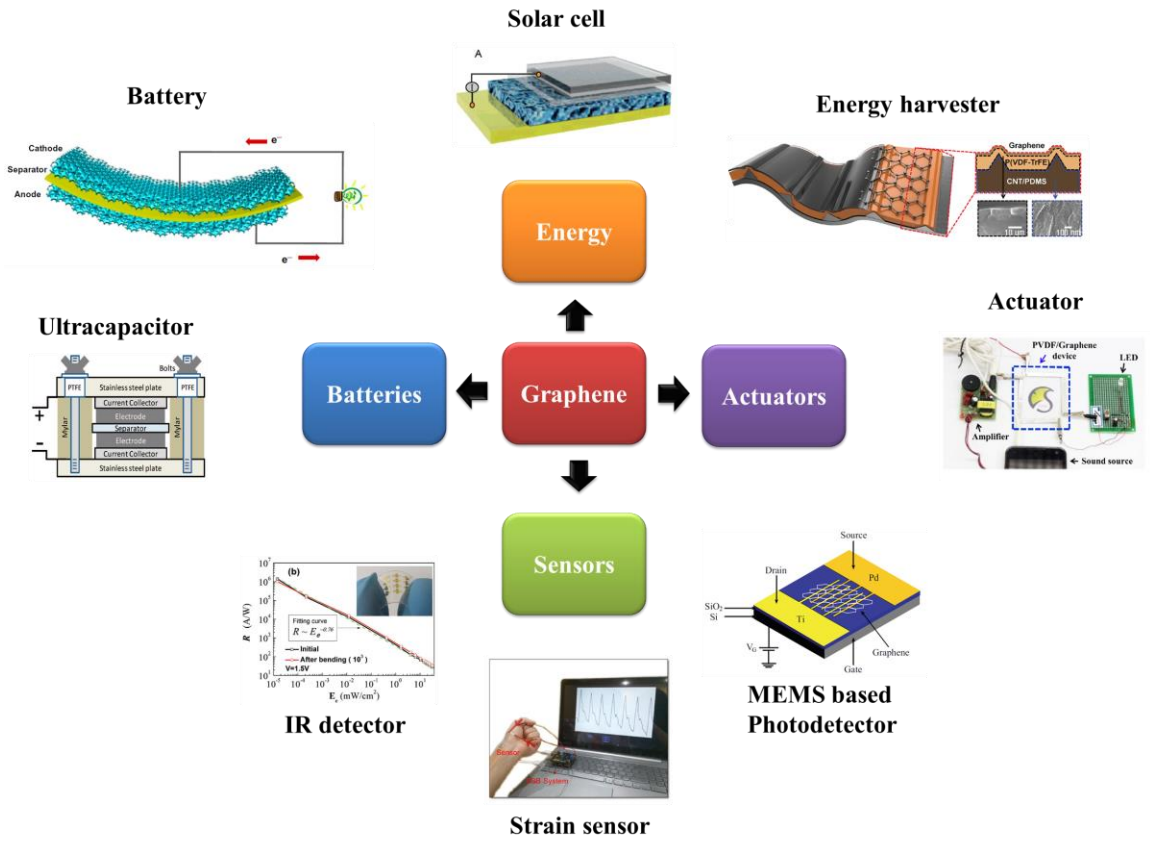

Figure 1.4 Overview of major graphene applications in a variety of diverse areas [23-30].

1.2 Poly(vinylidenefluoride-co-trifluoroethylene) P(VDF-TrFE)

P(VDF-TrFE) is ferroelectric polymer combined by varying the molar ratio of TrFE in proportion to PVDF, offers several advantages compared to PVDF, including higher piezoelectric coefficient [31] better crystallinity, higher remnant polarization, and higher temperature stability [32,33]. All ferroelectrics are also piezoelectrics due to crystal symmetry, and the ferroelectricity in P(VDF-TrFE) is caused by the dipoles that polarize spontaneously and align with external electric field. The P(VDF-TrFE), based on pure PVDF, has lots of benefits compared to other polymers and other piezoelectric

materials such as strong piezoelectric and pyroelectric properties, high mechanical flexibility, good chemical inertness, easy synthesis, fully biocompatibility, high dielectric strength, high rigidity, resists deformation, stability to radiation (UV, X-ray, Gamma), excellent electrical insulator, and high curie point [34-37]. This means that these superior properties are suitable for applications in a variety of diverse areas such as sensors (strain/pressure, temperature, ultrasound, infrared), speakers, memories, actuators, and energy harvesters, resulting from piezo- and pyroelectric responses. In this chapter, the ferroelectric, piezoelectric, pyroelectric properties of P(VDF-TrFE), and its applications will be introduced.

1.2.1 Ferroelectric and piezoelectric properties

The most important reason of the use of P(VDF-TrFE) is that pure PVDF as a ferroelectric material has severe weakness of phase transition, which PVDF does not easily crystallize into the ferroelectric β-phase without specialized processing such as uniaxial drawing. The first investigation of PVDF about net polarity was reported by several groups in the 1960's and 1970's [38-41], and the PVDF has chemical structure of ($-CH_2-CF_2-$) repeat units, which provide large chain flexibility. Furthermore, a piezoelectricity and pyroelectricity in PVDF was firstly discovered in 1969 and 1971 [42,43]. There has been a lot of research for the crystalline forms of PVDF and it was found that the PVDF has at least four different crystal phase such as α-phase, β-phase, γ-phase, and δ-phase with different molecular conformations and lattice parameters [40,41,44-50] as shown in Fig. 1.5. Among these phases, the β-phase possesses a

spontaneous lattice polarization resulting in observation of ferroelectricity in PVDF, which is the most interesting phase in several applications because of piezo- and pyro-electric properties. However, α-phase does not show a net lattice polarization due to its antiparallel chain arrangement (i.e., the dipole oppose each other, no piezoelectric properties) while γ-phase is intermediate between the α- and β-phase. Lastly, δ-phase of PVDF, which is a lack of study of δ-phase and difficult distinguishing its phase from the α-phase, is a polar version of the α-phase with the same unit cell (but a varying symmetry). The most common measurements of the different phases for PVDF are x-ray diffraction (XRD) or Fourier-transform infrared spectroscopy (FTIR), and they will be discussed in next chapter.

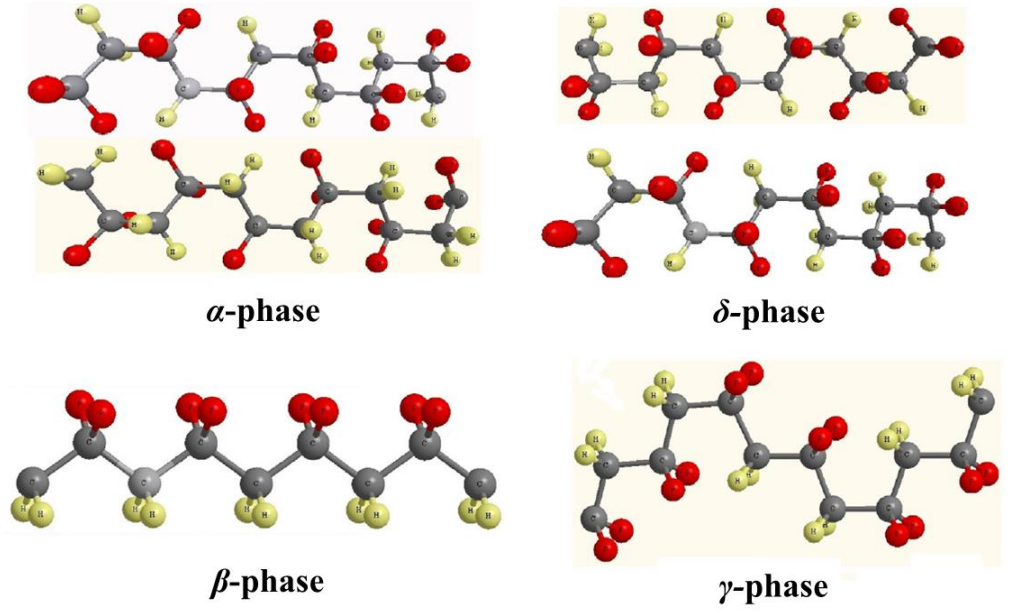

Figure 1.5 Schematic of crystalline α, β, γ, and δ conformations of PVDF [50].

Yadi et. al. [51] firstly reported phase transition in a polymeric materials and phase diagram for the compositions of P(VDF-TrFE) in the early 1980's. Since the 1980's there has been a plenty of research regarding the P(VDF-TrFE) [52-54], it has been found that the crystalline structure of P(VDF-TrFE) can be converted between the paraelectric and ferroelectric form with an external electric field or with a change in temperature (50~150 ^{o}C) while pure PVDF does not have a phase transition at temperature below that melt as shown in Fig. 1.6 [55]. Moreover, the size of the additional fluorine atom from TrFE make the copolymer of P(VDF-TrFE) crystallizing directly in beta phase, and thus the P(VDF-TrFE) can produce final structure from the solution without any extra processing [56]. The phase transition behavior and ferroelectric properties of P(VDF-TrFE) are strongly dependent on the ratio of TrFE content and the condition of synthesis [57]. The β-phase of P(VDF-TrFE) needs to be poled to obtain piezoelectric properties in films. This process includes applying a high external electric field (~100 MV/m) to the film in order to align dipoles in the same direction. However, the β-phase converts back to the more favorable α-phase with a hysteresis curve after polling is done. Figure 1.7 shows a typical P(VDF-TrFE) hysteresis curve. This curve exhibits a remnant polarization can be inverted for $[E]>E_C$ (coercive field) [55].

Piezoelectric energy harvesting is one of interest applications with P(VDF-TrFE) due to piezoelectric properties, thus it is important to know the piezoelectric properties of P(VDF-TrFE) with different ratio of TrFE content as shown in Table 1 [Piezotech ARKEMA].

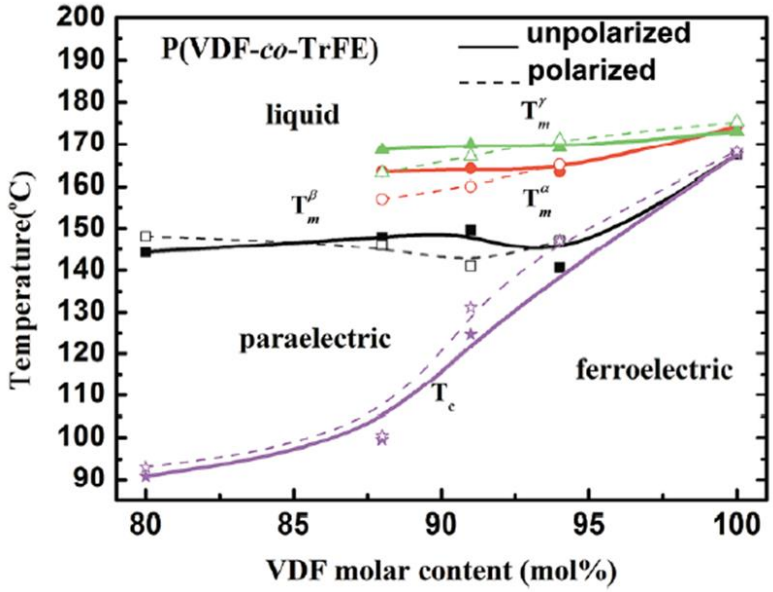

Figure 1.6 Phase diagram of P(VDF-TrFE) [55].

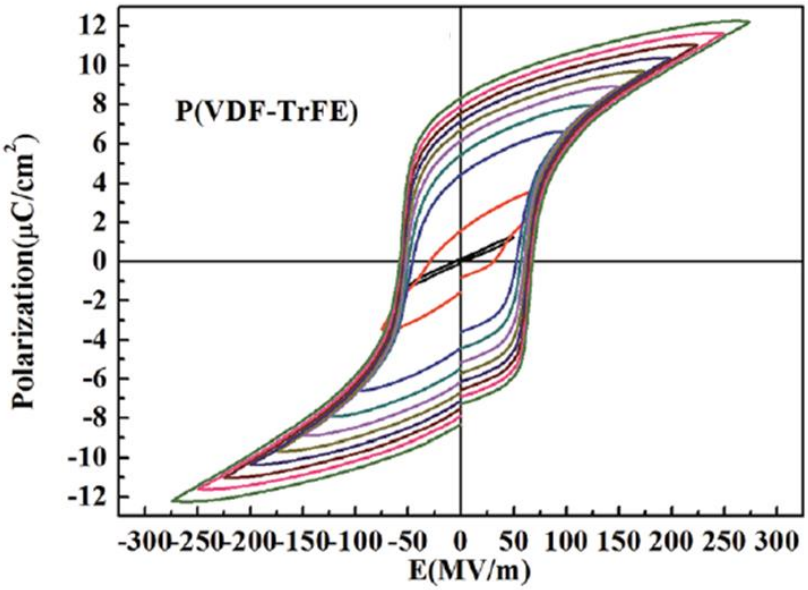

Figure 1.7 Polarization hysteresis loops at various electric field of P(VDF-TrFE) [55].

Table 1.1 Typical properties of the P(VDF-TrFE) with different ratio of TrFE content [Piezotech ARKEMA].

	Composition of %TrFE				
	20	25	30	45	50
	Thermal properties				
Melting T range (°C)	148-152	148-152	149-153	156-160	158-163
Curie T (°C)	131-141	112-123	96-106	57-62	58-63
Typical Annealing T (°C)	135	135	135	145	145
C_p (J/g/K)	1.3				
C_{pv}(J/cm^3/K)	2.3				
	Molar mass characteristics				
Mw range (10^3 g/mol)	400-530	370-530	380-540	350-550	350-550
	Dielectric properties				
ε_r	10-12			11-15	
Remnant polarization Pr (mC/m^2)	80	70	65	45	30
Coercive field (V/µm)	45	50	50	55	40
	Mechanical properties				
Young Modulus (Gpa)	0.8 – 1.2				
	Piezoelectric / Pyroelectric properties				
d_{33} (pC/N)	-24 to -30			-18 to -22	
Typical P_3 (µC/m^2/K)	-30			-50	

Furthermore, it is also possible to investigate expected value of deformation, applied mechanical stress, and generated voltage with different thickness of P(VDF-

TrFE) films using Table 1. The deformation (S_i) caused by the applied electric field can be calculated by Equation 1.6 as follows:

$$S_i = d_{3i} E = \frac{\Delta L}{L} \qquad i = 1,2,3 \tag{1.6}$$

where d_{3i} is the piezoelectric strain constant which is perpendicular direction with respect to the applied electric field. The applied mechanical stress and generated voltage can be calculated by Equation 1.7 as follows:

$$E = g_{ij} \sigma_i = \frac{V_0}{t} \qquad i \; and \; j = 1,2,3 \tag{1.7}$$

where E is the electric field output, g_{ij} is the piezoelectric voltage constant (Vm/Nm^2), σ_i is the applied mechanical stress (N/m^2), and V_0 is generated output voltage (V).

1.2.2 Pyroelectric properties

P(VDF-TrFE) also possess pyroelectric properties which can generate a certain voltage under the condition of fluctuations in thermal energy (i.e., temporal temperature changes), existing everywhere due to sun light and various heating/cooling sources. The pyroelectricity strongly depends on the change of spontaneous polarization which results in charges separation, and its coefficient could be described by Equation 1.8.

$$p_i = \frac{\partial P_{S,i}}{\partial T} \tag{1.8}$$

where p_i [C/m^2K] is the vector of pyroelectric coefficients. Although lots of energy harvesting systems such as piezoelectric, triboelectric, electrostatic, electromagnetic, and photovoltaic based devices have been tremendously researched and reported significant results [58-62], there is a lack of research on pyroelectric properties based energy

harvesting systems. The most interesting advantage of pyroelectric properties is that it can be used for multimodal energy harvesting applications in combinations with piezoelectric and triboelectric properties. Furthermore, pyroelectric properties are commonly used for infrared thermal imaging and uncooled based infrared radiation (IR) sensors.

1.2.3 Applications and trends

P(VDF-TrFE), with superior ferroelectric, piezoelectric, and pyroelectric properties, is a strong candidate for variety applications such as sensors (strain/pressure, temperature, ultrasound, infrared), speakers, memories, actuators, and energy harvesters etc. Here, some of the applications of P(VDF-TrFE) are briefly discussed, and Figure 1.8 shows major applications in a variety of diverse areas.

Bae et. al. [24] reported a flexible, transparent acoustic actuator and nanogenerator on graphene/P(VDF-TrFE)/graphene multilayer films. The acoustic actuator worked over a broad range of frequency, and the output voltage and the current density of the nanogenerator are estimated to be ~3 V and ~0.37 μAcm^{-2}, respectively, upon the application of pressure. It is notable that they demonstrated the possibility of rollable devices based on P(VDF-TrFE) film using highly transparency and mechanical flexibility. Lee et. al. demonstrated several types of P(VDF-TrFE) based nanogenerators (NG) such as micropatterned (i.e., trigonal and pyramid shape) based piezoelectric NG (output voltage: 4.4V, output current: 3.4 μA) [63], pyroelectric NG (output voltage: 2.5 V, output current density: 570 nA cm^{-2}) [64], and piezoelectric-pyroelectric hybrid NG

(output voltage:1.4 V, output current: 150 nA) [65]. It is interesting that P(VDF-TrFE) could be patterned by photolithography and have micropatterned which allow them to be highly sensitive self-powered pressure sensor as well. Another novelty of their work is that they fabricated piezoelectric-pyroelectric hybrid NG which can be attachable to human body.

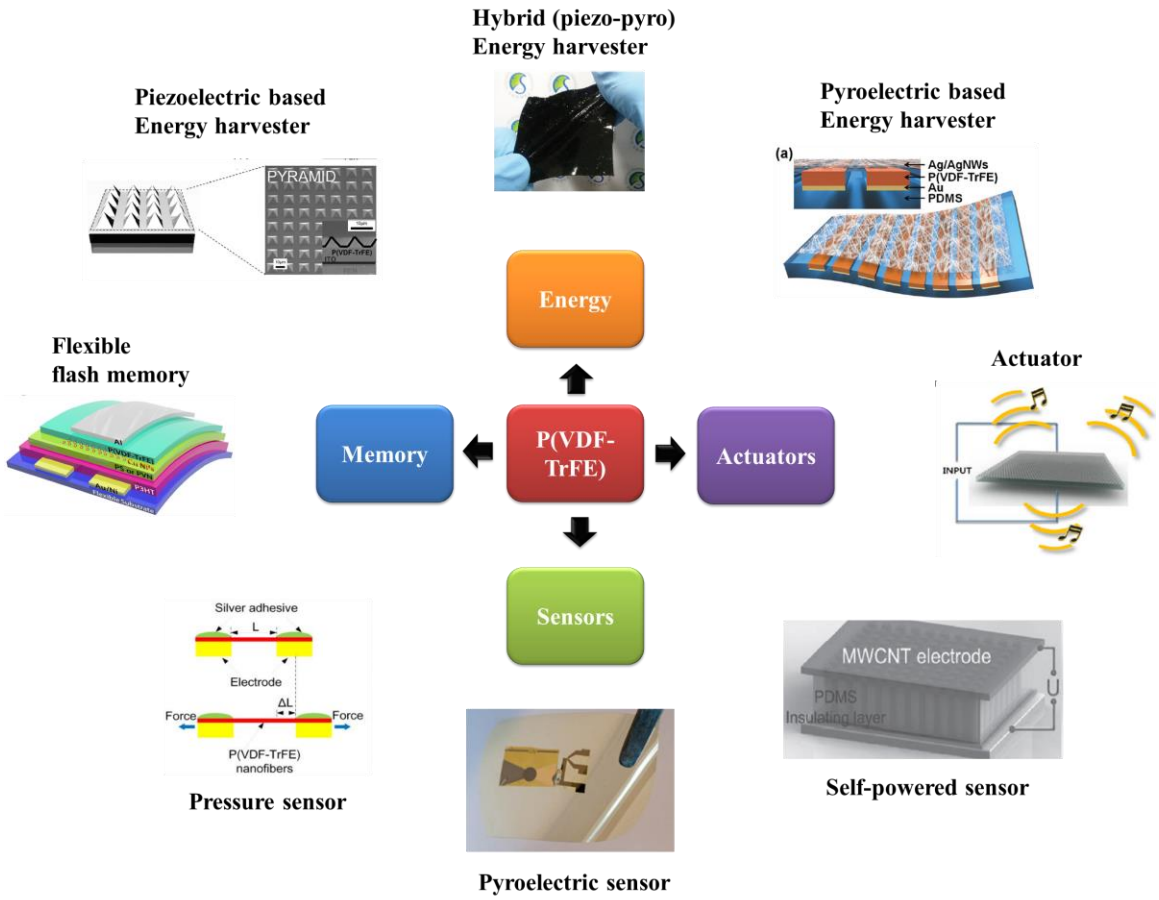

Figure 1.8 Overview of major P(VDF-TrFE) applications in a variety of diverse areas [24,63-72].

P(VDF-TrFE) is also good candidate for memory applications. Fujisaki et. al. [66] reported low-voltage operation of ferroelectric P(VDF-TrFE) capacitor. They fabricated

metal-ferroelectric-metal capacitor with thin film of P(VDF-TrFE) (60 nm) and demonstrated coercive voltage (V_C), coercive field (E_C), and remanent polarization (P_r) were 2.0 V, 33 V/μm, and 11.9 μC/cm^2, respectively. Also, Asadi et. al. [67] presented organic non-volatile memories from ferroelectric phase-separated blends. Measurements on pure P(VDF-TrFE) capacitors with a Sawyer-Tower circuit showed a E_C of 50 MV/m, and a remanent P_r of 60 mC/m^2.

Furthermore, P(VDF-TrFE) is able to be composite materials with other piezoelectric materials. Chen et. al. [68] fabricated self-powered flexible sensors using imprinted P(VDF-TrFE)/$BaTiO_3$ nanocomposite micropillars. The piezoelectric device exhibits enhanced voltage of 13.2 V and a current density of 0.33 μA/cm^2 with nanocomposite micropillars, which an enhancement by a factor of 7.3 relatives to the pristine P(VDF-TrFE) film. Additionally, the device can be applied as self-powered flexible sensor work in a noncontact mode for detecting air pressure and wearable sensors for detecting human vital signs (i.e., breath and heartbeat pulse). Wu et. al. [69] fabricated PZT/P(VDF-TrFE) composite film pyroelectric infrared sensor with patterned polyimide (PI) thermal isolation layer. Performance of the infrared sensor such as voltage responsivity (R_V), noise voltage (V_{noise}), noise equivalent power (NEP), detectivity (D^*), and thermal time constant of the sensor (τ_T) are 1.2×10^3 V/W, 1.25×10^{-6} VHz$^{1/2}$, 1.1×10^{-9} W, 1.9×10^8 cmHz$^{1/2}$W^{-1} at 137.3 Hz modulation frequency, and 15 ms, respectively.

CHAPTER TWO

SYNTHESIS OF GRAPHENE AND P(VDF-TRFE)

2.1 Synthesis of graphene

Since the first technique, i.e., mechanical exfoliation (also called scotch tape method), reported by Geim and Novoselove [73] to obtain graphene, there are broadly three methods such as epitaxial growth, chemical vapor deposition (CVD) growth, and reducing graphene oxide have been introduced to synthesize the graphene. The epitaxial and CVD growth methods have been used to synthesize large area and high quality of graphene, while reducing graphene oxide produce poor quality of graphene although it is available to synthesize large area of graphene. Table 2.1 and Figure 2.1 show comparison of different synthesis techniques of graphene. Here, some of the techniques for synthesis of graphene such as mechanical exfoliation and CVD growth are briefly discussed.

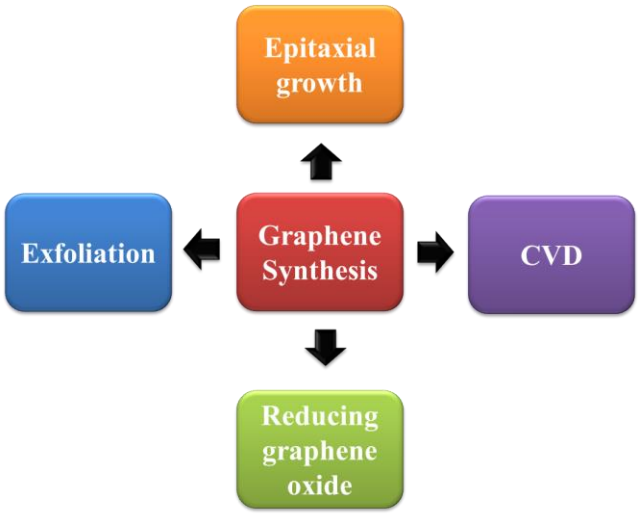

Figure 2.1 Various synthesis techniques of graphene

Table 2.1 Comparison of different synthesis techniques of graphene.

Technique	Advantage	Disadvantage
Epitaxial growth	High quality, Good uniformity, Synthesis of large area	Bad Transferability, Lattice mismatch, Lack of back gate
Chemical vapor deposition	High quality, Monolayer, Transferability, Synthesis of large area	High grain boundary, Hard to control number of graphene layer,
Reducing graphene oxide	Synthesis of large area	Bad quality, Hard to control number of graphene layer
Mechanical exfoliation	Easy process	Bad yield, Hard to control number of graphene layer

2.1.1 Mechanical exfoliation

Noveselov et. al. [73] reported mechanical exfoliation to obtain micron sized atom thick flakes of graphene from graphite using scotch tape as shown in Fig. 2.2. First of all, a piece of scotch tape is used to peel off a layer of graphite from the flat surface of highly ordered pyrolytic graphite. And then, another piece of scotch tape is used to remove a layer of graphite from the first tape. Next, new piece of scotch tape is used to remove a layer from the second piece of scotch tape repeatedly to further thin down the number of layers of graphite on the tape. Eventually, a single-, bi-, or few-layer of graphene can be obtained on the substrate. Although this mechanical exfoliation technique produces high quality of graphene flakes, it is not capable of large area synthesis of graphene unfortunately.

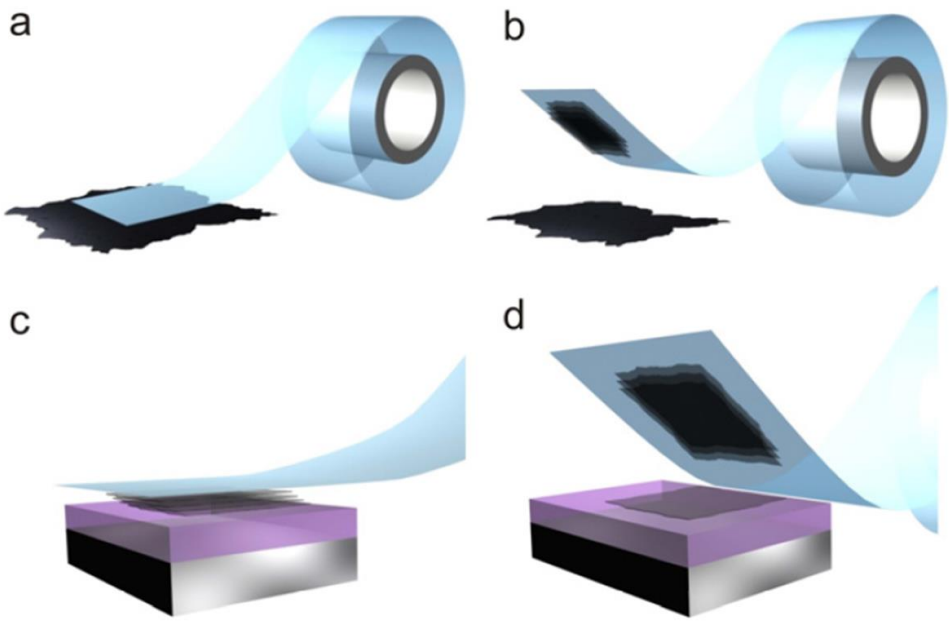

Figure 2.2 Mechanical exfoliation of graphene [73].

2.1.2 Chemical vapor deposition (CVD) growth

The chemical vapor deposition (CVD) involves the decomposition of hydrocarbons at high temperature, and the carbon from decomposed gasses gets adsorb on transition metal and synthesize the large area of graphene with high quality. Ruoff et. al. [74] reported CVD growth technique to synthesize large area of high quality graphene on Cu foils unlike mechanical exfoliation method. Since then, CVD growth technique reported various transition metal have been used, but Cu and Ni have been studied widely [1,74-76]. However, synthesizing graphene on Cu foil is better option for thinner graphene compared to Ni because carbon is less soluble in it which is reported by Li et. al. [77]. They used carbon isotope labeling in conjunction with Raman spectroscopic mapping to track carbon during the CVD growth process on Cu and Ni. They found the solubility of

C in Cu is much lower than that in Ni, which means that the source (CH_4) is catalytically decomposed on the Cu surface with minimal carbon diffusion into the Cu since only a small amount of carbon can be dissolved in Cu. In contrast, Ni can dissolve more carbon atoms and hence it is difficult to get uniform graphene films due to precipitation of extra C during the cool down.

A typical CVD growth includes three steps: (i) Annealing of the metal film, (ii) Exposure to CH_4, and (iii) Cooling of the metallic film. To be specific, first of all, after pursing a quartz tube reactor, the catalyst film is annealed at high temperature between 900 ^oC and 1000 ^oC under the gas mixtures of Ar and H_2 to induce not only recrystallization on the film but also a preferential texture of the film. After the annealing the diluted CH_4, main source to synthesize graphene, expose to the surface of metal film. They hydrocarbon gas can also be introduced with a mixture of Ar and H_2. At this process, methane is decomposed catalytically on the surface of the metal film to synthesize carbon atoms on the film, and its reaction can be described the Equation 2.1.

$$CH_4 \leftrightarrow 2H_2(g) + C(s) \tag{2.1}$$

Additionally, other hydrocarbons such as C_2H_4 (ethylene) and C_2H_2 (acetylene) may involve the transitional steps for the decomposition. And then, the carbon from decomposed gasses diffuses to the surface of metal film and adsorb on the film. Lastly, the sample should be cooling to promote the separation of C stored inside the film, and the carbon isolated to the surface initiating the growth of monolayer graphene or few layer graphene.

2.1.3 Process of CVD growth graphene

In our group, we are able to grow our own high quality of graphene on Cu foil by CVD growth technique (see Fig. 2.3) and it can be transferred to various substrates for many different device fabrications. Figure 2.4 shows the process of CVD graphene growth on Cu foil. Frist of all, the Cu foil (25 μm thick, 99.999%, Alfa Aesar) was cleaned by ultra-sonication for 2 min in acetone to remove organic particles on surface, and then rinsed it by isopropanol (IPA). Next, the diluted nitric acid (HNO_3) (30%) was used for 60 s for flattening Cu and oxidizing. After drying with N_2 gun, the Cu foil was sonicated for 10 min with acetic acid to remove the existing copper oxides such as CuO and Cu_2O, which were present in rolled Cu foils. Lastly, the Cu foil was rinsed by IPA to remove residue of chemical particles on the surface, and dried with N_2 gun again. Figure 2.5 shows the schematic of all cleaning process of Cu foil.

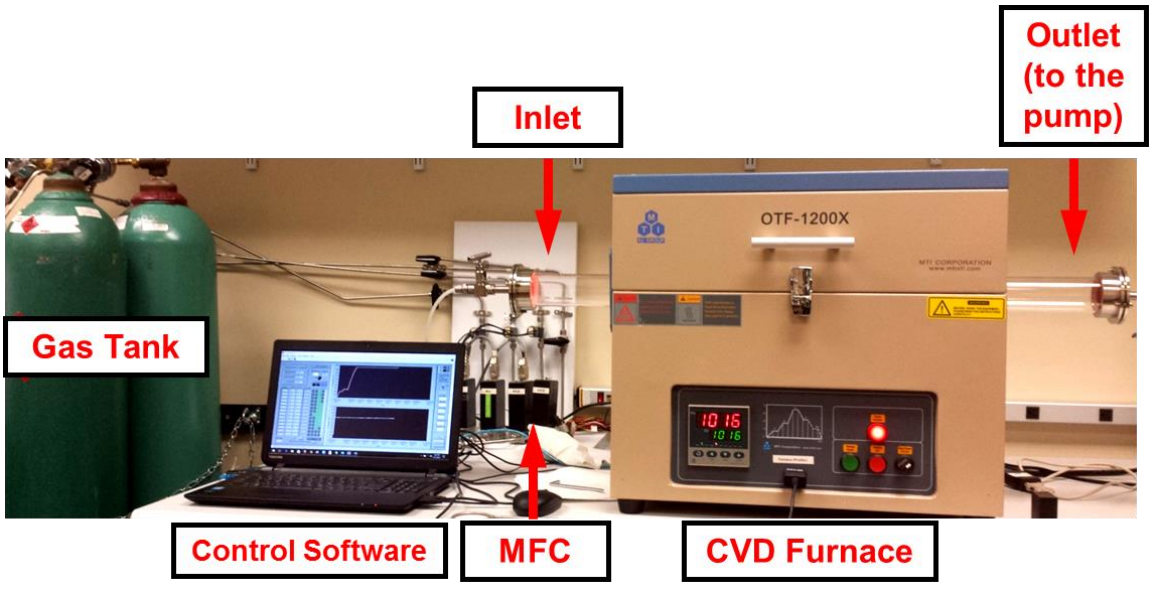

Figure 2.3 CVD growth system.

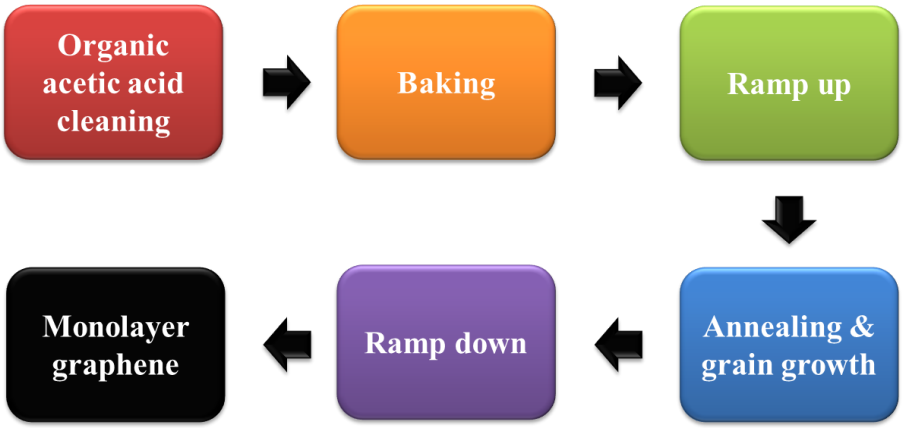

Figure 2.4 Process of CVD graphene growth.

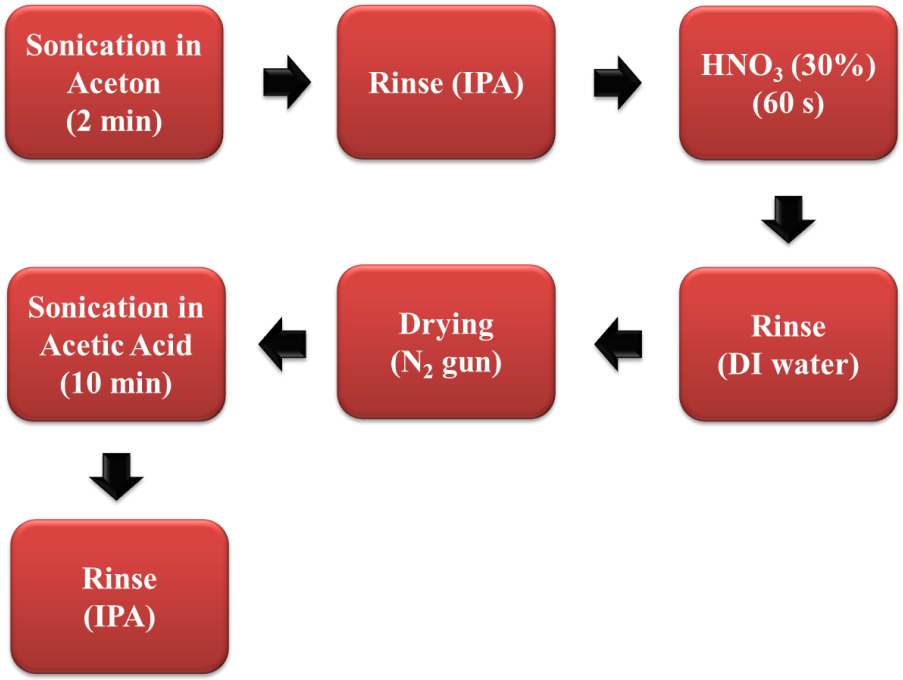

Figure 2.5 Cleaning process of Cu foil.

After cleaning process of Cu foil, it is placed into quartz chamber (1/4" size) in Ar atmosphere. Next, the temperature of quartz chamber in CVD system is increased up to

250 ^{o}C for baking in Ar (1000 sccm) atmosphere. H_2 (200 sccm) is flown for 2 h after increasing the temperature from 250 ^{o}C to 1000 ^{o}C in order to anneal Cu foil to increase its crystalline quality and remove any remaining and newly formed oxide on the surface. After that, the temperature of chamber is increased up to 1035^{o}C to start actual growth of graphene in presence of CH_4 (50 sccm). After 20 min of growth, the ramp is turned off to cool down naturally until the temperature of chamber reached 100 ^{o}C. Then, the lid of furnace in CVD system is opened to expedite the cooling process. Finally, we can get high quality of monolayer or few layer graphene by CVD technique. The optimized process parameters and sequence of steps for CVD growth graphene as shown in Fig. 2.6. The CVD growth system is a semi-automated with LabVIEW software. For three gasses such as CH_4, H_2, and Ar are controlled by mass flow controller (MFC), its valve are opened by manually and controlled by LabVIEW. To monitor the pressure of the CVD growth system, a Pirani gauge (901P Micro Pirani/Piezo Loadlock Vacuum Transducer) are placed at downstream line of stainless tube, which is connected to a Dual Stage Rotary Vane Mechanical Vacuum Pump from Ideal Vacuum (Alcatel 2021 2021SD Pascal SD) with a capability of 10 mTorr ultimate pressure. In order to reduce part of the vacuum pump's exhausted oil fumes and organic chemical and an inlet trap (Foreline Trap for Inlet KF25 Rotary Vane Vacuum Pumps up to 18 CFM), which is for preventing contaminants from inlet of pump and protecting the system from pump fluid or particulate migration, Oil Mist Eliminator (Pfeiffer ONF 10-12, ONF 25 S for Duo 10M, DN/ISO/KF 25 Outlet Flange) is located alongside the rotary pump. The working pressure for synthesis of graphene in the CVD system is 500 mTorr. The temperature of

the furnace was controlled by Temperature Control System for Controlling MTI Furnaces with Computer (EQ-MTS02). The furnace in the CVD system is able to operate at 1200 ^{o}C for prolonged hours, and reach that temperature in 48 min with 25 ^{o}C/min rate.

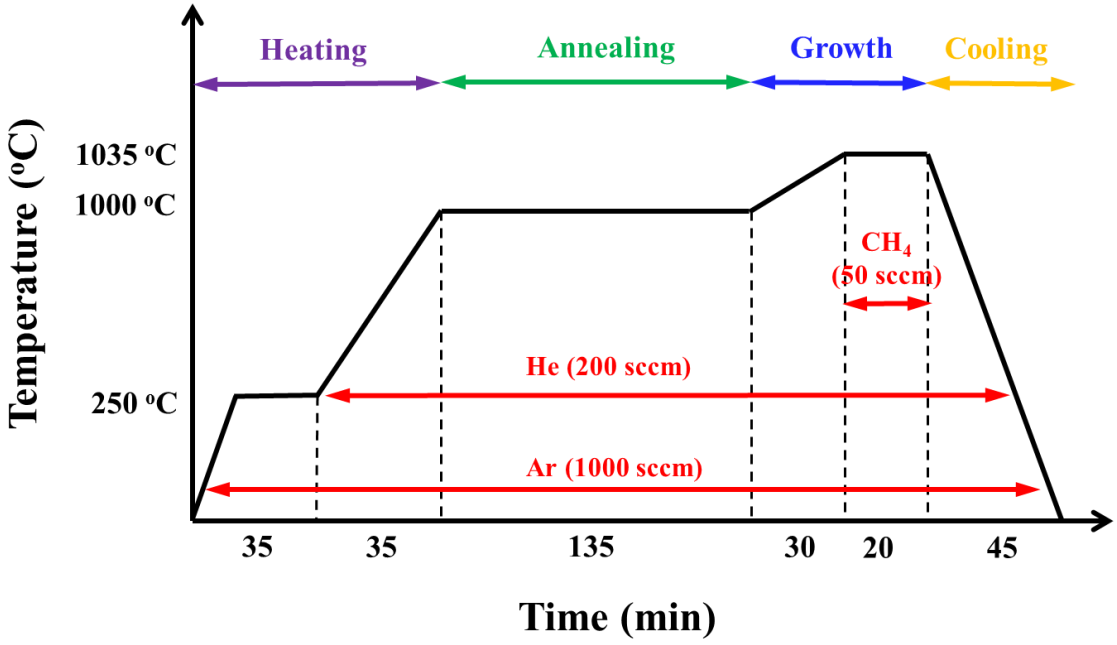

Figure 2.6 The optimized process parameters and sequence of steps for CVD growth graphene.

To use synthesized graphene on Cu foil by CVD technique, the graphene must be transferred on different target substrates to investigate its characterization and fabricate devices. The first step for transferring graphene is removing back side of synthesized graphene on Cu foil using Reactive ion Etching (RIE) chamber (with O_2 plasma) to oxidize and remove graphene layer because graphene is normally deposited on both sides of Cu foil, and the quality for bottom side of graphene on Cu foil is not good. After that, polymethyl methacrylate (PMMA) is spin-coated at 2000 rpm for 30 s twice, and directly

moves to hot plate to bake at 150 ^{o}C for 1 min. The PMMA coated Cu foil with graphene is then kept in 0.5 M of Cu etchant (ammonium persulfate) over 12 h. Once the Cu foil etched, the solution of etchant becomes bluish because of Cu (II) ions, and the PMMA coated graphene is floating on the solution. Deionized (DI) water is used several times to deionize the solution, and the solution is taken away and IPA is poured by pipette. Then, the target substrate is slid under the floating PMMA coated graphene to transfer, and move to hot place to dry the sample at 40 ^{o}C for 30 min. Finally, the coated PMMA is removed from top of transferred graphene by few droplets of 1,2-dichloroethane (99%, Alfa Aesar). All the process of transferring graphene is shown in Fig. 2.7.

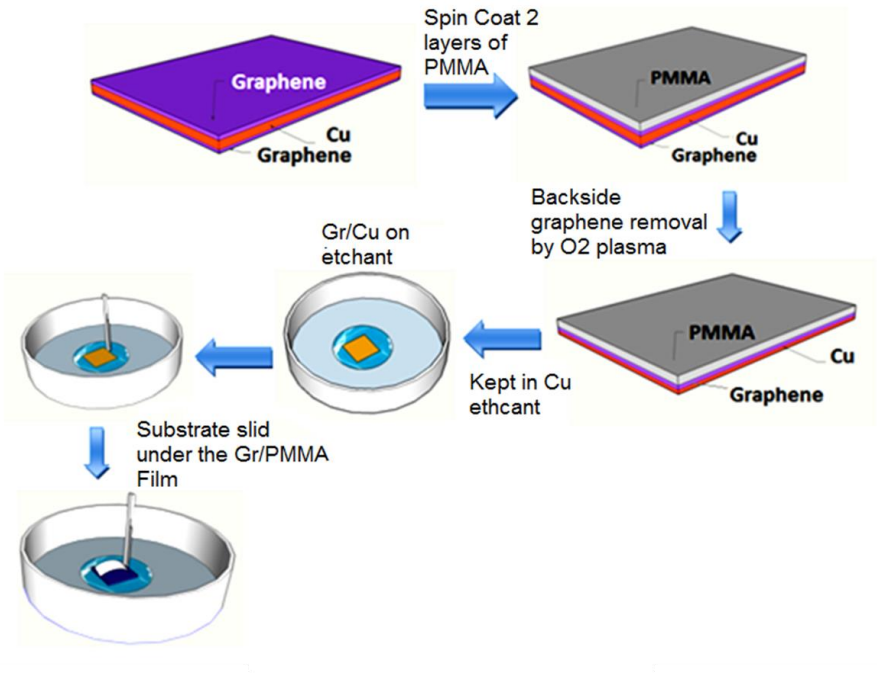

Figure 2.7 The process of transferring graphene on target substrate [78].

2.1.4 Raman spectroscopy

To investigate the quality of graphene, Raman spectroscopy is the one of options and it gives quick and immediate feedback on graphene without any sample preparation. Raman spectroscopy is based on vibrational spectrum of a material system, and it is important to detect in-/organic species and crystallinity of the material. Stress of materials in very small area is also able to be detected because Raman spectroscopy can focus in very small area using laser beam.

Figure 2.8 shows the Raman spectrum of graphene transferred on SiO_2/Si. The interested Raman peaks of graphene lies in the range of 1200 to 3000 cm^{-1}, and the important peaks of graphene in the Raman spectra are G and 2D bands corresponding at ~1580 cm^{-1} and ~2700 cm^{-1}, respectively. The G band corresponds doubly degenerate in-plane transverse optic (iTO) and longitudinal optic (LO) phonon mode, which corresponds to E_{2g} symmetry at the Brillouin zone [79], and it confirms the presence of carbonaceous material with sp^2 bonding. Additionally, the intensity of G band is proportional to the thickness of the material. The origin of 2D is a second order scattering process which involves double resonance and two iTO phonons near K point. There are two more peaks related with defects in graphene such as D and D'. The peak of D corresponds to the double resonance radial breathing modes of sp^2 bonded atoms, while the peak of D' corresponds to sp^3 hybridization. Therefore, the ratio of I_D/I_G (in Fig. 2.8) is 0.13 which means the graphene possess low defect density, while the ratio of I_{2D}/I_G (in Fig. 2.8) is 2.1 with 2D FWHM of 26.4 cm^{-1}, which indicate the presence of monolayer graphene.

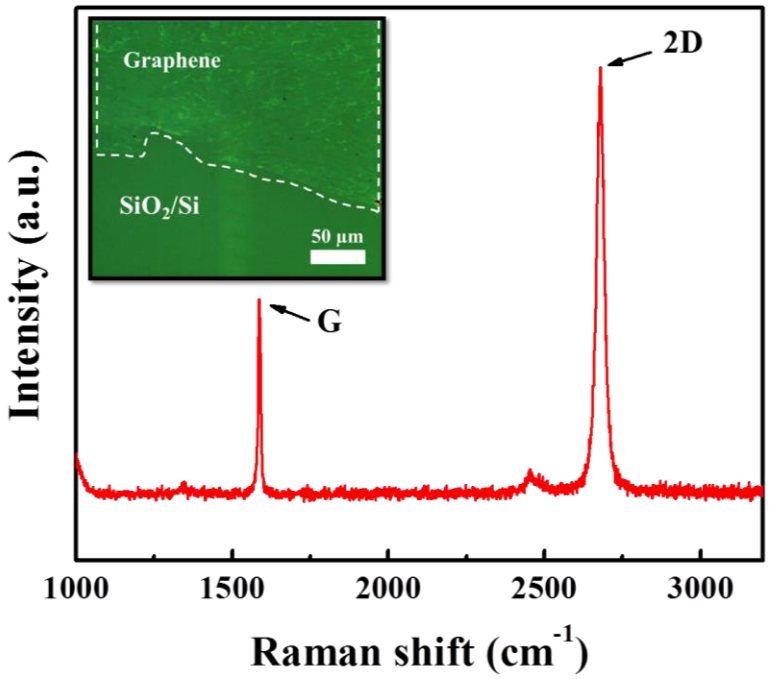

Figure 2.8 Raman spectrum of graphene after transferred on SiO2/Si substrate. The inset shows the optical image of the graphene.

2.1.5 Hall-effect measurement

Hall-effect measurement is a technique for investigating transport properties of a material such as resistivity (ρ), carrier density (N_b), sheet resistance (R_S), hall coefficient (R_H), and mobility (μ) when magnetic field is applied perpendicular to the material which carries a current across it.

Table 2.2 shows the results of Hall-effect measurement of graphene transferred on SiO_2/Si. The bulk carrier density (cm^{-3}), mobility (cm^2/Vs), resistivity (Ωcm), sheet Hall coefficient (m^2/C), sheet carrier density (cm^{-2}), and sheet resistance (Ω/sq) are

investigated by Hall-effect measurement (HMS-3000) as shown in Fig. 2.9, which indicate the measured graphene has high quality and low defect density.

Figure 2.9 A photo image of Hall-effect measurement (Model No.: Ecopia HMS3000)

Table 2.2 Various characteristics of monolayer graphene by Hall-effect measurement.

Bulk carrier density (cm^{-3})	Mobility (cm^2/Vs)	Resistivity (Ωcm)	Sheet Hall coefficient (m^2/C)	Sheet carrier density (cm^{-2})	Sheet resistance (Ω/sq)
1.80×10^{16}	3125	1.2×10^{-1}	3.40×10^{2}	9.1×10^{11}	2.35×10^{3}

2.2 Synthesis of P(VDF-TrFE) film

To prepare P(VDF-TrFE) thin films, most popular technique is spin-coating because it is easy to control its thickness and deposit large area of film with low cost on

many different substrate. For spin-coating, a solution of P(VDF-TrFE) should be synthesized, and there are lots of solvents such as tetrahydrojuran (THF), methylethyl ketone (MEK), dimethylformamide (DMF), and dimethylsulfoxide (DMSO) to dissolve powder of P(VDF-TrFE) [80]. Among them, DMF and DMSO are good solvent to produce high performance of P(VDF-TrFE) when it is spin-coated. Here, in this dissertation, the solution was prepared by dissolving powder of P(VDF-TrFE) (50/50, Piezotech) in N,N-dimethylformamide (DMF) solvent and stirring for 12 h at 40 ℃ to synthesize 13 wt % of P(VDF-TrFE) solution. To obtain a target thickness, the prepared solution of P(VDF-TrFE) was spin-coated at a certain rpm for 60 s as shown in Fig. 2.10. The specific thickness was measured by profilometer. After spin-coating, the film was dried at 60 ^{o}C for 10 min to remove the DMF solvent, and then the P(VDF-TrFE) film

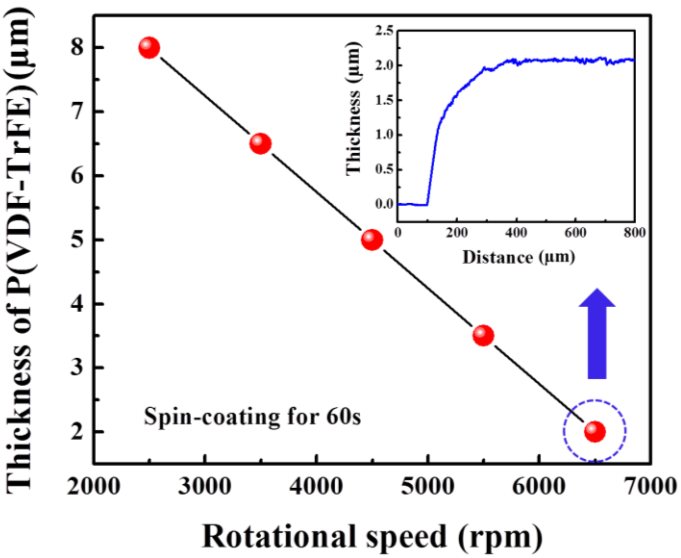

Figure 2.10 Various thickness of spin-coated P(VDF-TrFE) for 60s with different rotational speed. The inset shows the 2 μm thick of P(VDF-TrFE) measured by profilometer.

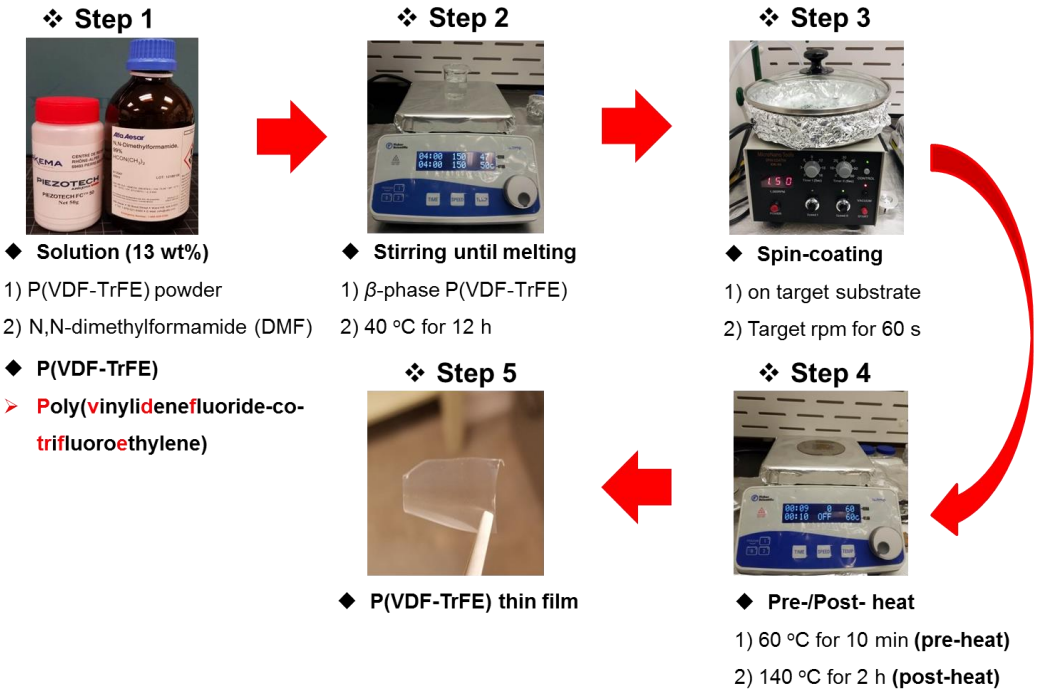

Figure 2.11 The process for synthesis of P(VDF-TrFE) thin film.

was subsequently heated in air at 140 ^{o}C for 2 h to develop the β-phase of P(VDF-TrFE), followed by natural cooling to room temperature. Figure 2.11 shows the process of P(VDF-TrFE) thin film.

2.2.1 Fourier-transform infrared spectroscopy (FTIR)

Fourier-transform infrared spectroscopy (FTIR) as shown in Fig. 2.12 is good method to investigate organic, polymeric, and in some cases, inorganic materials. Infrared radiation (10,000 to 100 cm^{-1}) is used to scan test samples when the materials absorb/pass through some radiation, and observe chemical properties in FTIR analysis.

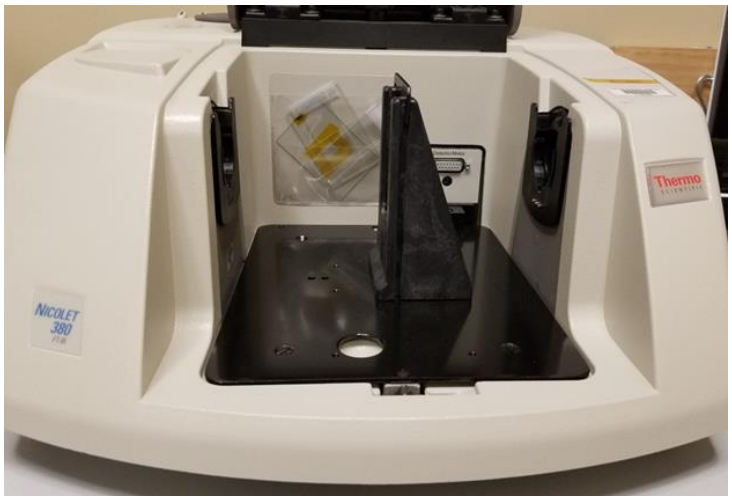

Figure 2.12 A photo image of Fourier-transform infrared spectroscopy (Model No.: Thermo Scientific Nicolet380)

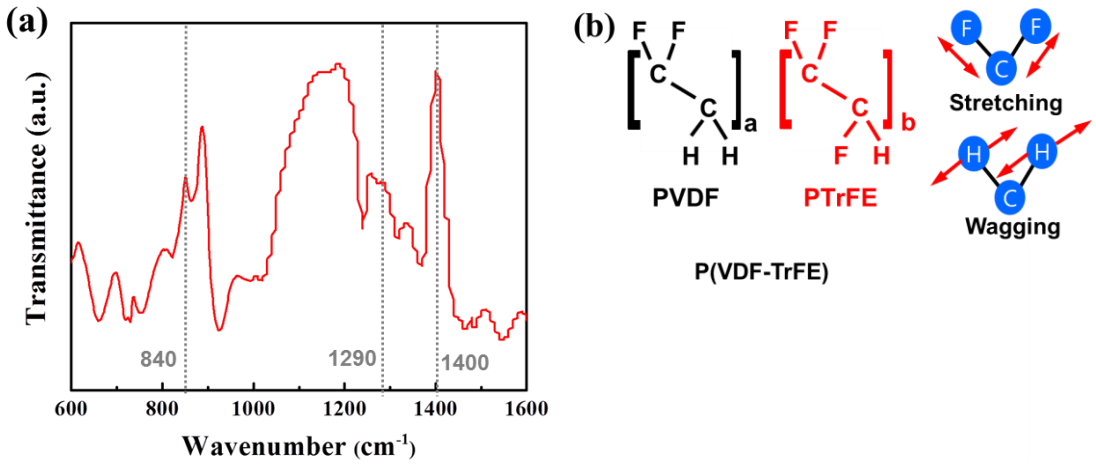

Figure 2.13 (a) FTIR spectrum and (b) the characteristic of P(VDF-TrFE) film.

The absorbed radiation is converted into rotational or vibrational energy by the materials molecules, presenting as a spectrum (4000 to 400 cm^{-1}) from the resulting signal at the detector. The molecule or chemical structure will produce unique spectral

fingerprints, resulting in strong technique for chemical identification. Figure 2.13(a) shows FTIR result of β-phase of P(VDF-TrFE) film. There are three major peaks at 840, 1290, and 1400 cm^{-1}. The peak of 840 and 1290 cm^{-1} is characteristic of CF_2 symmetric stretching in β-phase of P(VDF-TrFE), while the peak of 1400 cm^{-1} is that of CH_2 wagging in β-phase of P(VDF-TrFE) [33] as shown in Fig. 2.13(b).

2.2.2 X-ray diffraction (XRD)

X-ray diffraction (XRD) as shown in Fig. 2.14 is a powerful method in determination of crystalline materials and fingerprint of different polymorphic forms, and also distinguishing between amorphous and crystalline material. XRD technique is based on constructive interference of monochromatic X-rays and a crystalline material. The constructive interference is produced by the interaction of the incident rays when Bragg's Law ($n\lambda=2d\sin\theta$) is satisfy with the condition. The strongest advantage of XRD is that there is fingerprint of the crystals present in the material for the generated spectra of XRD pattern, which allows identification of the crystalline form.

Figure 2.15 shows the XRD results of P(VDF-TrFE) film. The orientation planes (110) and (200) shown in the XRD spectra are related to the polar β-phase, since the diffraction peak position is shown at a 2θ value of 19.7 [81].

Figure 2.14 A photo image of X-ray diffraction (Model No.: Rigaku ULTIMA IV, Department of Chemistry in Clemson University)

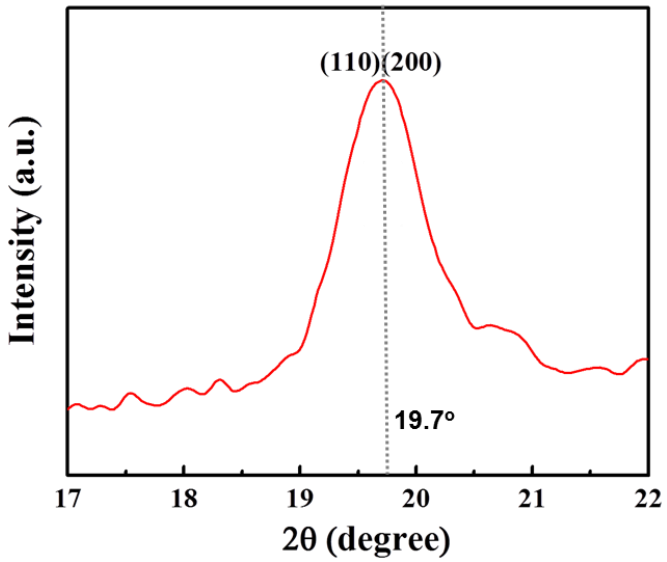

Figure 2.15 XRD spectrum of P(VDF-TrFE) film

2.2.3 Polling of P(VDF-TrFE) film

A polling process of P(VDF-TrFE) film is needed to use its properties such as piezoelectric and pyroelectric for several applications. In this dissertation, an extra electric field of 100 MV/m was applied to the P(VDF-TrFE) film for 1h using DC power supply as shown in Fig. 2.16. The process time of polling was found to be optimal as 1 h because further increase in time up to 2 h only resulted in less than 5% increase in the voltage generated across the film when similarly strained as shown in Fig. 2.17. Additionally, it should be noted that the degree of alignment of the dipoles decreases with time after the poling. In Fig. 2.18, we show the V_{gen} (under similar strain) vs. T_E (the time elapsed after poling), which indicates that the degree of poling reduces with time, but at a decreasing rate, and becomes steady after a few days at a value of ~55% of the maximum value achieved immediately after poling. This observation of decrease in the degree of poling and percentage of steady state value is consistent with earlier reports [82-84].

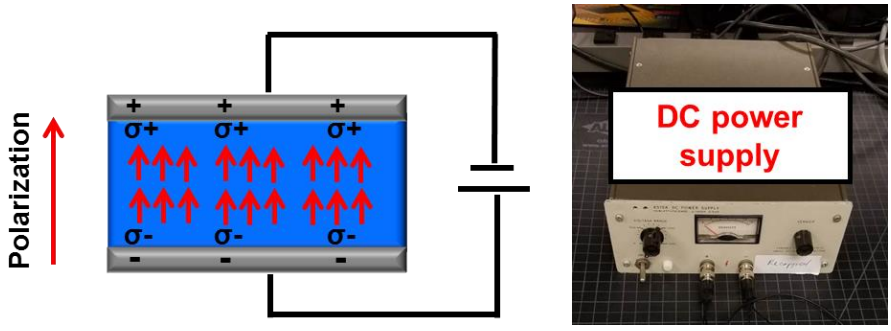

Figure 2.16 A polling process of P(VDF-TrFE) film with DC power supply.

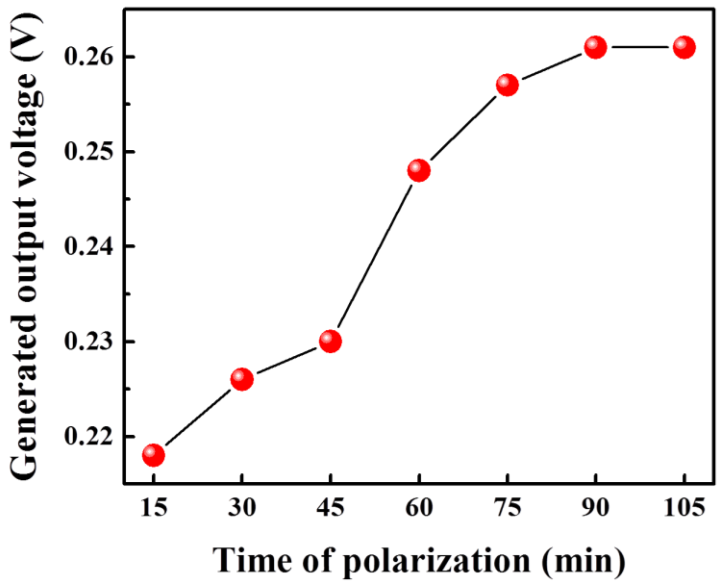

Figure 2.17 Generated output voltage (%) vs the process time of polling.

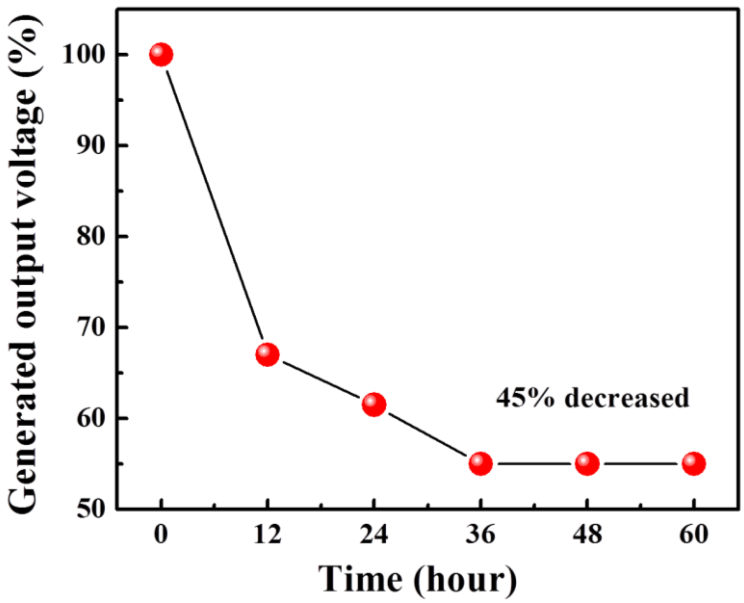

Figure 2.18 Generated output voltage (%) vs the time elapsed after polling.

CHAPTER THREE

ENERGY HARVESTING APPLICATIONS OF P(VDF-TRFE) ON FLEXIBLE SUBSTRATES

3.1 PDMS substrate based energy harvester

We have developed and demonstrated a highly flexible P(VDF-TrFE) film-based energy harvesting device on a PDMS substrate, avoiding any complex composites and patterned structures. The structural and electrical properties of the P(VDF-TrFE) film was investigated using multiple characterization techniques and an optimized film of 7 μm thickness was used for the energy harvesting application. The device, with Ti/Ni metal contacts, was driven by a shaker providing an acceleration of 1.75 g, and frequencies varying from 5 to 30 Hz. The energy harvesting performance of the final fabricated device was tested using the shaker, and resulted in a maximum output capacitor voltage of 4.4 V, which successfully powered a set of 27 LEDs after several minutes of charging.

3.1.1 Introduction

Energy harvesting devices have attracted immense research interest over the years due to the need for powering remote and unattended sensors, as well as low-power electronics [63,85,86]. Several different types of energy harvesting devices have been investigated over the past decade, of which electromagnetic, electrostatic, and piezoelectric ones have received the most attention [87-89]. Piezoelectric energy harvesting devices are especially attractive due to their compact size and easy scalability

and manufacturability. Among them, flexible piezoelectric material-based energy harvesters offer the advantage of being used in implantable or wearable bio-electronic devices and sensors, combined with the other advantages of piezoelectric generators, including high energy density, low mechanical damping, and easy voltage rectification [90]. Thus, they find usage in many applications including biometrics, strain monitoring, and mobile devices. While inorganic piezoelectric materials such as ZnO [91,92], $ZnSnO_3$ [93,94], and PZT [95,96] have been used extensively for harvesting energy, flexible piezoelectric materials such as poly(vinylidenefluoride-co-trifluoroethylene) P(VDF-TrFE) [34,35] have been investigated recently due to their high piezoelectric coefficient, flexibility, sensitivity, and mechanical durability. In addition, P(VDF-TrFE) is fully bio-compatible, making it suitable for energy harvesting applications when implanted. P(VDF-TrFE), which can be simply obtained by varying the molar ratio of TrFE in proportion to PVDF, offers several advantages compared to PVDF, including higher piezoelectric coefficient [31], better crystallinity, higher remnant polarization, and higher temperature stability [32,33].

Since P(VDF-TrFE) is a film with a thickness of several microns, typically a substrate is utilized as mechanical support. Among the substrates used, polydimethylsiloxane (PDMS) substrate has proven to be particularly useful because of advantages such as high elasticity, easy molding capability, and biocompatibility. The flexibility and bio-compatibility of the PDMS substrate make the energy harvester attractive for usage in implantable or wearable devices, i.e., monitoring and tracking intrinsic (such as muscle fatigue) and extrinsic (such as twisting and bending of limbs)

human parameters as part of biomedical applications, and smart monitoring systems including temperature sensors or low power microprocessors. Lee et al. [65] fabricated a nanogenerator (NG) using P(VDF-TrFE) film (active material, 7 μm) and a patterned PDMS-CNT composite as the bottom electrode, demonstrating maximum output voltage and current of 1.4 V and 150 nA, respectively. Wang et al. [97] developed patterned PDMS-MWCNT composite-based P(VDF-TrFE) (active material, 85 μm) hybrid energy harvester, and demonstrated piezoelectric output voltage and current of 2.5 V and 2.5 A, respectively. Han et al. [98] reported that patterned PDMS used as micro/nano dual scale can increase the surface roughness and provide more strain to the PVDF film (active material, 100 m) enhancing its power generation capacity. The resulting output voltage and current density reported from their devices were 52.8 V and 20.75 $\mu A/cm^2$, respectively. Ding et al. [99] developed PDMS/polyethylene terephthalate (PET)-based PVDF (active material, 5 μm) energy harvester, and the demonstrated output voltage and current were 150 mV and 4 nA, respectively. The output performance PVDF and P(VDF-TrFE) energy harvesters are shown in Table 3.1 [35,65,97-101].

In spite of their promise, PDMS-based composites (with other materials, such as CNT) or patterned structures, as reported earlier, pose several challenges, including complicated fabrication processes, low reproducibility, non-uniform output, difficulty in interfacing with active layers like the P(VDF-TrFE) matrix, and degradation of structures over long-term usage in strong vibrational environments. An additional issue with the structure of PDMS-based composites (i.e., PDMS/CNT) is that, due to their higher

Table 3.1 Comparison of the output performance of piezoelectric energy harvesters in recent years. The current work is shown in bold.

Substrate	Piezoelectric material (μm)	Size (cm^2)	Output performance			Input Frequency (Hz)	Ref
			Voltage (V)	Current (μA)/ Current density ($\mu A/cm^2$)	Power density (mW/cm^3)		
PDMS	**P(VDF-TrFE) (7 μm)**	**2 × 2**	**5.8 V**	**3.2 μA/ 0.8 $\mu A/cm^2$**	**6.62 mW/cm^3**	**5 ~ 30 Hz**	**This work**
CNT/PDMS	P(VDF-TrFE) (7 μm)	4 × 4	1.4 V	~150 nA	0.018 mW/cm^3	N/A	65
MWCNT/PDMS	P(VDF-TrFE) (85 μm)	0.8 × 0.8	2.5 V	~2.5 μA	0.689 mW/cm^3	1 ~ 4 Hz	97
PDMS	PVDF (100 μm)	4 × 2	52.8 V	20.75 $\mu A/cm^2$	10.95 mW/cm^3	5 ~ 10 Hz	98
PDMS	PVDF (5 μm)	3 × 3	150 mV	4 nA	1.33×10^{-4} mW/cm^3	1 ~ 2.3 Hz	99
ITO	P(VDF-TrFE) (50 μm)	1 × 1	4.0 V	2.6 μA	2.08 mW/cm^3	1 ~ 100 Hz	35
Silicone	PVDF (200 μm)	4.2 × 2	1.5 V	400 nA	3.57×10^{-3} mW/cm^3	~ 1.4 Hz	100
N/A (ITO & Gold electrodes)	P(VDF-TrFE) (30 μm)	1 × 1	4 V	1.88 μA	2.5 mW/cm^3	1 Hz	101

resistance, the output current and voltage are usually much lower, strongly degrading energy harvesting performance. In this study, we have developed a flexible P(VDF-TrFE) film-based energy harvesting device on a simple PDMS substrate, avoiding any complex

composites and patterned structures, while demonstrating performance comparable to or higher than the other devices reported on PDMS substrate. We have utilized profilometer, optical microscope, Fourier transform infrared (FTIR) spectroscopy and X-ray diffraction (XRD) to investigate the thickness, surface and structural properties of the P(VDF-TrFE) film. A COMSOL simulation was also performed to determine the strain and estimate the device performance. A shaker was used to measure the performance of the device at various frequencies, and power a set of LEDs as a simple application.

3.1.2 Experimental Details

Fabrication of the Flexible Piezoelectric Energy Harvester

To fabricate the P(VDF-TrFE) films, first the co-polymer powder of P(VDF-TrFE) (50/50, Piezotech) was dissolved in N,N-dimethylformamide (DMF) solvent. The solution was then stirred for 12 h at 40 ℃ to synthesize 13 wt. % of P(VDF-TrFE) solution. To make polydimethylsiloxane (PDMS) substrate (3.5 cm (W) × 3.5 cm (L) × 0.15 cm (H)), the liquid PDMS (weight ratio of elastomer to cross linker used was 10:1) was poured into square mold and then directly degassed to remove bubbles in a vacuum desiccator for 1 h. After that, it was heated in air at 100 ℃ for 30 min. Ti/Ni (30 nm/150 nm) metal stack (2 cm × 2 cm) was deposited at 100 ℃ by electron beam evaporation on the PDMS substrate to form the bottom electrode. Heat plays an important role in this fabrication process, as it improves the conductivity (by lowering resistance) when the Ti/Ni metal stack (2 cm × 2 cm) is deposited on the PDMS substrate directly. The PDMS substrate, owing to its tensile strength, was stretched while it was exposed to heat

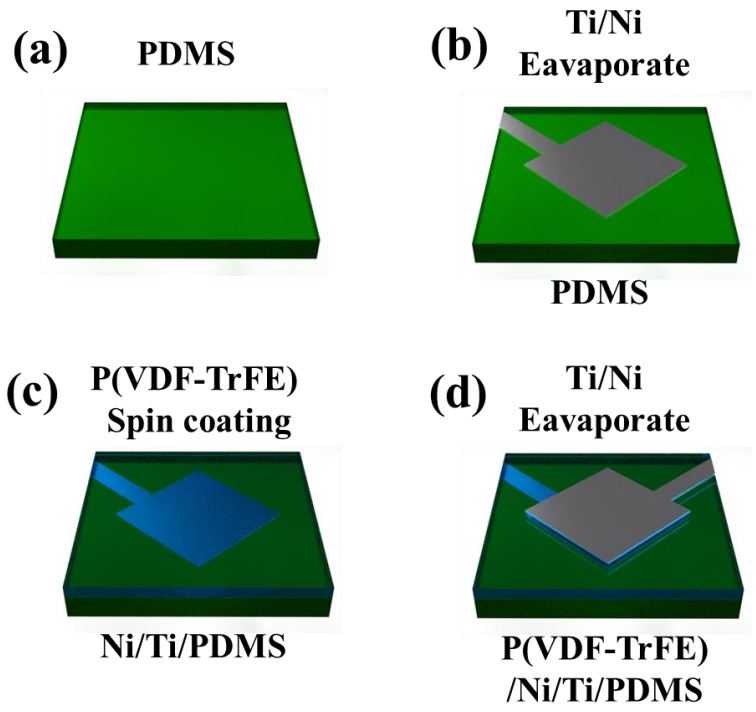

Figure 3.1 (a) PDMS substrate (3.5 cm (W) × 3.5 cm (L) × 0.15 cm (H)) was made by elastomer and cross linker (weight ratio 10:1); (b) Ti/Ni (30 nm/150 nm) was deposited on the PDMS substrate by electron beam evaporator; (c) P(VDF-TrFE) was spin-coated on Ni/Ti/PDMS at 3500 rpm for 60 s; (d) Ti/Ni (30 nm/150 nm) was deposited on the P(VDF-TrFE)/Ni/Ti/PDMS by electron beam evaporator. After that an electric field of 100 MV/m was applied for 1 h to align the dipoles in the P(VDF-TrFE) film uniformly.

(100 ℃), and first metal (Ti, 30 nm) was permeated into the surface of PDMS substrate, and then second metal (Ni, 150 nm) was finally deposited on the Ni/PDMS. Since cooling produces metal layer overlap, it makes the metal stack more stable under bending and vibration conditions from external force.

Next, a solution of the P(VDF-TrFE) was spin-coated on the PDMS substrate.

A thickness of 7 μm was obtained by rotating the spin coater at 3500 rpm for 60 s. The DMF solvent was evaporated by pre-heating the device at 60 ℃ for 10 min. The film was subsequently heated in air at 140 ℃ for 2 h. A second layer of Ti/Ni (30 nm/150 nm) was deposited at 100 ℃ by electron beam evaporation to form the top electrode. To perform "poling" of the P(VDF-TrFE) film, an electric field of 100 MV/m was applied for 1 h to align the dipoles in the film [102]. The electric field of 100 MV/m was reached gradually by increasing the field by 10 MV/m in every 5 min to avoid breakdown due to sudden application of voltage. All the fabrication steps are shown in Figure 3.1.

Measurement and Characterization

The thickness, surface, and structural properties of the sample were investigated using profilometer (Tencor AS-200), optical microscopy (Micromanipulator Corp. MODEL No. 6000), Fourier transform infrared (FTIR) spectroscopy and X-ray diffraction (XRD). A shaker (LDS V203) was used to strain the P(VDF-TrFE) layer and a digital force gauge (Shimpo FG-3000) was used to measure the force from the shaker, which was converted to acceleration based on the mass moved. A digital phosphor oscilloscope (Tektronix TDS 5054), data acquisition (Agilent 34970A), and low-noise current preamplifier (Stanford Research Systems Model SR570) were used to measure the electrical signal from the device. In our experiment, the device was clamped to subject it to variable frequency excitation from the shaker attached with an extended arm, to investigate its performance (shown clearly in Figure 3.4(a)).

Simulations: Strain, Stress, and Potential

The strain and stress distribution on the P(VDF-TrFE) film was simulated using the COMSOL finite-element simulation software. A solid mechanics module was used to simulate the stress and deformation of the device. The Young's Modulus used in the simulation was 2.3×10^6 Pa for P(VDF-TrFE) and 2.6×10^6 Pa for PDMS. The simulation used the same dimensions as in the fabricated device (3.5 × 3.5 cm for PDMS, and 2 × 2 cm for P(VDF-TrFE)), as shown in Figure 3.4(b). An acceleration of 1.75 g was applied onto half of the bottom surface of this device. Considering PDMS comprises more than 99.9% of the thickness of the entire structure, the strain distribution is mainly dependent on PDMS layer. Hence the deformation of active material P(VDF-TrFE) can be assumed to be same as the deformation of the upper surface of the PDMS layer where it is attached. Since the edge of the shaker will first hit the center-line of the device, this point will experience the most strain during the process. When the shaker is in contact with the device, the active material experiences a uniform acceleration for a short period of time. Then strain is mainly formed within the stretched (overhanging) half of the device, as shown in Figure 3.4(c). The potential simulation of COMSOL was performed using the information provided by the P(VDF-TrFE) powder manufacturer (Piezotech) with regard to the piezoelectric voltage constants g_{31}, g_{32} and g_{33}, which were 216, 19 and -339×10^{-3} Vm/Nm^2, respectively. These results are shown in Figure 3.4(d). The resonancemodeswere investigated both analytically and through simulations. The fundamental resonant frequency (f_0) of the device was found to be ~10.1 Hz from the equation:

$$f_0 = \frac{1}{2\pi}\sqrt{\frac{E}{\rho}}\frac{t}{wl}, \quad (1)$$

where E is Young's Modulus, r is density, t is thickness, w is width, and l is length. The resonant frequencies were also simulated using COMSOL, and f_0, f_1, and f_2, turned out to be 11.77 Hz, 25.55 Hz, and 68.93 Hz, respectively. We excited the device at frequencies of 5, 10, 20 and 30 Hz, overlapping the range of frequency of fundamental and first order modes.

3.1.3 Results and discussion

The schematic diagram of our flexible piezoelectric energy harvester is shown in Figure 3.2(a). The device comprises four layers with the Ti/Ni as the top and bottom electrodes, the P(VDF-TrFE) piezoelectric film, and the PDMS substrate. Previously, a nanogenerator (NG) fabricated by Lee et al. [65] made use of the patterned PDMS-CNT composite to form the bottom electrode, while patterned PDMS was used as micro/nano dual scale by Han et al. [98] to increase the surface roughness of the NG. Wang et al. [97] also used patterned PDMS-MWCNT composite to obtain increased roughness and lower internal resistance in the device. As mentioned above, these methods included complex fabrication steps, such as chemical etching, photolithography, and plasma treatment, which add more cost and increase the complexity of fabrication. An optical image of our device, which is much simpler in construction, is shown in Figure 3.2(b). All the materials, such as Ti/Ni for electrodes and P(VDF-TrFE) film for active area, were found to adhere well onto the PDMS substrate and withstand repeated cycles of bending and stretching.

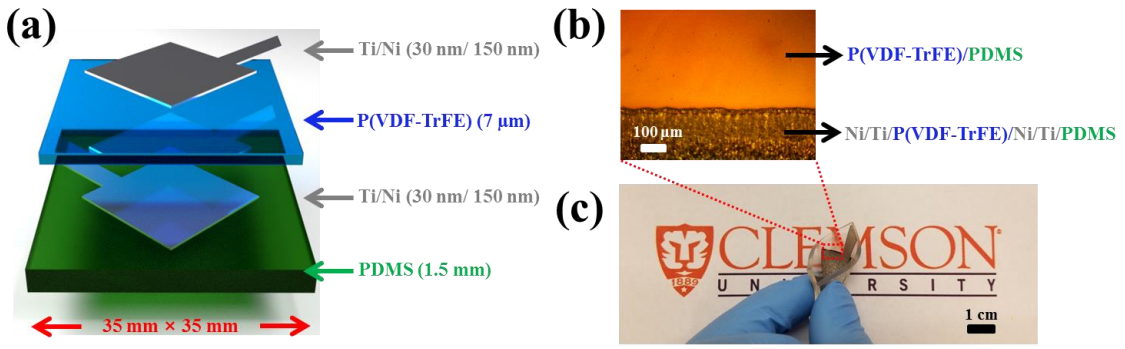

Figure 3.2 (a) Schematic illustration; (b) optical microscopy image; and (c) photographic image of the proposed device.

Once the composition and thickness had been optimized, we performed structural characterization using the XRD technique on the prepared P(VDF-TrFE) film, and the results are shown in Figure 3.3(a). We found that the orientation planes (110) and (200) shown in the XRD spectra are related to the polar *β*-phase, since the diffraction peak position is shown at a 2θ value of 19.7° [81,103]. FTIR measurements were also carried out to further confirm the presence of *β*-phase P(VDF-TrFE). Figure 3.3(b) indicates the signature FTIR spectra of the film, with 3 peaks corresponding to the *β*-phase P(VDF-TrFE): 842 (CH2 rocking), 1286 (trans band) and 1400 (CH2 wagging) cm^{-1} [33,104]. Taken together, these tests clearly indicate that the synthesized film is indeed P(VDF-TrFE).

To determine the efficacy of the layered energy harvesting structure prepared, it was exposed to external strain using a mechanical shaker, and the output voltage and power were recorded. Figure 3.4(a) shows a photographic image of the basic experimental setup for energy harvesting, which consists of an oscilloscope

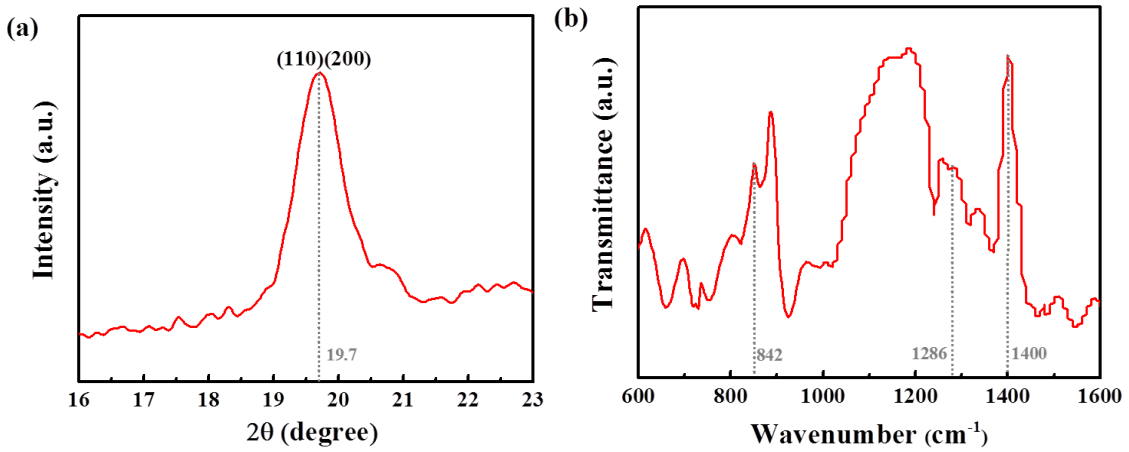

Figure 3.3 (a) XRD and (b) FTIR result of b-phase of P(VDF-TrFE) film. The XRD peak at 19.7 degrees and the transmittance peaks at 842, 1286 and 1400 cm^{-1} confirm the material is *β*-phase P(VDF-TrFE).

(Tektronix TDS 5054), a Shaker (LDS V203), and the device attached to the shaker. The output voltages were obtained from the device under application of an external force at frequencies of 5, 10, 20 and 30 Hz at 1.75 g acceleration. The force was provided by the shaker. An extended metal arm from the shaker was attached to the bottom center of the device to provide the oscillatory force (see Figure 3.4(a)). The active area of the harvesting device is estimated to be ~4 cm^2 (2 × 2 cm).

A COMSOL-based finite element simulation was performed to theoretically estimate the stress, strain, and voltage output from the device. From the simulation results (see Figure 3.4(c)) the peak and average stresses were found to be 8.42×10^6 and 2.45×10^6 N/m^2, respectively, for the P(VDF-TrFE) films over the active area. The output voltage calculated from the relation $V = g_{33} \times \sigma_3 t$ (g_{33}: piezoelectric voltage constant, σ_3:

applied mechanical stress, and t: thickness of film) yields the peak and average voltages of 20 and 5.8 V, respectively. Moreover, the peak and average surface charge densities of ~355 and 105 $\mu C/m^2$ for 20 and 5.8 V, respectively, were obtained using the equation $V = \sigma t/\varepsilon$ (V: voltage, σ: surface charge density, t: thickness, and ε: dielectric constant). The calculated values of the voltages are well matched with the experimental data (see Figure 3.5), as well as simulation data for potential (see Figure 3.4(d)). The simulation figures

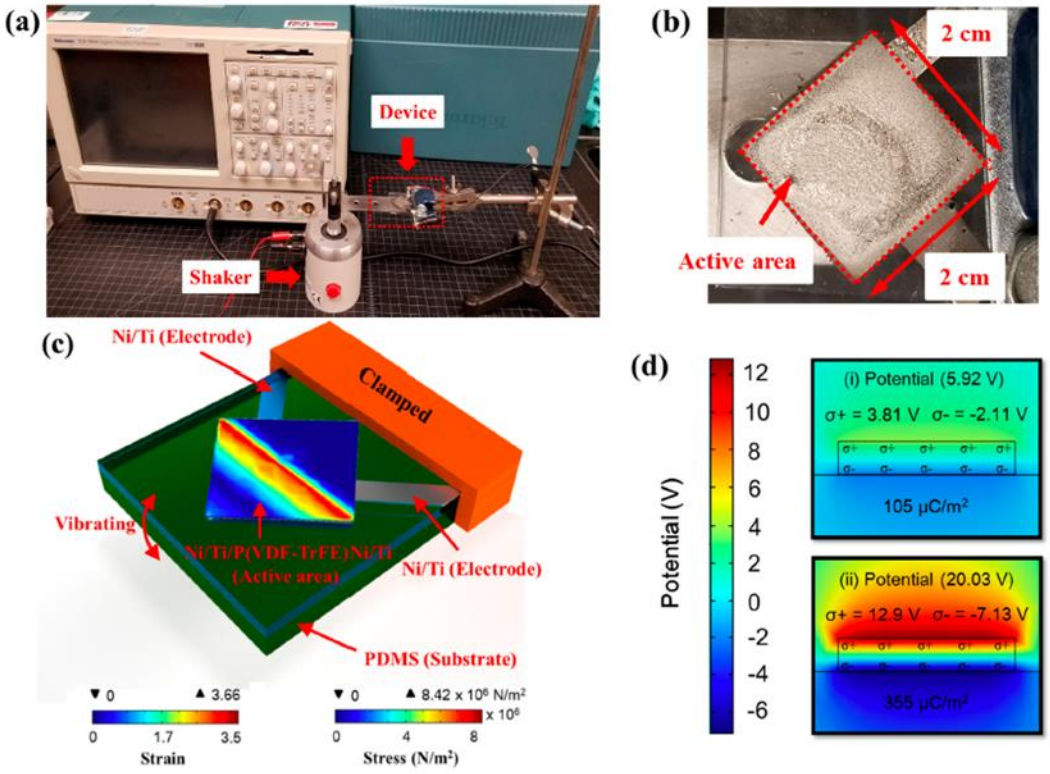

Figure 3.4 (a) Photographic image of the basic experimental setup and (b) image of the device under test; (c) Finite element (COMSOL) simulation of strain and stress distribution and (d) piezoelectric output voltages and surface charge densities over the active area (2×2 cm^2).

show positive charge (and voltage) developing on the P(VDF-TrFE) positioned on top of the PDMS substrate, with negative charge and voltage at the interface of P(VDF-TrFE) and PDMS. The charges on the top surface of the P(VDF-TrFE) meet air, while the bottom surface has PDMS, so although the charge densities are the same, the voltage magnitudes generated are different.

Figure 3.5(a)-(d) shows the frequency-dependent output voltage and current of the device under an external force at the various frequencies. The oscilloscope and low-noise current preamplifier were used to measure the electrical signal from the device. It is evident that the average voltage and current (solid parts of peaks in each figure) gradually increase with the increase of frequency, while the maximum upper peak voltage remains almost same at around 20 V. The increase in average voltage and current is attributed to the increase in the average surface charge as the bending frequency is increased. This occurs due to the slower discharge rate of the device as compared to the input pulse rate, resulting in a continuous rise in the output voltage and current as frequency is increased [105,106]. At 30 Hz, the peak value of average voltage and current is 5.8 V and 3.2 μA (see Table 3.2), while the maximum upper peak value of voltage and current is 20 V and 6.5 μA. These voltages are well matched with the calculated output potential, as mentioned above. Additionally, the value of average voltage of 5.8 V matches the final output voltage available across the full wave bridge rectifier circuit of 4.4 V (steady-state voltage value on the capacitor), considering a total drop across two diodes of ~1.4 V. This result is further discussed below.

The aforementioned energy harvesting performance is quite impressive,

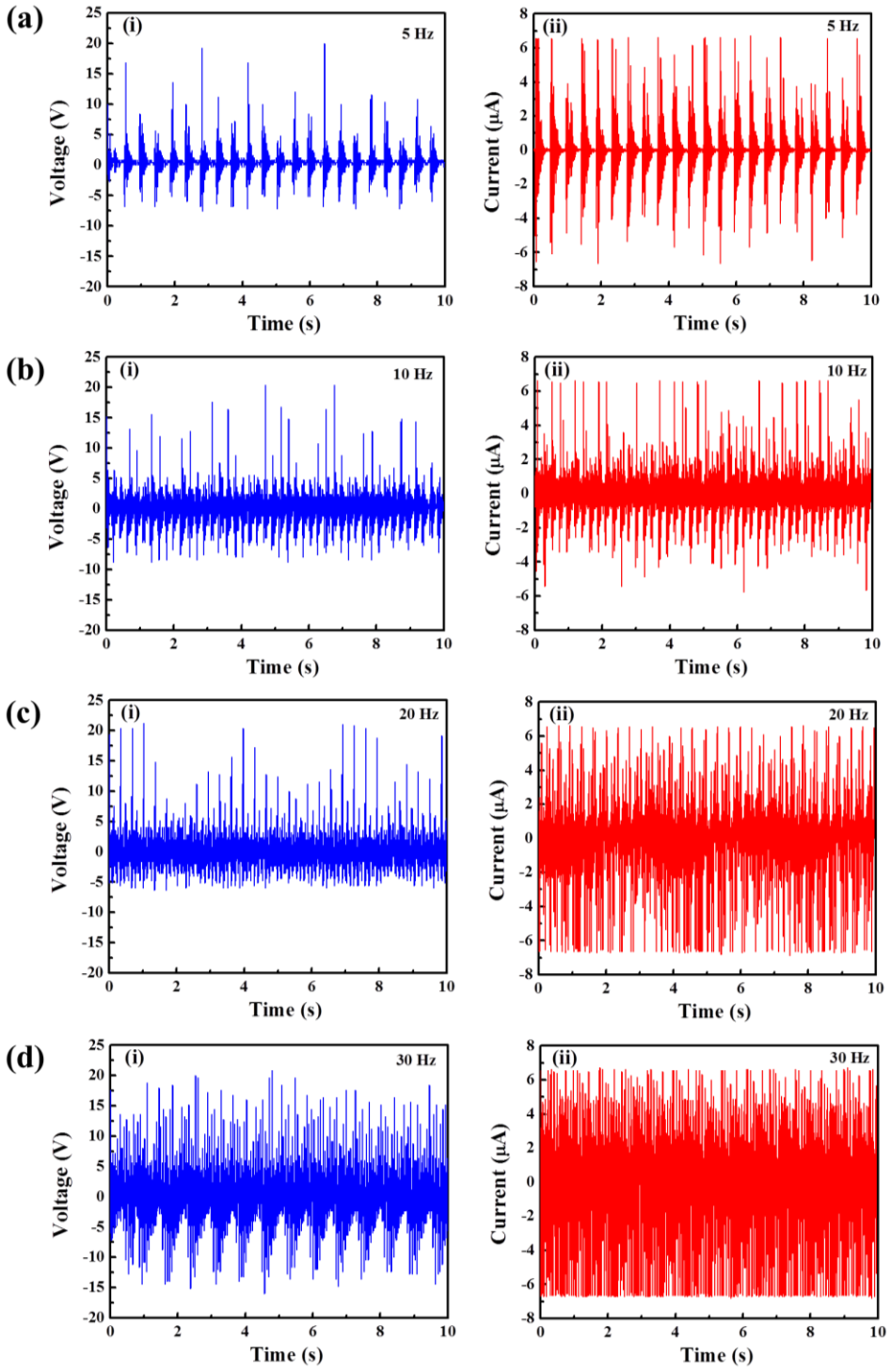

Figure 3.5 (a–d) the frequency-dependent (5, 10, 20 and 30 Hz, respectively) output (i) voltage and (ii) current of the device under application of an external force.

Table 3.2 Average output voltage, current, and power of the device for various excitation frequencies.

Frequency (Hz)	Average voltage (V)	Average current (μA)	Average power (μW)
5	2.8	1.2	3.36
10	3.3	1.5	4.95
20	3.8	2.1	7.98
30	5.8	3.2	18.56

compared to the previously reported performance of flexible energy harvesters on PDMS substrate. Ding et al. [99] developed PDMS/PET-based PVDF (5 μm thick) piezoelectric NG with an output voltage of 150 mV. Wang et al. [97] fabricated patterned PDMS-MWCNT composite-based P(VDF-TrFE) (85 μm thick) hybrid NG, and piezoelectric output voltage was 2.5 V. Micropatterned (pyramid-shaped) P(VDF-TrFE) piezoelectric-pyroelectric NG (7 μm thick) on the CNT/PDMS composite substrate demonstrated by Lee et al. [65] led to an output voltage of only 1.4 V. By comparison, our device provides a significantly better performance, while requiring a much simpler fabrication process. Table 3.1 compares the output performance of the current device with various PVDF and P(VDF-TrFE) based NG reported earlier.

The output voltage transient across the output capacitors with different capacitance values of 4.7 μF, 10 μF, and 47 μF, under an external force with 30 Hz

frequency, is shown in Figure 3.6(a). The inset shows a magnified plot of charging transients up to 100 s. We found that the output voltage on the 4.7 µF capacitor terminals reached 4.4 V in ~60 s, while it took ~145 s and ~1085 s, respectively, to charge the 10 µF and 47 µF capacitors to the same voltage (4.4 V). The maximum stored energy and average power values were determined to be 113.74 µJ and 370 nW, respectively. Based on the active area and thickness of the sample (4 cm^2 and 7×10^4 cm), the maximum output power density can be calculated as 6.62 mW/cm^3, which is comparable to the state-of-the-art performance across all energy harvesting device technologies [35,65,88,97-101,107-114]. Although the power from the device is in the sub µW range, just a single device can still provide sufficient power to operate structural health monitoring devices, such as a 100 nW temperature sensor, or a low-power 4 kB 80 nW microprocessor [115-117].

To demonstrate a simple practical application of the energy harvester, we used it to light a set of 27 commercial LEDs connected in parallel. The overall circuit schematic, including 4 diodes, a switch, a capacitor, and 27 LEDs is shown in Figure 3.6(b). As the capacitor reaches the threshold voltage (2.2 V), it turns on the LEDs, which then begin to glow. A picture of the lighted LEDs after the threshold voltage from the output capacitor was reached is shown in Figure 3.6(b). This device can be used to charge many capacitors sequentially over a longer period to obtain a much higher stored energy that can be used for various applications, such as powering wireless sensors, wearable/implantable bio-electronic devices, or smart monitoring devices [118-120].

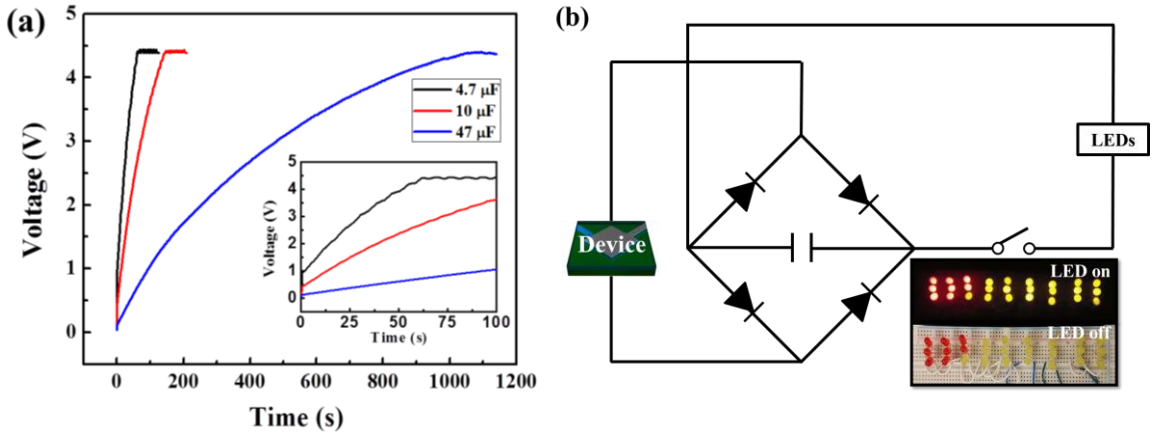

Figure 3.6 (a)Voltage-time charging curve of storage capacitors with different capacitances (4.7 μF, 10 μF, and 47 μF) under application of an external force with 30 Hz frequency. The inset shows an enlarged plot of voltage-time charging curves; (b) Electric charging circuit for the storage capacitor, and a picture of an LED assembly that glows by drawing power from the storage capacitor after energy harvesting is done.

3.1.4 PET substrate based energy harvester

In spite of the simple design of PDMS based energy harvester, the performance of the device was found to be superior compared to other flexible energy harvesters on PDMS substrate. However, there was a challenge (i.e., metal contact issue for long term usage) on the PDMS based energy harvester due to the cleaved surface of PDMS substrate under the strain or pressure, which made cracks on bottom electrode. This crack results in reducing the performance of energy harvester seriously and limiting it for only less strain or pressure condition. To solve this issue, polyethylene terephthalate (PET) is a good candidate for the next version of P(VDF-TrFE) energy harvester due to the high mechanical durability under the bending and vibration conditions. In addition, PET based

energy harvester can be used for triboelectric energy harvester using back side of the device because P(VDF-TrFE) piezoelectric energy harvester has friction inevitably when the active layer is bent and recovered to generate power. Thus, we have developed a device with P(VDF-TrFE) film for multiple energy harvesting applications based on piezoelectric and hybrid (tribo-/piezo- electric) structures.

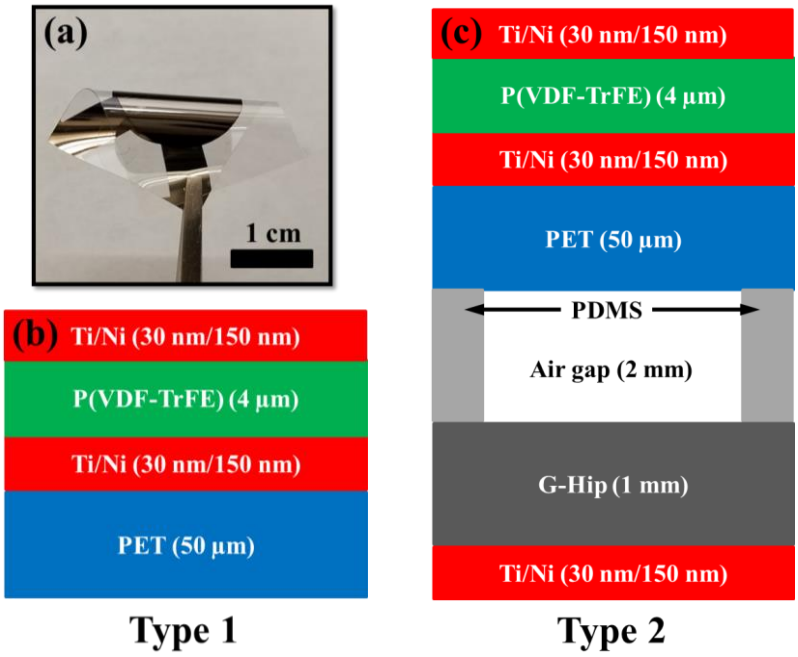

Figure 3.7 (a) Optical image of type 1, (b) Schematic illustration of the design (type 1), and (c) schematic illustration of the design (type 2).

Figure 3.7 shows schematic illustrations of the device. The device (Type 1), with PET (50 µm), two layers of Ti/Ni (30 nm/150 nm), and P(VDF-TrFE) (4 µm), was simply fabricated and also highly flexible as shown in Fig. 3.7(a). Bottom and top electrodes (Ti/Ni) was deposited by electron beam evaporation. A layer of P(VDF-TrFE) was spin-coated with 13 wt% of its solution at 1500 rpm for 60 s. The coated film were

pre-heated at 60 ℃ for 10 min, and then subsequently post-heated in air at 140 ℃ for 2 h. After that, an electric field of 100 MV/m was applied for 1 h to align the dipoles in the P(VDF-TrFE) film uniformly. To fabricate another device (type 2), we printed graphene high impact polystyrene (G-HIP) (3 cm × 2 cm × 1 mm) by 3D printer, and Ti/Ni electrode was deposited on G-HIP by electron beam evaporation. Finally, two PDMS spacers were placed between type 1 and G-HIP with metal electrode to support mechanical force from air gap for triboelectricity.

We demonstrated the devices in multiple energy harvesting applications to generate voltage using wind power (type 1) and mechanical force (type 2). Figure 3.8(a) shows voltage performance of the type 1 under wind power, and inset shows a photo image of the device as flag application. The device was fluttered and generated the peak to peak voltage of 2 V when subjected to air flow. This device can be placed on windmill, roof, or running car to generate a certain power ranges (μW ~ mW) to support electric loads such as low power temperature sensor or microprocessor [115-117] after adding multiple devices on flagpole. Another device (type 2) generated two different types of voltage from hybrid structures such as piezoelectricity and triboelectricity under the mechanical force as shown in Fig. 3.8(b) and (c), respectively. The triboelectric part in hybrid energy harvester (type 2) generated voltage from the friction between G-HIP and PET, which results from the piezoelectric energy harvester (type 1) when it was bent and recovered to generate voltage. The generated voltages of the piezoelectric part and the triboelectric part are 2 and 5 V, respectively. This type of device can be used in shoes

soles to generate a certain voltage and support electric loads, or monitor steps as gait analysis as shown in Fig. 3.9.

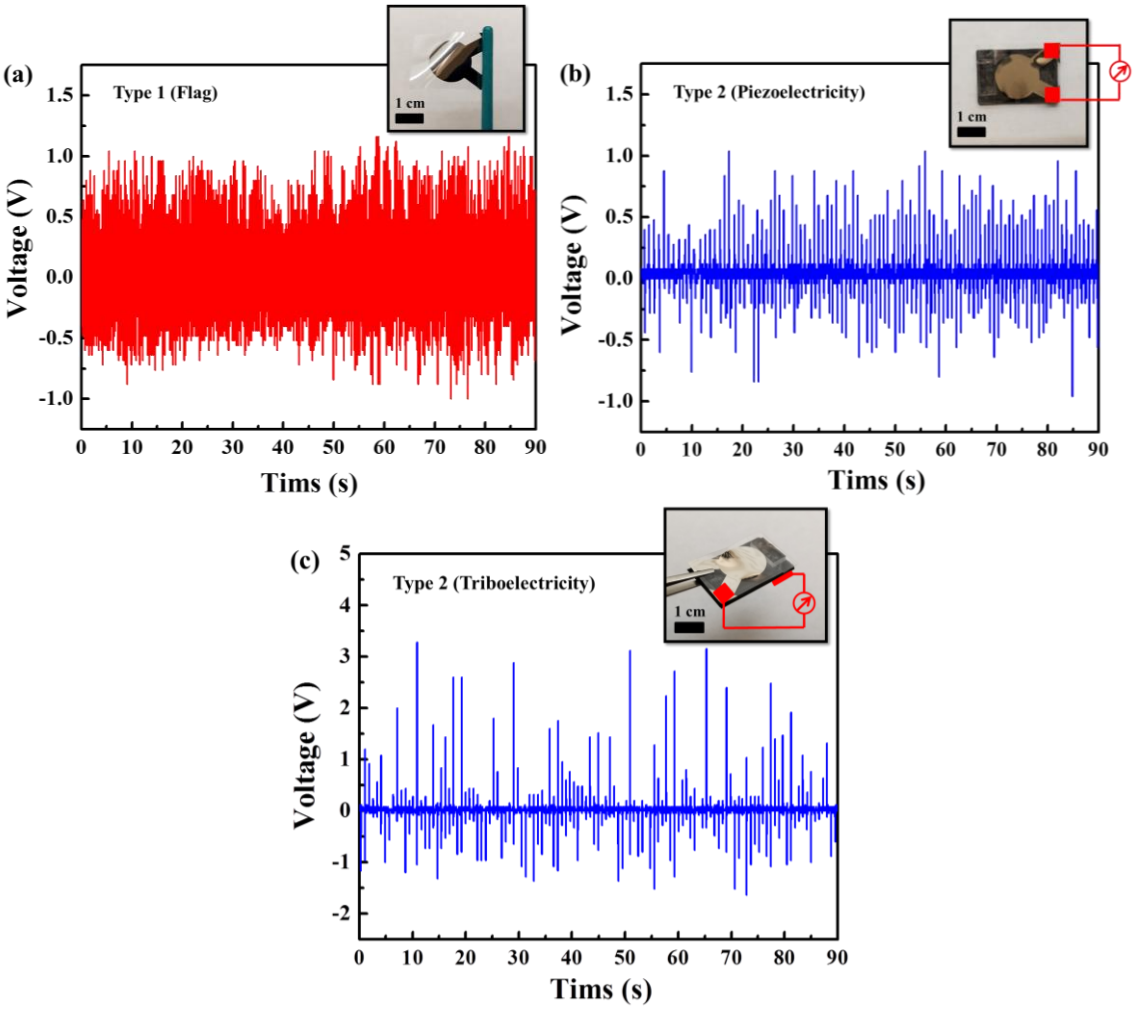

Figure 3.8 (a) Output voltage of type 1 under wind power, (b) output voltage of piezoelectric part, and (c) triboelectric part in type 2 under mechanical force.

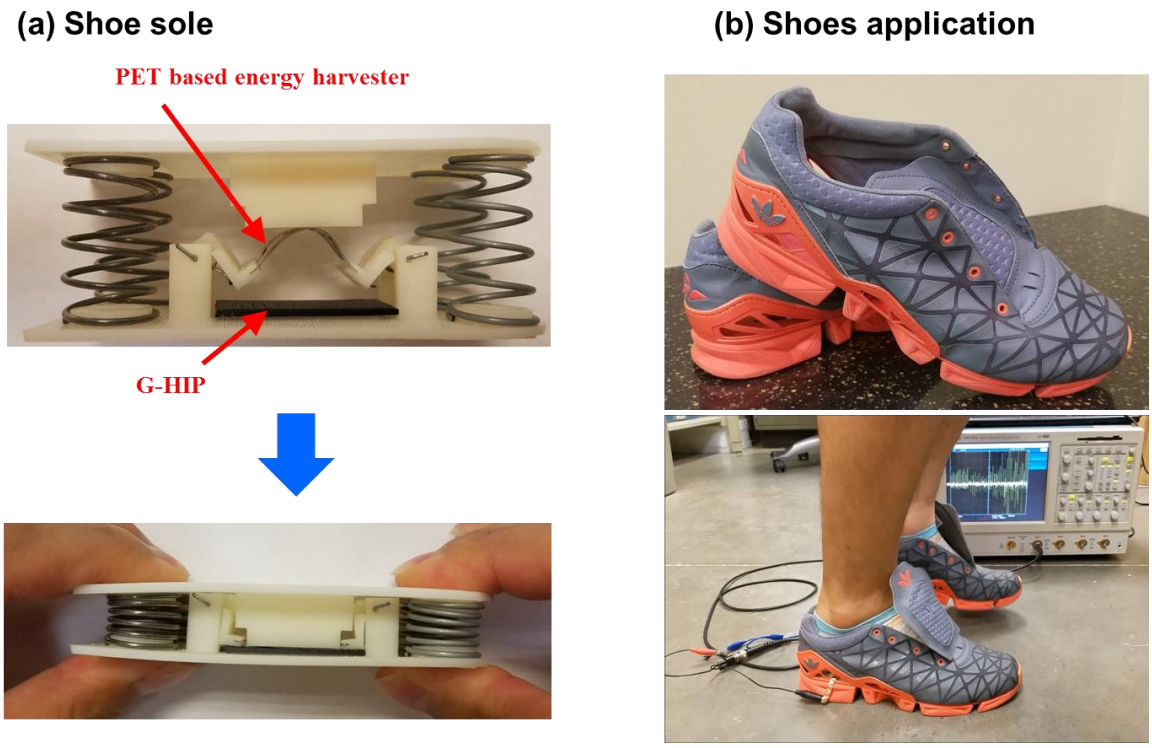

Figure 3.9 (a) A photo image of 3D printed shoe sole for hybrid structure based energy harvester, (b) demonstration of shoes application by hybrid structure based energy harvester with shoe sole.

3.1.5 Conclusions

In this work, we have demonstrated a highly flexible, biocompatible PDMS-based piezoelectric energy harvester with P(VDF-TrFE) film utilizing a simple fabrication process. The device with an active area of 4 cm2 was found to have a power density of 6.62 mW/cm^3 and average voltage and current of 5.8 V and 3.2 μA, respectively at 30 Hz vibration frequency at 1.75 g acceleration. Using a full wave bridge rectifier, a capacitor was charged and could deliver 370 nW, which was capable of lighting 27 LEDs

simultaneously. With this power output, a wide range of wearable electronics and smart monitoring devices are within the realm of possible applications. In spite of the simple design, the performance of the present device was found to be superior compared to other flexible energy harvesters on PDMS substrate.

We have also developed the piezoelectric energy harvester on PET substrate to solve metal contact issue for PDMS based energy harvester. Under severe bending and vibration condition, the device generated a voltage uniformly. Furthermore, the hybrid energy harvester (i.e., based on piezoelectric and triboelectric) was fabricated with P(VDF-TrFE) (spin-coating) and G-HIP (3D printing). It was successfully generated few voltages by various stimuli such as wind and tapping, which highlight the feasibility of multiple energy harvesting applications such as flags in renewable technology and shoes soles in wearable electronics.

CHAPTER FOUR

SENSING APPLICATIONS OF GRAPHENE/P(VDF-TRFE) HETEROJUCTION ON FLEXIBLE SUBSTRATES

4.1 PDMS substrate based sensor

The world of wearable technology is making use of strain and pressure sensors in human monitoring and the use of data can range from improving the lifestyle of people to using it in the workplace for improving safety. High sensitivity, fast response time, low-pressure range of operation, low cost and simplicity of the fabrication process are the preferred attributes in strain/pressure sensors. We have developed a highly sensitive strain/pressure sensor based on PDMS, P(VDF-TrFE), metal electrode, and monolayer graphene. The device is very responsive to even small differentials of pressure mainly because there are multiple factors contributing to the response. The piezoelectric nature of P(VDF-TrFE), the structure of metal electrode, lower Young's modulus of the PDMS, and monolayer graphene contribute in making the device highly responsive even under small stimuli. The sensor demonstrates high sensitivity (average = 0.76 kPa^{-1}, maximum = 0.89 kPa^{-1}, and gauge factor = 481.6) in the range of pressure up to 45 mmHg. The sensor has low detectable strain of 0.016%, SNR of 26.4 dB, and a fast response time of ~100 ms. These features, coupled with the flexible nature of the device and ease of fabrication, make it a very attractive candidate for use in the growing wearable technology market, especially biomedical applications and smart monitoring systems.

4.1.1 Introduction

Highly sensitive, flexible and conformable strain/pressure sensors have attracted tremendous research interest in recent years for their applications in health care [121,122], gait analysis [123,124], and smart monitoring systems [125,126], Several material systems and device configurations have been investigated to develop these types of sensors including, piezoelectric (i.e. ZnO thin films and nanowires [127,128], BaTiO3 thin films and composites [129,130], PVDF and PVDF-TrFE [131,132]), piezoresistive (thin Si [133,134] piezoresistive polymer [135,136], or carbon nanotube based [137,138]), transistive, (integrating a flexible transistor as a sensing element [139-142]) and capacitive [143-145]. Although, several of these approaches are promising, and results in high sensitivity devices [138-144], they are either not completely flexible and conformable [139,141,142], or suffer from complex and expensive fabrication process [138,139,140,143,144]. On the other hand, graphene, with its outstanding material properties, including high carrier mobility, atomically thin nature, and ability to tolerate mechanical deformation related strain up to 20% before breaking [146,147], making it very attractive for developing highly sensitive and conformable strain/pressure sensor. Unfortunately, graphene by itself is not piezoresistive, so developing a strain sensor utilizing just graphene is challenging. Fortunately, graphene synthesized on Cu foil can be transferred to arbitrary substrates (preserving its high quality), including flexible polymer substrates, which will allow the overall flexibility and conformability of the sensing element, to be maintained. Furthermore, a graphene/polymer based sensor devices can be easily patterned into an array over dimensions reaching several feet, taking advantage of large area synthesis of graphene, which will make the ultimate sensor

very inexpensive. If a piezo-electric polymer, such as P(VDF-TrFE), is chosen to form a heterojunction with graphene, it will strongly affect the carrier density in graphene, due to the fixed charge developing on its surface under strain or pressure. Taking advantage of the high carrier mobility in graphene, such a charge change can result in very high sensitivity to pressure and strain.

For mechanical stability and ease of handling, the sensing layer normally needs to be put on a flexible substrate. To date, strain/pressure sensors have been fabricated on a variety of flexible substrates including polyethylene terephthalate (PET) [139], polyethylene naphthalate (PEN) [148], polycarbonate (PC) [149], and polyurethane (PU) [150] for flexible and wearable electronics due to their high optical transparency (except for PU), ease of use, and superior durability. In addition, other type of substrates, such as, polydimethylsiloxane (PDMS) [144], EcoFlex [151], DragonSkin [152], and hydrogel [145] have recently attracted extensive interest for developing "skin electronics" because of their unique properties of high deformability, along with chemical inertness and biocompatibility. In particular, these substrates support superior conformability on any geometry and are able to attach well to skin, during deformation and recovery, making them strong candidates for flexible substrate. Among these, PDMS combines the advantages of relatively high operational temperature (up to 350 ℃), high permeability to oxygen, ease of molding, compositional control, and low Young's modulus [153-155]. Thus, very high sensitivity can be obtained (especially for low pressure operation) for sensor devices integrated on PDMS substrates, making it very attractive for biomedical [156] and artificial skin [157] applications. Examples of high

sensitivity PDMS based sensors include demonstration of a sensitivity of 0.7 kPa^{-1} in a capacitive sensing configuration in the low pressure regime (2.5 Pa ~ 20 kPa) [144], and organic field-effect transistors (OFET) based sensor with microstructured PDMS as a gate dielectric layer with sensitivity up to 0.55 kPa^{-1} [140].

In this work, we report on the development of an ultra-high sensitivity pressure sensor by marrying the high deformability of PDMS substrate with the high responsivity of the graphene/PVDF-TrFE composite. Although there are many reports on P(VDF-TrFE) based sensors including several on PDMS substrate, there is only one other report to our knowledge that utilized graphene and P(VDF-TrFE) together in the sensor configuration. Sun et. al. [139] developed graphene transistor based sensor that is gated by piezopotential generated across a P(VDF-TrFE) film, which was coupled to the graphene transistor channels via an ion gel. The strain sensor resulted in a gauge factor (GF) of 389, which is one of the highest ever reported on a flexible substrate. However, this sensor suffers from fabrication complexity, ion gel charge coupling issues that includes limited response time and device lifetime. In contrast, our sensor directly couples the charge generated by the P(VDF-TrFE), much easier to fabricate, have lower thickness, and do not have gel lifetime issues, and exhibited significantly superior performance including ultra-high sensitivity (average = 0.76 kPa^{-1}, maximum = 0.89 kPa^{-1}) and gauge factor = 481.6. A theoretical model, supported by COMSOL Multiphysics simulation, has been developed to explain the device performance.

4.1.2 Experimental details

Fabrication of the flexible and self-powered strain/pressure sensor

To fabricate the sensor device, we separately optimized the PDMS substrate and the P(VDF-TrFE) piezoelectric polymer, and utilized high quality graphene synthesized on Cu foil through a well-developed recipe in our lab [158-160]. The sensor was fabricated following the sequential steps shown in Fig. 4.1.1, and is described in detail below.

Preparation of PDMS substrate

The preparation of liquid PDMS was done by mixing elastomer with a cross linker (Sylgard 184 silicon elastomer kit) in the weight ratio 10:1, followed by degasing to remove bubbles in a vacuum desiccator for 1 h. In the first step of the fabrication process, liquid PDMS was spin-coated at 800 rpm for 20 s on a rectangular copper plate (2.5 cm (W) x 2.5 cm (L) x 0.0175 cm (H)) (Fig. 4.1.1(a)) to make the PDMS substrate on top of it. After spin-coating, it was heated at 100 ℃ for 30 min in ambient conditions, which was followed by deposition of the the bottom electrode for the sensor (radius = 0.8 cm), Ti/Ni (30 nm/150 nm) at 100 ℃ by electron beam evaporation on the PDMS/Cu (Fig. 4.1.1(b)). In the fabrication process, thermal treatment plays an important role to improve the conductivity and homogeneity of the Ti/Ni metal stack deposited on the PDMS. Since the PDMS substrate was stretched while it was exposed to heat (and the Cu substrate underneath spreads the heat uniformly), which also allowed the Ti (first metal, 30 nm) to permeate into the PDMS, the subsequent Ni layer (second metal, 150 nm)

deposition led to the overall metal electrode contact to become more stable and reliable during repeated bending and stretching from external strain.

Preparation of P(VDF-TrFE) film

A solution of P(VDF-TrFE) was prepared by dissolving Co-polymer powder of P(VDF-TrFE) (50/50, Piezotech) in *N*,*N*-dimethylformamide (DMF) solvent and stirring for 12 h at 40 ℃ to synthesize 13 wt % of P(VDF-TrFE) solution. The prepared solution of P(VDF-TrFE) was then spin-coated on the Ni/Ti/PDMS/Cu at 6500 rpm for 60 s to obtain a thickness of 2 μm as shown in Fig. 4.1.2(a), and was dried at 60 ^{o}C for 10 min to remove the DMF solvent. The P(VDF-TrFE) film on the Ni/Ti/PDMS/Cu was subsequently heated in air at 140 ^{o}C for 2 h to develop the β-phase of P(VDF-TrFE), (which is it's most stable form with the highest piezoelectric constant) [31-36] followed by natural cooling to room temperature (Fig. 4.1.1(c)). Another layer of Ti/Ni (30 nm/150 nm) was deposited to form the top metal electrode (in the form of two semicircular halves of 7 mm radius, with a gap of 2 mm in between), by e-beam evaporation as shown in Fig. 4.1.1(d)). After that, the Cu layer was removed from underneath of the overall device structure by dissolving in a solution of 0.5 M ammonium persulfate as shown in Fig. 4.1.1(e). The device was floated in the solution while Cu layer was etched. After that, the bottom of floated device (PDMS substrate) was rinsed multiple times in deionized (DI) water. Although not shown as a formal step in Fig. 4.1.1, a very important part of the fabrication process is poling of the P(VDF-TrFE) film to align the dipoles to an external electric field. These aligned dipoles will generate fixed surface charge when the film is

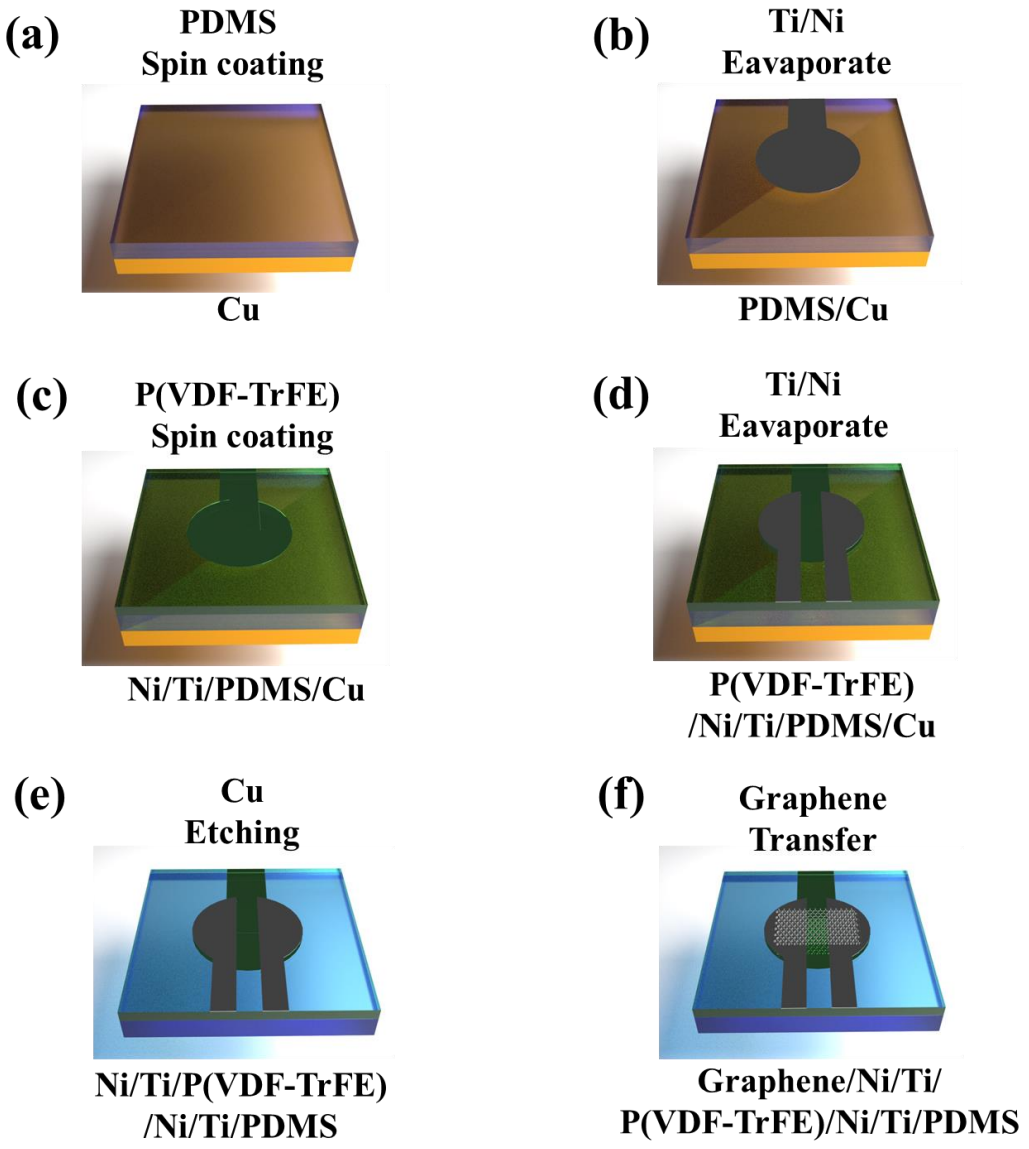

Figure 4.1.1 Schematic demonstration of the processes in fabrication of the sensor. (a) PDMS was spin-coated on Cu. (b) Deposition of Ti/Ni as bottom electrode using electron beam evaporator. (c) P(VDF-TrFE) was spin-coated on Ni/Ti/PDMS/Cu. (d) Deposition of Ti/Ni as top electrode using electron beam evaporator. (e) Removing Cu from Ni/Ti/P(VDF-TrFE)/Ni/Ti/PDMS/Cu using ammonium persulfate etchant. (f) Transferring graphene on Ni/Ti/P(VDF-TrFE)/Ni/Ti/PDMS.

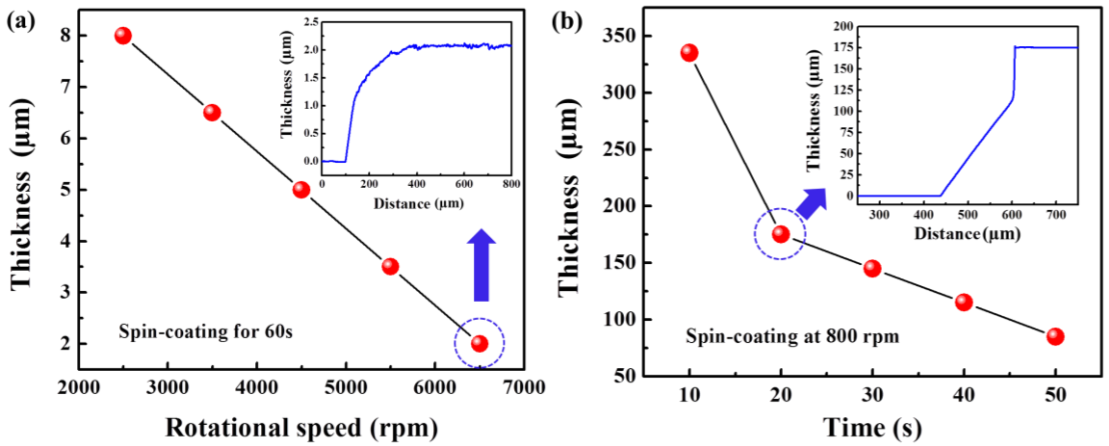

Figure 4.1.2 (a) Various thickness of P(VDF-TrFE) films by spin-coating at different rotational speed for 60 s. The inset shows the thickness of P(VDF-TrFE) at 6500 rpm. (b) Various thickness of PDMS by spin-coating at 800 rpm for different time. The inset shows the thickness of PDMS for 20 s.

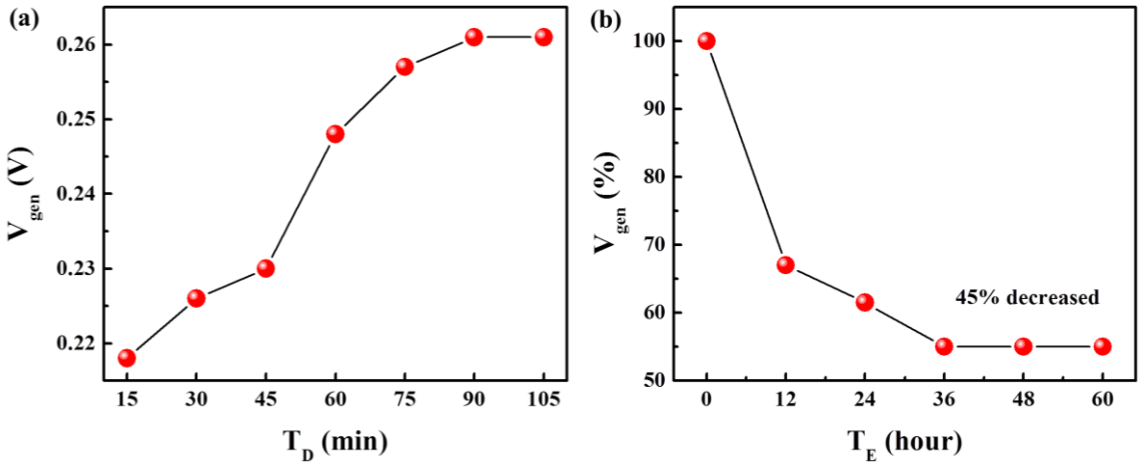

Figure 4.1.3 (a) Voltage generated (V_{gen}) vs time duration of poling (T_D), and (b) Voltage generated (V_{gen}) vs time elapsed after polling (T_E)

subjected to external strain, the magnitude of which directly affects sensitivity of the overall device. Poling of the P(VDF-TrFE) was performed by subjecting it to an electric field of 100 MV/m for 1 hour, by applying a voltage of 200 V across the Ti/Ni metal layer underneath, and the two halves of the Ti/Ni metal layer connected at the top. The one hour duration was found to be optimal and further increase in time up to 2 hours only resulted in less than 5% increase in the voltage generated across the film when similarly strained. The plot of voltage generated V_{gen} vs. T_D (duration of poling) is shown in the supplemental Fig. 4.1.3(a). Additionally, it should be noted that the degree of alignment of the dipoles decreases with time after the poling. In Fig. 4.1.3(b) we show the V_{gen} (under similar strain) vs. T_E (the time elapsed after poling), which indicates that the degree of poling reduces with time, but at a decreasing rate, and becomes steady after a few days at a value of ~55% of the maximum value achieved immediately after poling. This observation of decrease in the degree of poling and percentage of steady state value is consistent with earlier reports [164,165,166].

Synthesis and transfer of graphene

In the next step, high quality monolayer graphene, synthesized through an optimized chemical vapor deposition (CVD) process, was transferred onto the Ni/Ti/P(VDF-TrFE)/Ni/Ti/PDMS layer structure using a wet transfer process developed in our lab (Fig. 4.1.1(f)). Details of the CVD synthesis and transfer process of graphene are discussed in detail elsewhere [158-160]. Briefly, graphene was grown on a copper foil (which acted as the substrate as well as the catalyst) at 1035 ^{o}C for 20 min using CH_4 as

the precursor gas after the Cu foil was baked out in Ar environment at 250 ^{o}C followed by a 2 hour anneal at 1000 ^{o}C. The wet transfer process involved 2 layers of PMMA coating of the graphene by spin-coating at 2000 rpm for 60 s, followed by oxygen plasma etch from the backside graphene grown on the Cu foil, which was then followed by Cu removal by etching in the solution of 0.5 M ammonium persulfate. The floated PMMA/graphene was rinsed multiple times in DI water, and then the PMMA/graphene can be transferred on the device as shown in Fig. 4.1.1(f). The device with transferred PMMA/graphene was dried at 40 ^{o}C for 10 min in air. Finally, the coated PMMA was removed from top of transferred graphene by few droplets of 1,2-dichloroethane (99%, Alfa Aesar).

Measurement and characterization

The structural and optical transmission properties of the P(VDF-TrFE) were investigated using Fourier transform infrared (FTIR) spectroscopy (Model # Thermo Scientific Nicolet380), X-ray diffraction (XRD, Model # Rigaku ULTIMA IV). The graphene was characterized using Raman spectroscopy (Model # CrystaLaser CL-2000) to determine its quality and verify monolayer nature. The carrier mobility and density in the graphene in the device layer structure were measured by a Hall Effect measurement system (Model # Ecopia HMS3000) both in relaxed condition and under external strain of 0.0075. The performance of the sensor was measured by attaching it to a printed circuit board (PCB), specifically designed to hold the sensor, and utilizing a data acquisition unit (Agilent 34970A) to collect the data and store it in computer. A semi-

automatic wire/ball bonder from Kulicke and Soffa (Model # KS 4524A) was used to make gold wire bonds between the PCB pads and the Ti/Ni contacts of the sensor device.

Monitoring of human activities with wireless data transmission

To monitor human movement using the sensor, a circuit board from Adafruit (Model # ESP8266MOD) was used to collect the data and transmit through Wi-Fi in real-time, while the movement was performed. The data was transmitted from the sensor every 5 secs using the ESP8266 Wi-Fi module which used the message queuing telemetry transport (MQTT) protocol for transmitting the data. The response of the sensor was read in terms of variation of voltage across a 10 kΩ resistor connected in series with the sensor. The sensor resistance varied with application of an external strain or pressure, which altered the voltage across the 10 kΩ resistor that was read on the analog pin of the ESP8266 chip, and subsequently transmitted to cloud. The maximum range of analog voltage across the 10 Kohm resistor (0 to 3.3 V), and was mapped between 0 and 1024 by a 10 bit analog to digital converter (ADC) in the ESP8266 Wi-Fi module. These ADC values were then sent to the cloud and to be plotted on the Y-axis of the response graph (as a function of time), which will be discussed later.

4.1.3 Results and discussion

Figures 4.1.4(a) and (b) show schematic views of the strain/pressure sensor and its layer structure. As discussed above, the sensor consists of five layers: the PDMS substrate, the Ti/Ni top and bottom contact electrodes, the P(VDF-TrFE) film, and

graphene. The thickness of PDMS substrate is one of the most important parameters for sensor design, since it determines the range of force/strain that can be applied (dynamic range) without damaging the physical structure, as well as, critical device attributes such as sensitivity. While thinner PDMS substrate results in higher sensitivity as it experiences higher deformation for a given magnitude of external force/strain, it also limits the dynamic range by making the PDMS metal electrode more susceptible to damage. The maximum applicable strain in PDMS without introducing significant cracks in the metal layer deposited on top, is reported to be ~0.8 % [167,168], and in a previous study we found that the thickness of PDMS of ~175 µm will result in a maximum strain of ~0.8 % for an applied pressure of ~50 mm Hg for a square membrane with sides of 3 mm [153]. Since a comparable diameter of 5 mm was used in this study, the thickness of PDMS substrate was chosen to be 175, to simultaneously achieve the high sensitivity as well as good dynamic range. The Ti/Ni as the top and bottom electrodes and P(VDF-TrFE) as active film were deposited on the PDMS substrate sequentially, and a monolayer graphene was transferred on top of them. A top view schematic is shown in Fig. 4.1.5(b), while Fig. Fig. 4.1.5(c) shows photos of the fabricated device as it is laid flat and is folded (using a tweezer, which underlines its flexibility) across the diagonal. Top view, optical microscope image of the sensor is shown in Fig. 4.1.5(d). The cracks seen at the center of the optical image in Fig. 4.1.5(d), is formed on the bottom electrode, during its deposition on the PDMS substrate and deformations afterwards. Despite the presence of cracks, the bottom electrode shows good electrical continuity as shown in Fig. 4.1.5(e), where the current-voltage characteristics of both the top and bottom electrodes are plotted

by applying voltage across two point contacts established at the ends of the metal contact pads.

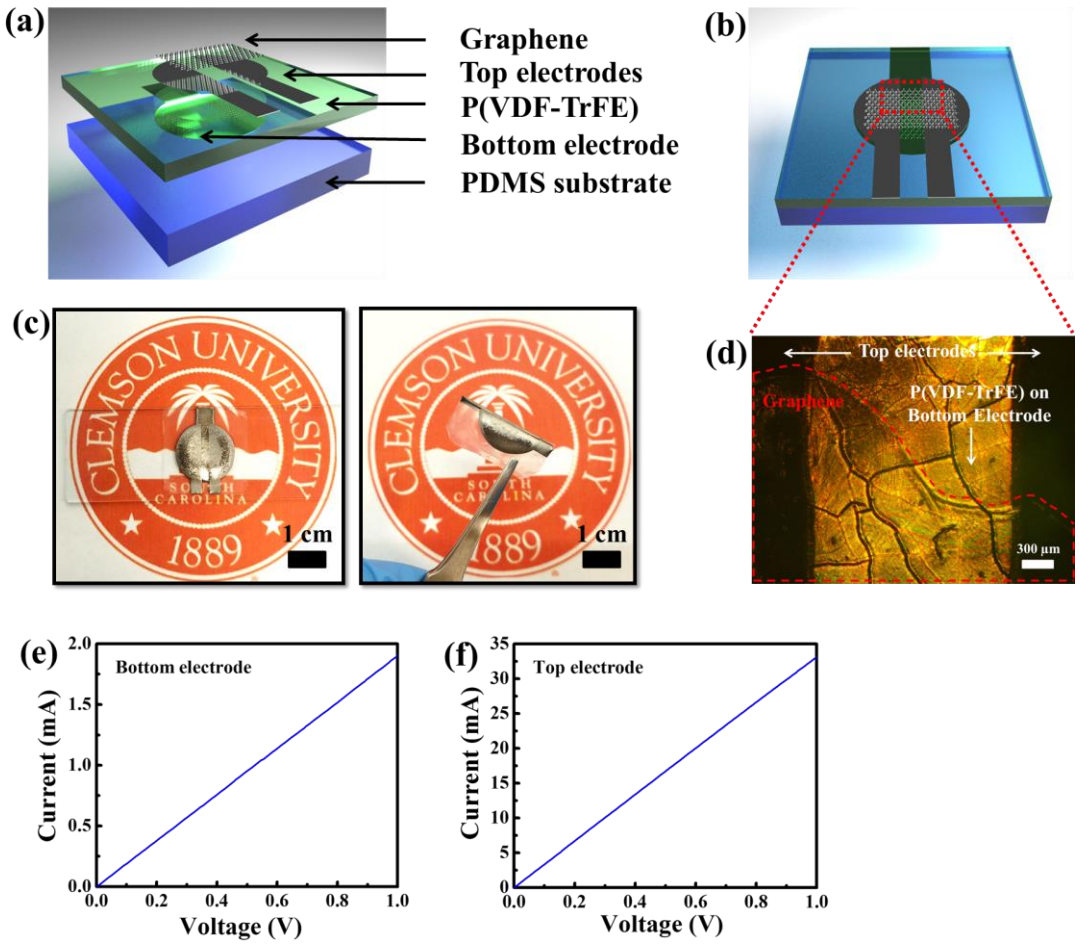

Figure 4.1.4 (a) and (b) show schematic illustrations of the design, (c) photographic images, and (d) optical microscopy image for the sensor. (e) and (f) show the electrical continuity of bottom electrode and top electrode on the sensor, respectively.

The structure of the P(VDF-TrFE) film was confirmed using FTIR spectroscopy. Figure 4.1.6(a) presents the FTIR spectrum of the P(VDF-TrFE) film at room temperature. Presence of the three absorption peaks at 840, 1290, and 1400 cm^{-1} correspond to the CH_2

rocking, trans band, and CH_2 wagging, respectively, for the β-phase of the P(VDF-TrFE) film, confirming its formation [33,104]. In addition, the observation of diffraction peak at

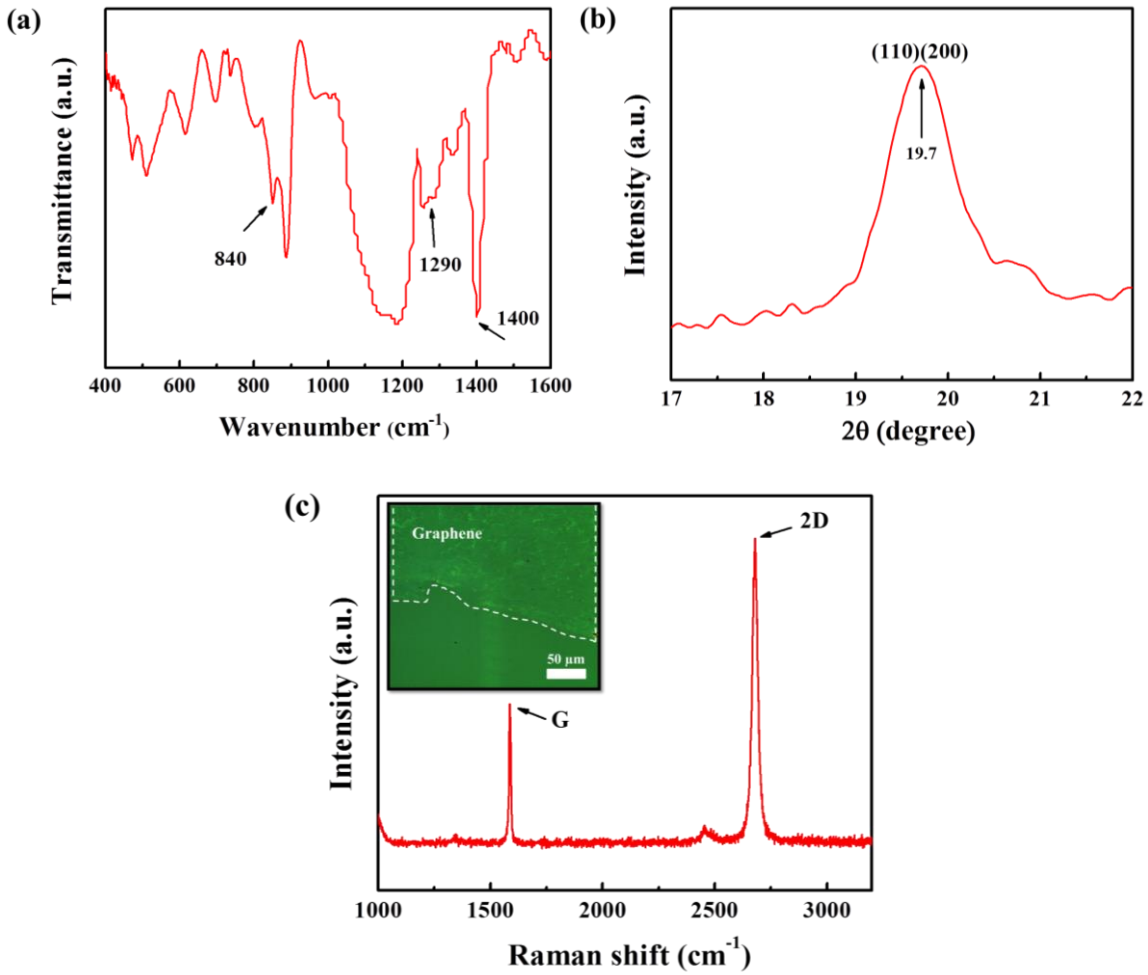

Figure 4.1.5 (a) FTIR and (b) XRD result of β-phase of P(VDF-TrFE) film. (c) Raman spectrum of graphene after transferred on SiO_2/Si substrate and the inset shows the optical image of the graphene.

$2\theta = 19.7^{o}$ (Fig. 4.1.6(b)), which is generally attributed to the orientation planes (110) and (200) for the polar β-phase [81,103] of P(VDF-TrFE), once again confirms its formation.

Therefore, we conclude that our synthesis method yielded high crystalline quality β-phase of P(VDF-TrFE) film, as desired. Figure 4.1.6(c) presents the Raman spectrum of a typical graphene layer transferred on SiO_2/Si substrate, while the inset shows an optical image of the graphene layer (demarcated by the white dashed line). From the Raman spectra, the ID/IG ratio is calculated as 0.13, which indicates very low defect density in the transferred graphene. In addition, the I_{2D}/I_G ratio is calculated to be 2.1, which along with the FWHM (2D peak) of 26.7 cm^{-1}, clearly indicates the presence of monolayer graphene [169]. To investigate the electrical properties, including sheet carrier density and mobility, on graphene transferred to PDMS substrate, Hall measurements were performed on it by putting indium press contacts at the four corners. The results are shown in Table 4.1.1. The Hall mobility and carrier density were found to be 3120 cm^2/Vs and and 9.1×10^{11} cm^{-2}, respectively, which is indicative of high quality of the graphene layer [170].

Table 4.1.1 Characterizations of graphene such as mobility, sheet carrier density, and sheet resistance.

Graphene on	Mobility (cm^2/Vs)	Sheet carrier density (cm^{-2})	Sheet resistance (Ω/sq)
SiO_2/Si	3120	9.1×10^{11}	2.3×10^3

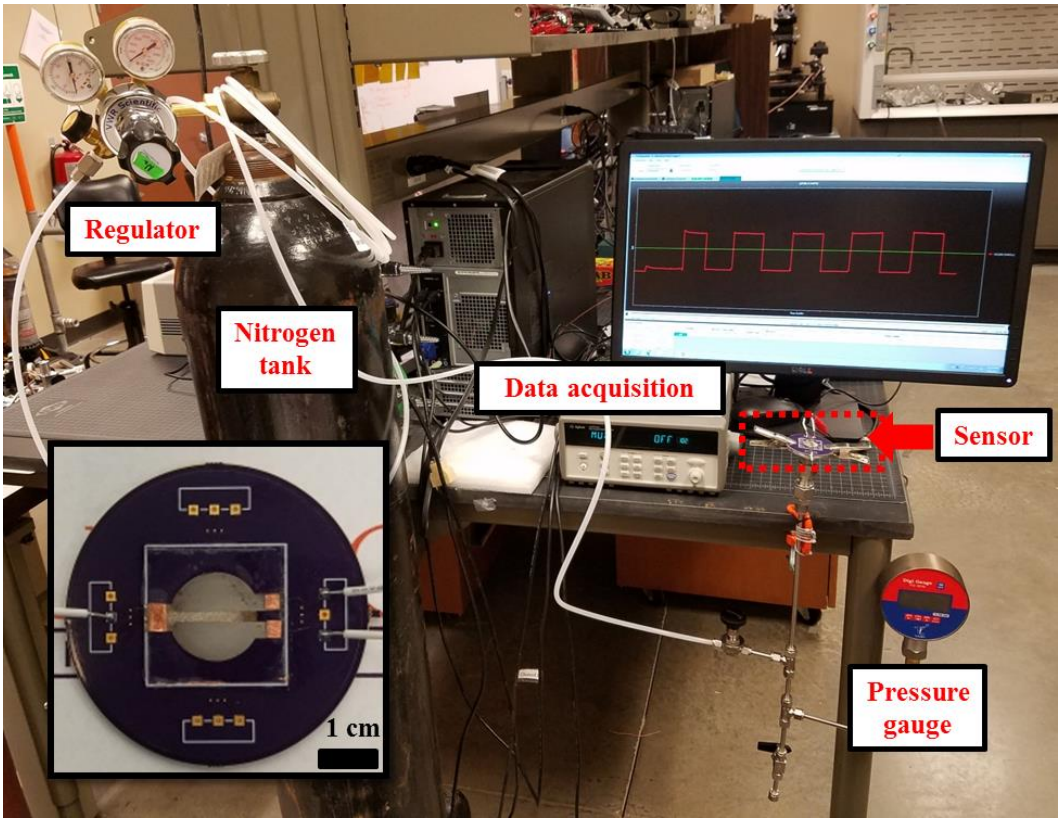

Figure 4.1.6 Photographic image of the basic measurement setup and inset shows image of the sensor mounted on the PCB.

Figure 4.1.6 shows a picture of the measurement setup, which basically consists of a computer controlled data acquisition system (Agilent 34970A), a nitrogen tank to apply gaseous pressure, the sensor connected to the gas line from the tank, and a gauge (Yash Flowmeters YG309) to measure the applied pressure. The inset shows a photo of the sensor attached to a custom built printed circuit board (PCB) designed using EAGLE software. The PCB terminals were connected to the Ti/Ni metal contact pads on the sensor using Au wire bonds put in place using a semi-automatic wire/ball bonder. The output of the sensor, which simply constitutes the resistance change of the graphene strip

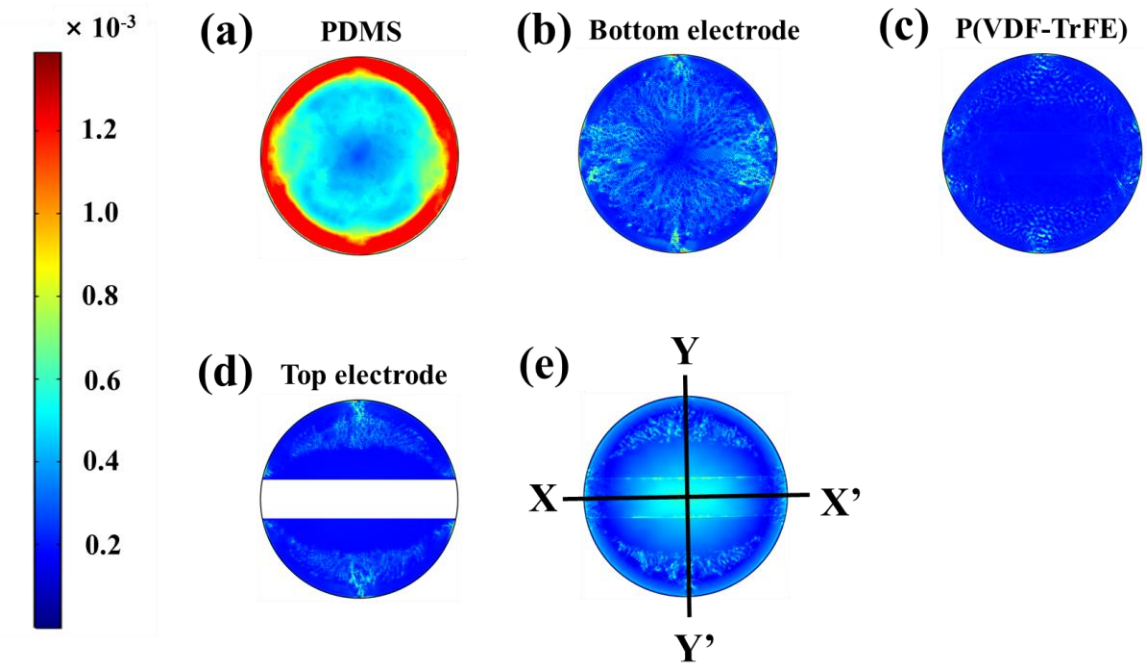

Figure 4.1.7 COMSOL simulation of strain distribution on the active area (diameter = 10 mm) on each layers such as (a) PDMS substrate, (b) bottom electrode, (c) P(VDF-TrFE) film, (d) top electrode, and (e) entire structure of the sensor.

between the semicircular metal contact pads, was recorded for various pressures up to 45 mmHg in small steps of a few mm Hg. The pressure applied to the sensor was manually adjusted using the pressure regulator on the nitrogen tank.

In order to determine the performance parameters of the sensor (see discussion below) we need to determine the strain distribution on the graphene sensing element due to applied pressure. The stress and strain distribution across the sensor membrane (radius = 5 mm) was simulated using COMSOL finite-element simulation (Solid Mechanics module) software. The outer edge of the active area was assumed to be fixed for the

simulations, and a uniform pressure of 15 mmHg (2 kPa) was assumed to be applied on the bottom surface of the membrane. Figure 4.1.7 shows the strain distribution for the P(VDF-TrFE) layer of the sensor, which is responsible for producing electrical charge in response to strain. The strain distribution in the PDMS, bottom electrode and the top electrode are included in the Fig 4.1.7. These values will be used to calculate the gauge factor for the sensor as discussed below.

Figure 4.1.8(a) shows the change in resistance with externally applied pressures for the sensor. The sensitivity (S) of a sensor is generally calculated from the equation

$$S = (\Delta R/R_o)/\Delta P, \quad (1)$$

where ΔR is the change in resistance, R_o is the original resistance, and ΔP is the change in applied pressure on the sensor. The slope of the least square line fitted to the $\Delta R/R_o$ vs. ΔP plot in Fig. 6 gives the average sensitivity over the entire range of pressure of 45 mmHg. The response of the sensor is quite linear and the value of sensitivity is obtained as 0.101/mmHg (0.76/kPa) which is one of the best values reported on graphene based strain/pressure sensors with PDMS or P(VDF-TrFE) substrates as can be seen from Table 4.1.2. The Gauge Factor (GF) of the sensor can be calculated to compare the performance of the sensor with other strain sensors. This allows a more direct comparison between technologies, since possible variation in strain due to dimensional variations is accounted for. The GF of the sensor calculated from the equation $GF = (\Delta R/R_o)/\varepsilon_{av}$, turns out to be 481.6 using the average values of strain in these directions calculated above, and using a fractional change is resistance $\Delta R/R_o = 1.5$ for an applied pressure of 15 mmHg. The resulting value of GF is at least an order of magnitude higher than those of the flexible

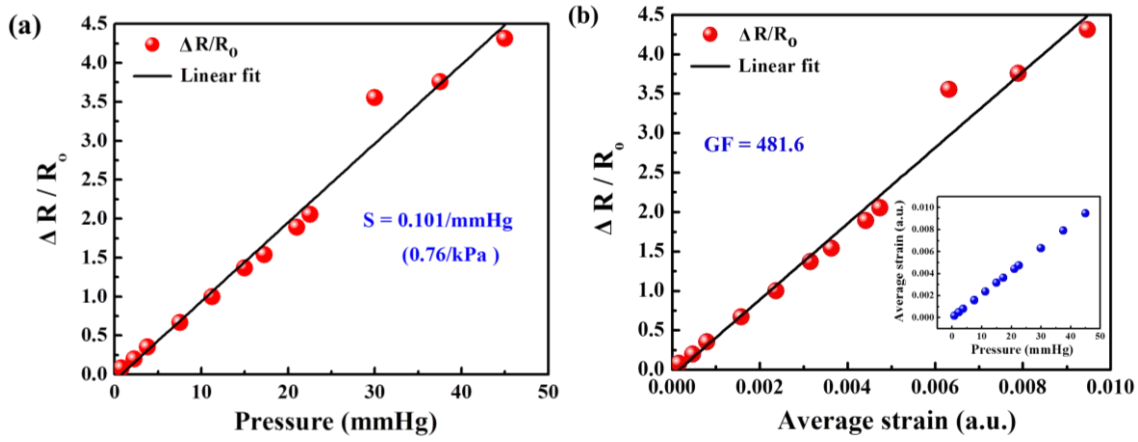

Figure 4.1.8 Relative change in resistance with applied (a) various pressures and (b) average strain for the sensor. The inset shows average strains versus various pressures, computed by COMSOL simulation.

strain sensors reported so far as shown in Table 4.1.2, which clearly highlights the benefits of using a graphene/ P(VDF-TrFE) composite to perform highly sensitive detection of strain, pressure or force.

The ultra-high sensitivity of our sensor device originates in the graphene/P(VDF-TrFE) heterostructure composite. Poling of the P(VDF-TrFE) film causes its C-H and C-F bonds in graphene/P(VDF-TrFE) to orient their positive and negative charges along the direction of applied poling field, resulting in a net polarization in the film [24,171]. This net polarization varies in strength under the influence of mechanical strain which induces a change in carrier density in graphene. CVD grown graphene is typically p-type when transferred to different substrates, which can be attributed to the presence of charged surface impurities during wet-etching of copper and subsequent transfer process on

Table 4.1.2 Sensor performance comparison of PDMS, P(VDF-TrFE), and graphene based strain/pressure sensors reported in recent years.

Active materials	Sensing Type	Active area (cm^2)	Measurement range (Pa) Detection range (%)	Output performance GF Sensitivity (kPa^{-1})
Graphene/ P(VDF-TrFE)/ Metal/ PDMS	**Piezoresistive [This work]**	**0.785 cm^2**	**0.1 kPa ~ 6 kPa 0.016 ~ 0.95 %**	**481.6 0.76 kPa^{-1}**
P(VDF-TrFE)/ $PbTiO_3$ FET	Piezoelectric [Ref. 141]	-	2 MPa ~ 22 Mpa	-
Air gap/ porous PDMS	Capacitive [Ref. 144]	1 cm^2	2.5 Pa ~ 20 kPa	0.7 kPa^{-1}
Pyramid-shaped PDMS microhairy	Capacitive [Ref. 143]	Microhair (Diameter = 30 μm)	~ 5 kPa	0.58 kPa^{-1}
Microstructured PDMS OFET	Capacitive [Ref. 140]	0.64 cm^2	3 Pa ~ 20 kPa	0.55 kPa^{-1}
CB/PDMS composite	Piezoresistive [Ref. 136]	Ribbon-shaped (Width: 300μm Length: 2cm)	~ 80 %	~ 5.5
CB/PDMS composite	Piezoresistive [Ref. 135]	-	~ 150 %	29.1
P(VDF-TrFE)/ graphene transistor	Piezoelectric [Ref. 139]	-	0.008 ~ 0.20 %	389
P(VDF-TrFE)/ $BrTiO_3$ FET	Piezoelectric [Ref. 142]	-	0.1 MPa ~ 0.5 MPa	2.615 mV kPa^{-1}
P(VDF-TrFE) nanofiber	Piezoelectric [Ref. 132]	0.18 cm^2	0.1 Pa ~ 12 Pa	0.41 V Pa^{-1}
Graphene/ PU sponge	Piezoresistive [Ref. 177]	0.04 cm^2	9 Pa ~ 10 kPa	0.26 kPa^{-1}
Coplanar gate graphene FET	Piezoresistive [Ref. 178]	-	5 kPa ~ 40 kPa	0.12 kPa^{-1}
Graphene woven fabric	Piezoresistive [Ref. 179]	36 cm^2	~ 2 %	35

various substrates. The p-type nature of the graphene layer transferred on P(VDF-TrFE) was confirmed from Hall measurements, as discussed below. Figure 4.1.9(a) schematically shows that as the graphene/P(VDF-TrFE) layer is subjected to strain, a differential positive surface charge $+\Delta\sigma$ is generated on the P(VDF-TrFE) top surface (this is the side that graphene is deposited). This positive charge repels holes in graphene reducing its p-type nature. On the other hand, the bottom side of the P(VDF-TrFE) undergoes a compressive strain, forming a differential negative surface charge $-\Delta\sigma$, which induces a positive charge on the bottom metal electrode. The total top surface charge becomes a stronger positive (σ++), and the total bottom charge becomes a stronger negative charge (σ--). As the hole density is reduced, the Fermi level of graphene moves upwards compared to the unstrained graphene, as shown in the bottom panel of Fig.4.1.9(a). Such a reduction in hole density resulted in an increase in resistance as observed in Fig.4.1.10 (as discussed below the mobility also decreased significantly leading to a much higher variation in resistance than simply carrier density change). The increased resistance was maintained in the strained graphene, and returned back to its original value when the P(VDF-TrFE) film was allowed to relax. We note here once again that by utilizing the graphene/P(VDF-TrFE) composite, we have converted a piezoelectric sensing element (P(VDF-TrFE) by itself) to an ultra-high sensitivity piezoresistive sensing element that can be used much more easily to transduce pressure, and which can respond accurately to step and low frequency changes very accurately.

To independently verify the change in carrier density in graphene induced by strain in P(VDF-TrFE), we performed Raman spectroscopy on the device, in strained and

unstrained conditions, since variation in carrier density is correlated with the G-peak shift in the Raman spectrum. Figure 4.1.9(b) shows the spot was chosen to perform the Raman spectroscopy measurements. The top panel in Fig.4.1.9(b) (black line plot) indicates the G-peak before bending, and bottom panel (red line plot) shows the G-peak after the device was subjected to strain. The Raman shifts of G-peak for before and after bending were found to be 1588 and 1578 cm^{-1}, respectively. A red shift in the G-peak confirms the upward movement of the Fermi level for graphene under strained condition [172, 173], which supports the electrical measurements discussed above.

Figure 4.1.10(a) shows the response and relaxation times of the sensor which is corresponding to the pressures on and off, respectively. The pressure was adjusted manually on nitrogen tank from 0 to 15 mmHg in this measurement and it was kept at 15 mmHg for 20 s and then released to 0 for 20 s. It is clear that the performance of the sensor is very consistent over the various cycles. Figure 4.1.10(b) presents a single pulse of response (pressure on) and relaxation (pressure off) times of the sensor which is between 25 and 70 s from Fig. 1.8(a). The response time of the strain/pressure sensor and signal-to-noise (SNR) ratios are very important parameters in obtaining accurate information from the pressure sensors in a commercial setting. Both need to be high for a more accurate detection and calculation of pressure. The common limitation of pressure sensors is the less SNR which essentially prevents them from measuring small pressure changes [174-176]. In general, piezoresistive sensors often suffer from poor signal-to-noise ratios, limiting their use for measuring small pressure differentials. Our sensor, based on PDMS, P(VDF-TrFE), and graphene, exhibits a high SNR of 26.4 dB with a

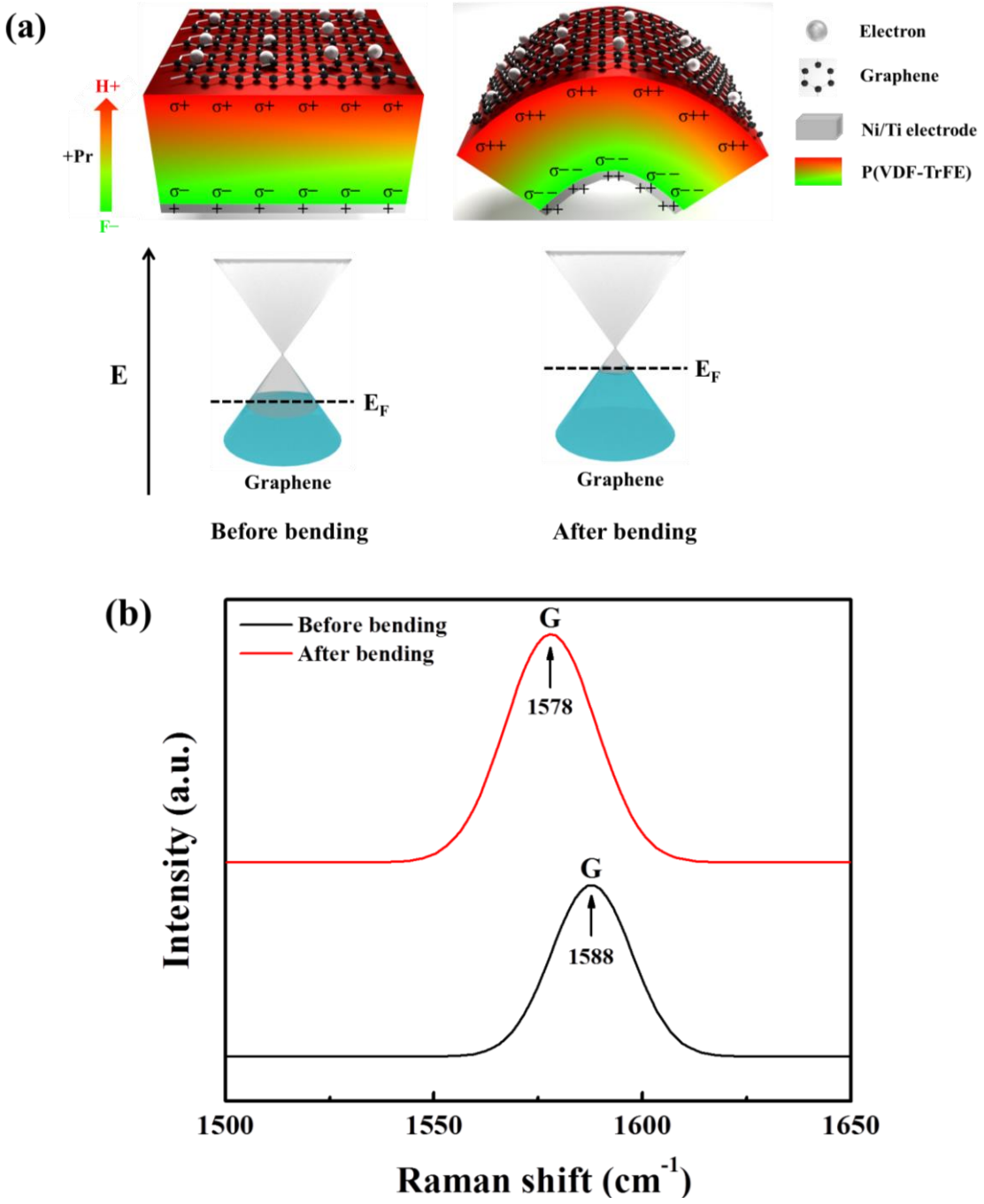

Figure 4.1.9 (a) An illustration for proposed mechanism of the carrier doping in graphene/P(VDF-TrFE) for before and after bending. (b) Raman spectra of graphene for G peak position before and after bending graphene/P(VDF-TrFE).

fast response time (~100 ms). These results make the sensor very attractive for use in wearable electronics such as biomedical applications and smart monitoring systems to monitor strain and pressure in real-time.

Flexible and self-powered strain/pressure sensor in practical wearable application was demonstrated by monitoring the motions of a human hand as shown in Fig. 4.1.11(a). The sensor was physically attached to the hand and activities involving hand motion were performed. The thickness of PDMS for the sensor was increased (up to 1.5 mm) to prevent severe cracking of the bottom electrode on the PDMS substrate under the influence of high pressure. Figure 4.1.11(a) shows the response corresponding to the movement of the hand. The graph shows the amplitude and relaxation time for the bending, deformation and straightening, respectively. The physical motion of the hand is clearly evident in the response graph. In addition, we have demonstrated an application of the self-powered strain/pressure sensor in human activity monitoring by attaching the sensor to a human knee. Multiple activities, involving physical human motion, were performed and the corresponding response of the sensor was obtained on the data cloud in the form of a graphical representation as shown in Fig. 4.1.11(b). This sensor could function as a wearable human activity monitor and recorded multiple motions ranging from simple standing to walking and running. The variation in motion corresponding to different activities was captured well in the sensor response. The peaks in the real-time graphs that occur with multiple motions that clearly demonstrate the efficiency of our sensor in identifying human activities, making it a candidate for a wearable activity tracking device. One application of this self-powered strain/pressure sensor is active

sports monitoring. Statistics like steps taken and energy expenditure could be recorded from the sensor being placed on anatomical regions that are most active during physical movement, such as joints. Because of the thin profile and flexibility of the sensor it could replace other monitoring systems and be implemented neatly into active wear, like knee braces to acquire data without being a hazard during athletics.

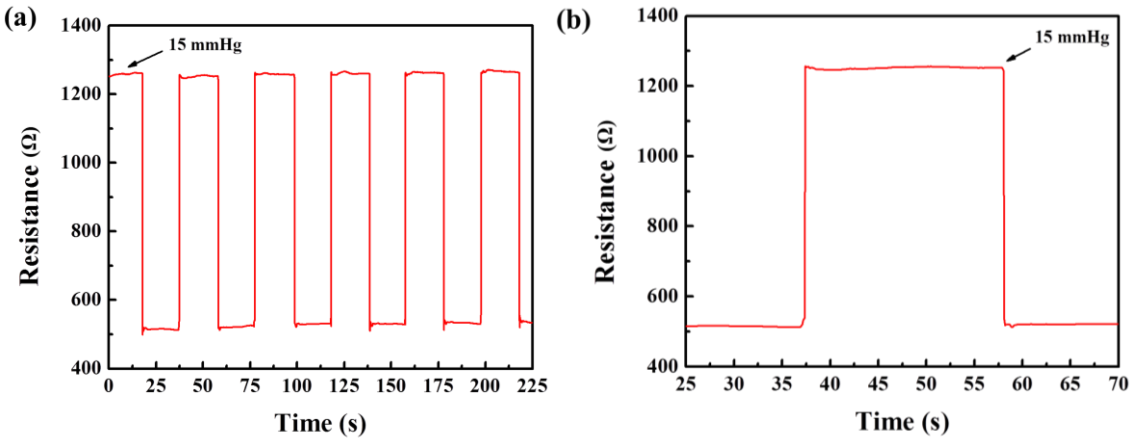

Figure 4.1.10 (a) Response (pressure on) and relaxation (pressure off) times of the sensor between 0 and 15 mmHg pressure. (b) A single pulse of response and relaxation times of the sensor between 25 and 70 s in the Fig. 4.1.10(a).

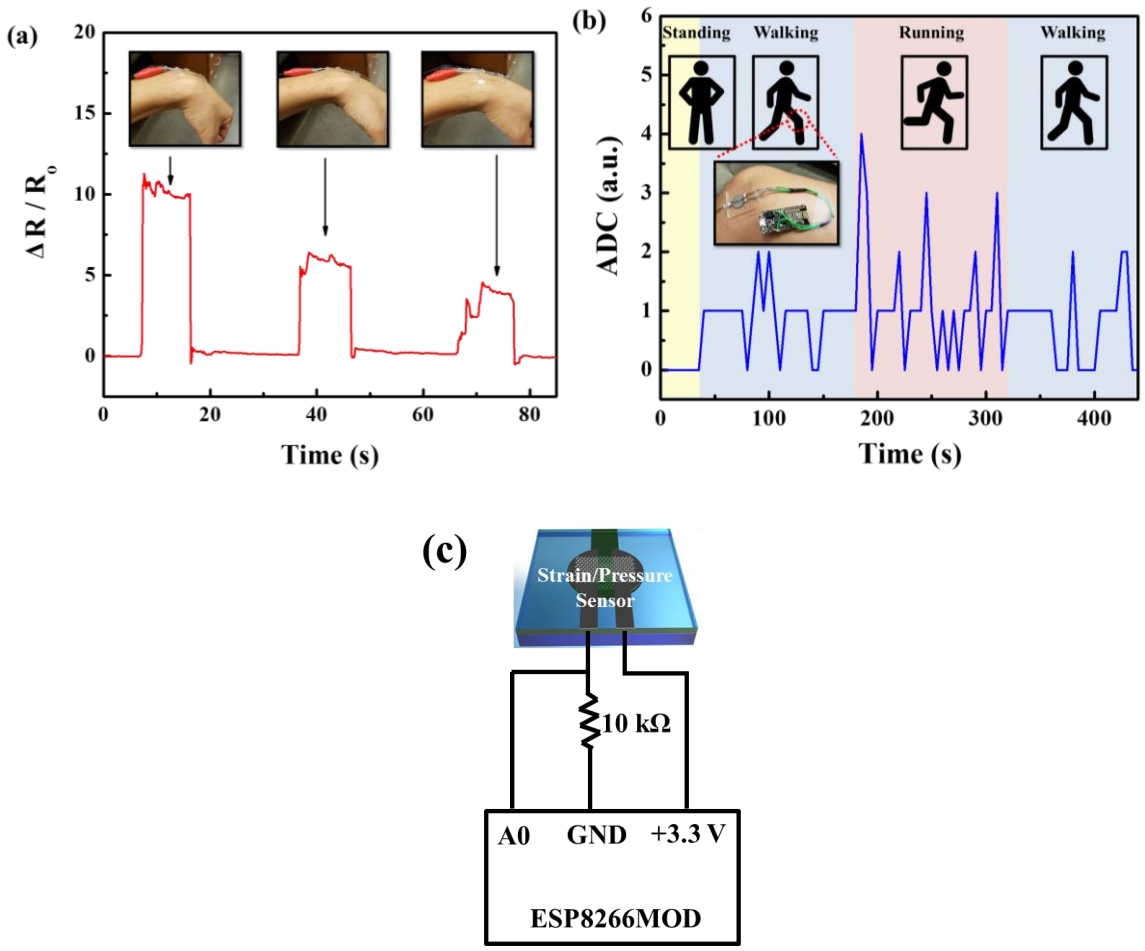

Figure 4.1.11 (a) Demonstration of human hand movement by the self-powered strain/pressure sensor. (b) Output response of the self-powered stain/pressure sensor in terms of analog to digital converted (ADC) values transmitted wirelessly via the ESP8266 Wi-Fi module. The response is updated every 5 seconds on the cloud. (c) Electronic circuit for connecting the sample terminals to the ESP8266 Wi-Fi module.

4.1.4 Conclusions

We have developed a highly sensitive strain/pressure sensor based on the P(VDF-TrFE) film and monolayer graphene on a plain PDMS substrate using a simple

fabrication process. The response of the sensor were quite linear with various pressures and it demonstrated high sensitivity response (average = 0.76 kPa^{-1}, maximum = 0.89 kPa^{-1}, and gauge factor = 481.6) in the entire range of pressure up to 45 mmHg. In addition, the sensor has low detectable strain of 0.016%, SNR of 26.4 dB, and a fast response time of ~100 ms. This was because the piezoresistive response was effectively caused by the hybrid structure of P(VDF-TrFE) film, monolayer graphene, and metal electrode on PDMS substrate. Hence, our self-powered strain/pressure sensor include features of high sensitivity, low detectable strain, simple and ease of fabrication and biocompatibility, making it immensely promising for wearable electronics such as biomedical applications and smart monitoring systems.

4.2 PET substrate based sensor

We have developed a graphene/P(VDF-TrFE) heterojunction based self-powered strain/pressure sensor on polyethylene terephthalate (PET) substrate. The sensor is responsive to variable pressures from 1 kPa to 100 kPa, which result in the strain-induced change of the resistance due to the piezoresistive graphene/P(VDF-TrFE) heterojunction. The range of detectable strain for the sensor was from 0.0075 (1 kPa) to 7.5 % (100 kPa), and the average sensitivity and gauge factor of the sensor were 0.00123/kPa and 16.4, respectively. We also successfully demonstrated the flexible self-powered strain/pressure sensor in a practical wearable application by monitoring the motions of a human hand. The mechanism of the sensor is discussed and illustrated in terms of piezoresistive graphene/P(VDF-TrFE) heterojunction converted from piezoelectric property of P(VDF-TrFE).

4.2.1 Introduction

In recent years, flexible pressure sensors have drawn enormous attention due to their potential applications in smart monitoring systems [125.126], wearable bio-medical health care [121,122], and real-time gait analysis [123,124]. Several different types of pressure sensors such as capacitance [143,144], piezoelectricity [128,132], and piezoresistivity [133,134] have been investigated over the past decade. Among them, piezoresistive based pressure sensors are more suitable for implantable or wearable bio-medical devices owing to its advantages, i.e. step measurement and self-powered operation, including low cost, easy fabrication, simple structure, long-term stability, and

fast response/relaxation time. Typically, piezoresistive based pressure sensors detect the change in resistance caused by the pressure-induced deformation of the active materials such as patterned nano-/micro-structures [143,144], metal films [153], nanowires [127,128], CNTs [137,138], graphene [177,178], and polymers [135,136]. To date, patterned nano-/micro-structures with/without nanowires, CNT, graphene, and polymers as active materials on flexible substrates have been developed for many applications including wearable electronics and artificial electronic skins. However, patterned structures on flexible substrates were fabricated by chemical etching, plasma treatment, and photolithography process which are complicated and add more cost. In addition, the piezoresistive based pressure sensors have limited measurement range, and adhesion between metal films or nanowires and flexible substrate is not durable for long-term operation under bending and vibration conditions. To solve above issues, therefore, new structure of sensor without any complex patterning, i.e. heterojunction, and additional fabrication technique for good adhesion, i.e. annealing, are needed.

Poly(vinylidenefluoride-co-trifluoroethylene), P(VDF-TrFE), have been used as flexible piezoelectric materials recently for pressure sensors due to their high piezoelectric coefficient, flexibility, sensitivity, dielectric strength, mechanical durability, and bio-compatibility. Moreover, P(VDF-TrFE), which can be enhanced the electric charges on surface when tensile strain is increased, offering electrostatic doping to adjacent conductive materials that make it suitable for heterojunction structure with graphene layer. The graphene has high mobility of carriers, mechanical strength flexibility, and tunable Fermi level based on surface charge. Hence, graphene/

heterojunction can give rise to piezoresistive sensors instead of piezoelectric ones.

Herein, we report on the new structure of piezoresistive sensor using graphene/P(VDF-TrFE) heterojunction for self-powered strain/pressure sensor on polyethylene terephthalate (PET) substrate without any complex patterning. We also have utilized optical microscope (Micromanipulator Corp. MODEL No. 6000), X-ray diffraction (XRD), Fourier transform infrared (FTIR) spectroscopy (Thermo Scientific Nicolet380), Raman spectroscopy (CrystaLaser CL-2000), and Hall-effect measurement (Ecopia HMS3000) to investigate the properties of the graphene and the β-phase of P(VDF-TrFE). A COMSOL simulation was performed to theoretically examine the change in strain from the sensor with different pressures. Several pressures are applied and the changes in resistance are measured. The range of detectable strain for the sensor was from 0.0075 (1 kPa) to 7.5 % (100 kPa), and the average sensitivity and gauge factor of the sensor were 0.00123/kPa and 16.4, respectively. We successfully demonstrated the flexible self-powered strain/pressure sensor in a practical wearable application by monitoring the motions of a human hand.

4.2.2 Experimental details

To fabricate the sensor, bottom electrode (radius = 0.8 cm), Ti/Ni (30 nm/150 nm) was deposited by electron beam evaporation on PET substrate (100 μm) (Fig. 4.2.1(a)). The solution of P(VDF-TrFE) was prepared by dissolving Co-polymer powder of P(VDF-TrFE) (50/50, Piezotech) in *N*,*N*-dimethylformamide (DMF) solvent and stirring for 12 h at 40 ℃ to synthesize 13 wt % of P(VDF-TrFE) solution. The solution of

P(VDF-TrFE) was spin-coated on the Ni/Ti/PET at 2500 rpm for 60 s to obtain a thickness of 2 µm and was dried at 60 ^{o}C for 10 min to remove DMF solvent. Then, the film was subsequently post-heated in air at 140 ^{o}C for 2 h to develop β-phase of P(VDF-TrFE) and cooled down to room temperature naturally (Fig. 4.2.1(b)). Another layer of top electrodes (semicircle, radius = 0.3 cm), Ti/Ni (30 nm/150 nm), was deposited by electron beam evaporation on P(VDF-TrFE)/Ni/Ti/PET (Fig. 4.2.1(c)). After that, poling of the P(VDF-TrFE) was performed by subjecting it to an electric field of 100 MV/m for 1 hour. This helps in the uniform alignment of the dipoles in the film making it more piezoresistive. In the next step, monolayer graphene (1.5 cm × 1 cm), grown by the CVD technique on a Cu substrate, is transferred onto Ni/Ti/P(VDF-TrFE)/Ni/Ti/PET using wet transfer method (Fig. 4.2.1(d)). To grow the monolayer graphene, copper foil was placed in a thermal CVD chamber after copper oxides were removed. Then, the system was evacuated (base pressure was 500 mTorr), and 800 standard cubic centimeter per minute (sccm) of Ar was flown at 250 ^{o}C to bake out. H_2 (100 sccm) was then flown for 2 h at 1000 ^{o}C to anneal the copper foil and enlarge the grain size which in turn increases crystalline property. The actual graphene growth was done at an elevated temperature (1035 ^{o}C) by flowing the precursor gas CH_4 (100 sccm) for 20 min. The chamber was cooled down for 50 min after the growth was completed. To measure the performance of the sensor, the sensor was attached on printed circuit board (PCB) designed in EAGLE software and we have utilized data acquisition (Agilent 34970A) which was connected with a computer for processing. Moreover, wire bonders (KS 4524A) was used to connect with gold wire between the sensor and PCB.

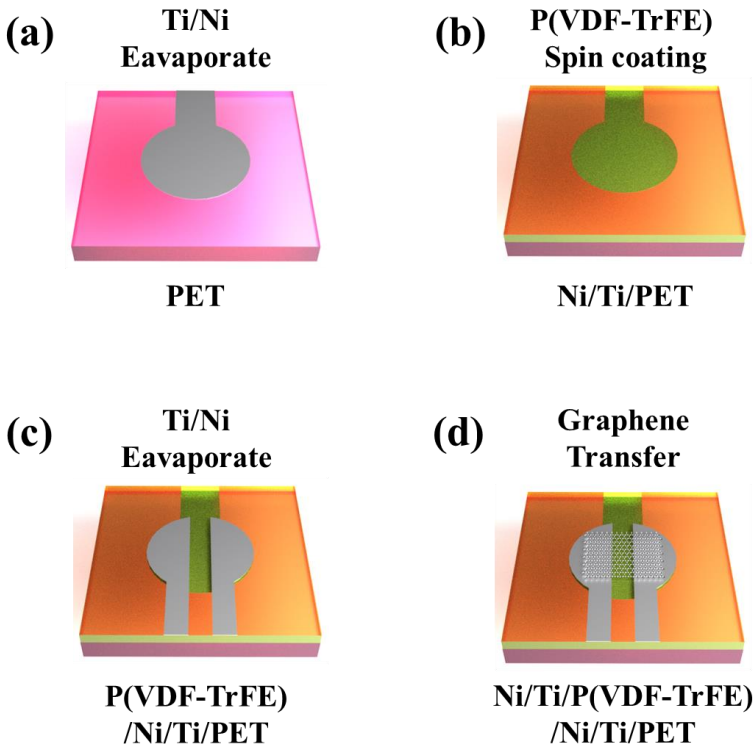

Figure 4.2.1 Schematic demonstration of the processes in fabrication of the sensor. (a) Deposition of Ti/Ni as bottom electrode using electron beam evaporator on PET substrate. (b) P(VDF-TrFE) was spin-coated on Ni/Ti/PET. (c) Deposition of Ti/Ni as top electrode using electron beam evaporator. (d) Transferring graphene on Ni/Ti/P(VDF-TrFE)/Ni/Ti/PET.

4.2.3 Results and discussion

We have developed the graphene/P(VDF-TrFE) heterojunction based flexible self-powered strain/pressure sensor on PET substrate with simple fabrication process. Previously, Sun et. al. [139] and Bae et. al. [180] fabricated pressure sensor on PET using a coplanar-gate graphene transistor and hierarchically structured graphene/PDMS,

respectively, including several photolithography patterned. As mentioned above, photolithography process yield more cost and increase the complexity of fabrication to obtain nano-/micro patterned structures. A schematic illustration of our sensor, which is much simpler in fabrication, is shown in Fig. 4.2.2(a). A layer of PET (100 µm) supports self-powered strain/pressure sensor as flexible substrate, and four different layers such as the Ti/Ni (bottom and top electrodes), the P(VDF-TrFE) film, and the graphene are attached well on the substrate as shown in Fig. 4.2.2(b) and (c).

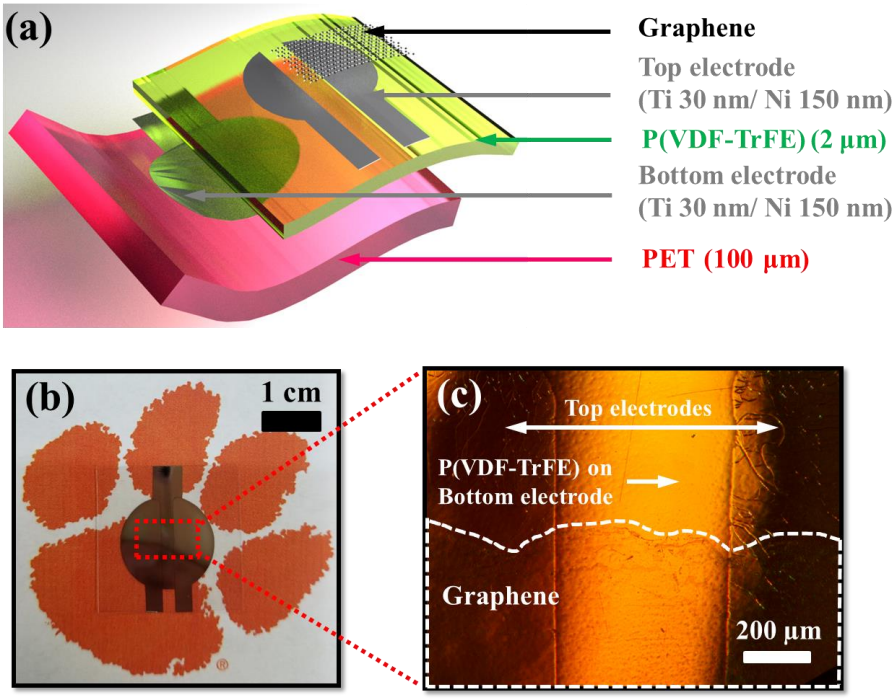

Figure 4.2.2 (a) show schematic illustrations of the design, (b) photographic images, and (c) optical microscopy image for the sensor.

To confirm high quality of crystallinity for the β-phases of P(VDF-TrFE) film, we performed structural characterization using the XRD and FTIR technique on the

prepared P(VDF-TrFE) film. Figure 4.2.3(a) shows the XRD pattern of P(VDF-TrFE) film. The diffraction peak of 2θ value of 19.7^{o} represents orientation planes (110) and (200) for the polar β-phase [81,103]. In addition, three different peaks of FTIR spectroscopy spectrum such as 840, 1290, and 1400 cm-1 indicate β-phases of P(VDF-TrFE) film as shown in Fig. 4.2.3(b) [33,104].

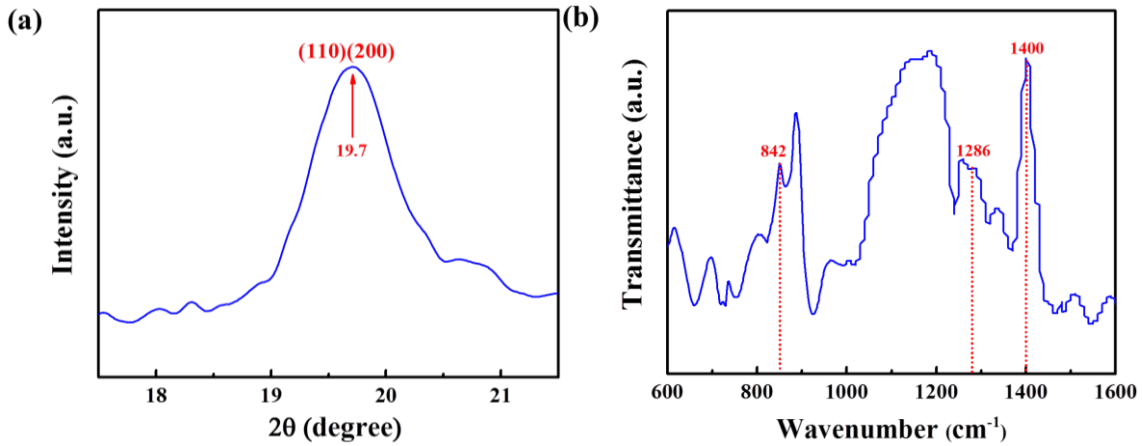

Figure 4.2.3 (a) XRD and (b) FTIR result of β-phase of P(VDF-TrFE) film.

Figure 4.2.4 shows the relative change in resistance with applied various pressures and simulated average strain for the sensor. The inset shows a photographic image after attaching the sensor on the printed circuit board (PCB) designed in EAGLE software. To connect with gold wire between the sensor and PCB, a wire bonders (KS 4524A) was used. The sensor mounted on PCB was placed on vacuum chuck whose were connected to a rotary pump. The variable pressures were transmitted to the sensor by the rotary pump, and the corresponding changes in resistance were recorded by data acquisition (Agilent 34970A) which was connected with a computer for processing. A commercial pressure gauge (Yash Flowmeters YG309) was used in order to monitor the

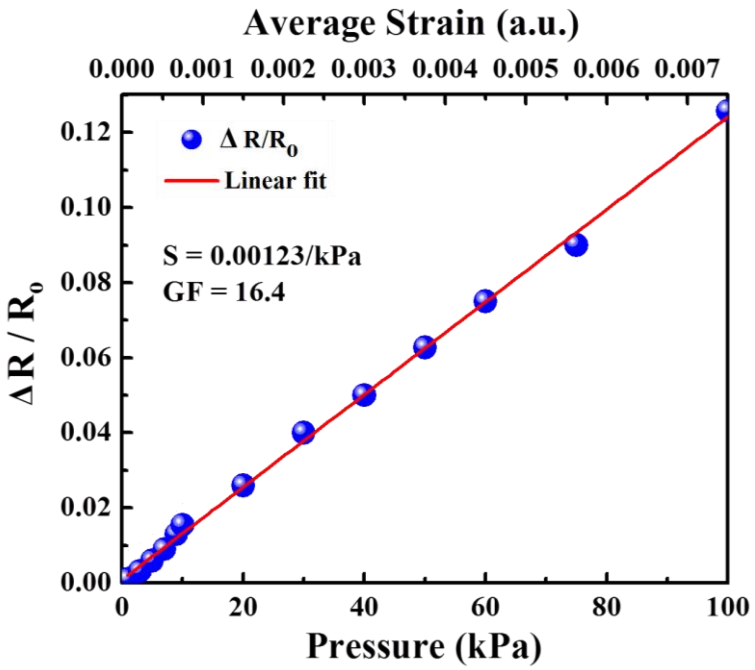

Figure 4.2.4 Relative change in resistance with applied various pressures and simulated average strain for the sensor. The inset shows image of the sensor mounted on the PCB.

real pressure in the sensor during the test. The active area of the sensing was 78.5 mm^2 (radius = 5 mm), and the sensitivity (S) and gauge factor (GF) for the sensor are calculated using the following equations, respectively: $S = (\Delta R/R_o)/\Delta P$, $GF = (\Delta R/R_o)/\varepsilon_{av}$, where ΔR is the relative change in resistance, R_o is the original resistance, ΔP is the change in applied pressure, and εav is average strain on the sensor. It is clear that the response of the sensor (i.e. $\Delta R/R_o$) is reasonably linear, and the value of sensitivity and gauge factor is 0.00123/kPa and 16.4, respectively, over the entire range of pressure up to 100 kPa. The value of GF for our sensor has more than eight times higher GF than the conventional strain gauges based on metal alloys of ~2. In addition, the range of detectable strain for the sensor was from 0.0075 (1 kPa) to 7.5 % (100 kPa). The module

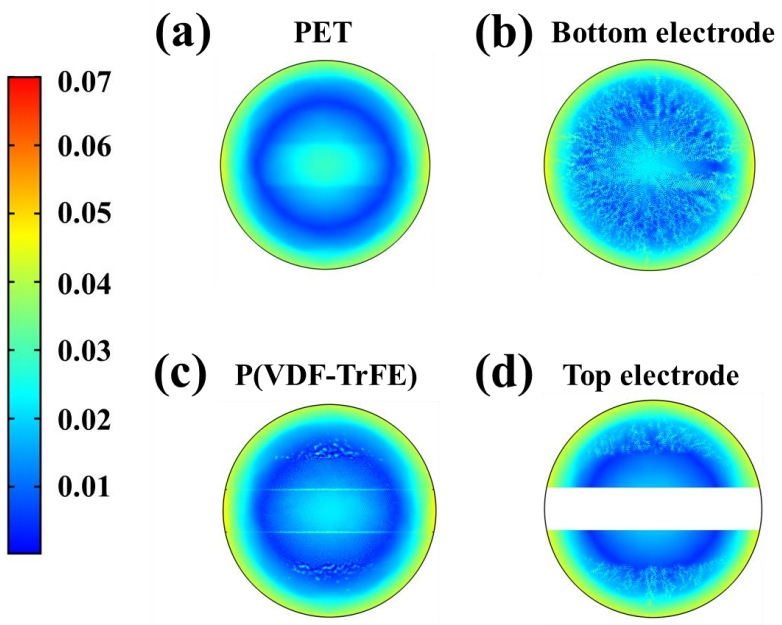

Figure 4.2.5 COMSOL simulation of strain distribution on the active area (diameter = 10 mm) on each layers such as (a) PET substrate, (b) bottom electrode, (c) P(VDF-TrFE) film, and (d) top electrode.

of solid mechanics was used to simulate the average strain of the sensor using the COMSOL finite-element simulation as shown in Fig. 4.2.5. The active area is 10 mm (diameter), the outer rim of the active area was perfectly fixed, and 100 kPa of boundary load was applied onto the bottom surface of the sensor. The Figure 4.2.5(a) to (d) describe each different layers of the sensor such as PET substrate, bottom electrode, P(VDF-TrFE), and top electrode, respectively. Most of the average strain is contributed by PET layer due to its largest thickness comparing to other layers, and the average strain across the sensor was quite linear with various pressures.

Figure 4.2.6(a) shows the response (pressure on) and relaxation times (pressure

off) of the sensor corresponding to the loading (100 kPa) and unloading. The pressure was kept at 100 kPa for 40 s and then reduced back to 0 for 20 s. It is notable that the performance of the sensor is reasonably consistent over the various cycles. Additionally, the sensor, based on graphene/P(VDF-TrFE) heterojunction, exhibits a high SNR of 29.5 dB with a fast response time (~100 ms). Furthermore, we demonstrated the flexible self-powered strain/pressure sensor in a practical wearable application by monitoring the motions of a human hand as shown in Fig. 4.2.6(b). The sensor was physically attached on the hand to monitor activities, and the motion of the hand is clearly evident in the response signal. The resistance was immediately increased with bending, and it reduced back its original value when straightened. It is notable that the demonstration of our sensor involves human activities, making it a potential candidate for a wearable activity tracking devices such as smart monitoring systems, wearable bio-medical health care, and real-time gait analysis.

Graphene, with high carrier mobility, mechanical strength flexibility, and tunable Fermi level based on surface charge, made our sensor a candidate for flexible self-powered strain/pressure sensor using graphene/P(VDF-TrFE) heterojunction. Interestingly, we found that increased in tensile strain at the top surface of the P(VDF-TrFE) film enhances the positive fixed charge density which results in attracting more negative charges in graphene. G-peak of graphene on the sensor in Raman spectra (see Figure 4.2.7(a)) was red-shifted after bending which indicates upward shift of Fermi level and increased electron concentration for graphene. Figure 4.2.7(b) shows an illustration for proposed mechanism of the electrostatic doping in graphene/P(VDF- TrFE)

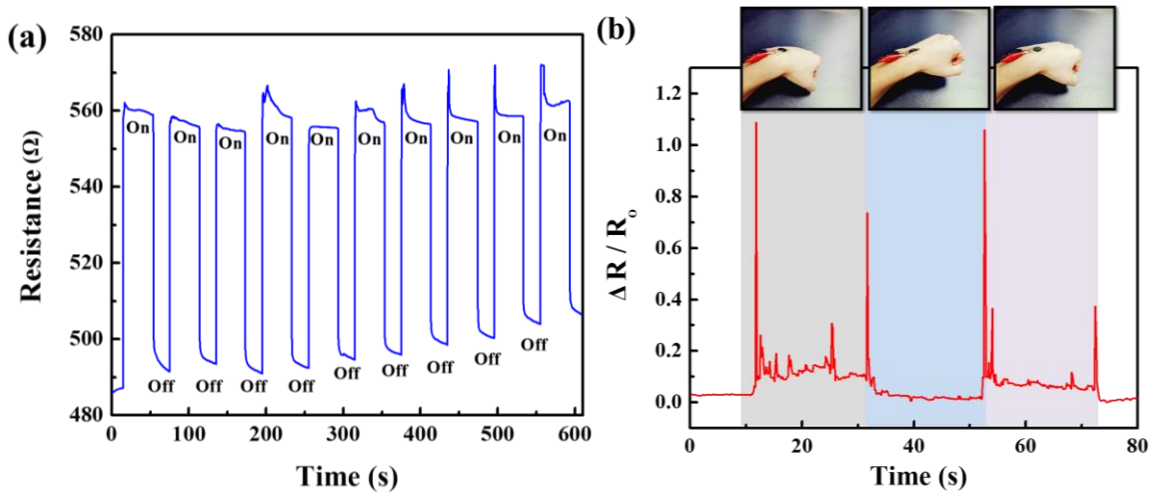

Figure 4.2.6 (a) Response (pressure on) and relaxation (pressure off) times of the sensor between 0 and 100 kPa pressure. (b) Demonstration of human hand movement by the self-powered strain/pressure sensor.

heterojunction for before and after bending. The P(VDF-TrFE) film was positively polarized, and σ+ repels holes and attracts electrons at the top surface while σ- induces positive charge at the bottom, making hole concentration decrease in graphene due to electrostatic doping. Therefore, the proposed sensor mechanism in our sensor is that a decrease in hole density (i.e. increase in electron density) contributes to increase in graphene resistance, which results in change of resistance by piezoresistive properties of graphene/P(VDF-TrFE) heterojunction converted from piezoelectric property of P(VDF-TrFE) film. Finally, the decreased hole density (i.e. increased electron density) by pressure is maintained in the graphene which enables step response of sensor resistance as shown in Fig. 4.2.6(a).

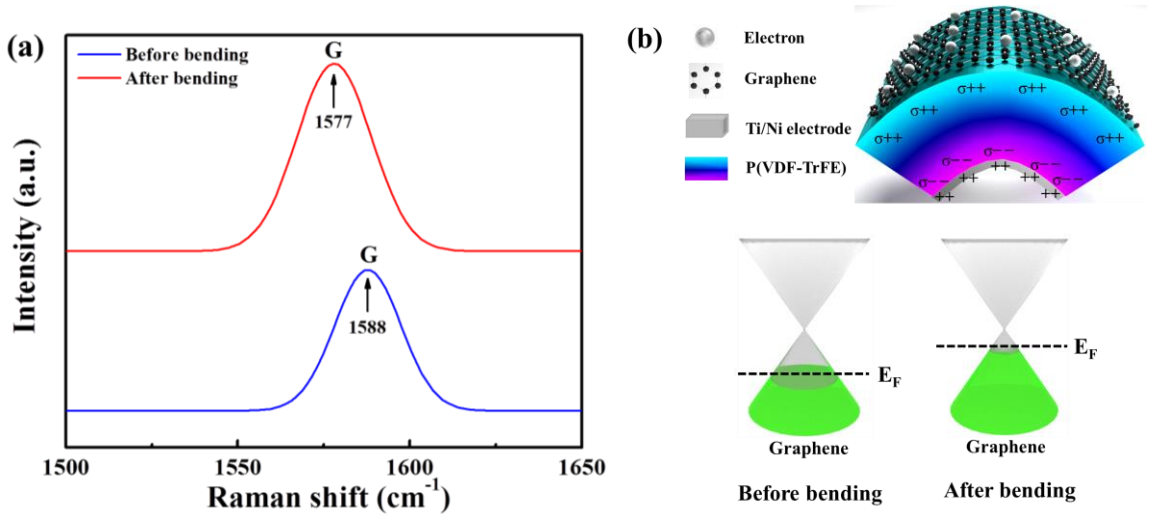

Figure 4.2.7 (a) Raman spectra of graphene for G peak position before and after bending graphene/P(VDF-TrFE). (b) An illustration for proposed mechanism of the carrier doping in the graphene/P(VDF-TrFE) for before and after bending.

4.2.4 Conclusions

In summary, we have developed a graphene/P(VDF-TrFE) heterojunction based strain/pressure sensor on polyethylene terephthalate (PET) substrate utilizing a simple fabrication process. This new structure of self-powered piezoresistive sensor has flexibility, mechanically durability, and bio-compatibility. The mechanism of the sensor is attributed to the piezoresistive property of the graphene/P(VDF-TrFE) heterojunction converted from piezoelectric property of P(VDF-TrFE) film that resulted in changed resistance in graphene which enables step response. The response of the sensor was reasonably linear with various pressures, and demonstrated a sensitivity of 0.00123/kPa and gauge factor of 16.4, over a pressure range of 0 to 100 kPa. The range of detectable

strain for the sensor was from 0.0075 (1 kPa) to 7.5 % (100 kPa), and the sensor has a high SNR of 29.5 dB and a fast response time of ~100 ms.

CHAPTER FIVE

CONCLUSIONS AND FUTURE DIRECTIONS

5.1 Summary

In this dissertation, we have explored the synthesis of graphene and P(VDF-TrFE), their properties and applications in chapter 1 and 2. The graphene, with its outstanding material properties, including high carrier mobility, atomically thin nature, and ability to tolerate mechanical deformation related strain up to 20% before breaking, make it very attractive for developing highly sensitive and conformable strain/pressure sensor. P(VDF-TrFE) have been investigated recently due to their high piezoelectric coefficient, flexibility, sensitivity, mechanical durability, and bio-compatibility for energy harvesting applications as piezoelectric materials. In addition, P(VDF-TrFE) is able to form a heterojunction with graphene, which will strongly affect the carrier density in graphene, due to the fixed charge developing on its surface under strain or pressure. Taking advantages of two different materials, the graphene/P(VDF-TrFE) heterojunction could be used for piezoresistive based strain/pressure sensors which piezoresistive property on graphene was converted from piezoelectric property of P(VDF-TrFE) film, and the their proposed mechanism was discussed with Raman spectroscopy. The sensor was fabricated on two different substrates such as PDMS and PET. The PDMS based sensor demonstrated high sensitivity (average = 0.76 kPa^{-1}, maximum = 0.89 kPa^{-1}, and gauge factor = 481.6) in the low pressure range (~6 kPa), while PET based sensor demonstrated the sensitivity of 0.00123 kPa^{-1} and gauge factor of 16.4 over the pressure range of 0 to 100 kPa. Hence, these features, coupled with the flexible nature of the

device and ease of fabrication, make it a very attractive candidate for use in the growing wearable technology market, especially biomedical applications and smart health monitoring system as well as virtual reality sensors.

For energy harvester, P(VDF-TrFE) was spin-coated on PDMS substrate and its performance such as power density, average voltage and current were 6.62 mW/cm^3, 5.8 V, and 3.2 μA, respectively at 30 Hz vibration frequency at 1.75 g acceleration. Using a full wave bridge rectifier, a capacitor was charged and could deliver 370 nW, which was capable of lighting set of LEDs simultaneously. With this performance, the energy harvester can provide sufficient power to operate structural health monitoring devices, such as a 100 nW temperature sensor, or a low-power 80 nW microprocessor. In spite of the simple design, the performance of the device was found to be superior compared to other flexible energy harvesters on PDMS substrate. However, there was a challenge (i.e., metal contact issue for long term usage) on the PDMS based energy harvester due to the cleaved surface of PDMS substrate under the strain or pressure. To solve this issue, we used PET substrate which has very high mechanical durability under the strain and pressure condition while it generated ~2 V with various stimuli such as wind and tapping. Furthermore, PET based energy harvester was integrated with G-HIP based triboelectric energy harvester for hybrid structure because P(VDF-TrFE) piezoelectric energy harvester has friction inevitably when the active layer is bent and recovered to generate power. Triboelectric based energy harvester generated the voltage of ~5 V while the generated voltage of piezoelectric part was ~2 V. This type of device can be used in shoes soles for wearable electronics as well as flags in renewable technology after adding

multiple devices on flagpole, in order to generate a certain voltage and support electric loads, or monitor steps as gait analysis.

5.2 Future directions

For the future work it would be useful to further develop miniaturized multifunctional sensing systems utilizing strain/pressure sensor, chemical sensor, infrared sensor, and actuators with integrated energy harvesting and communication systems on the same substrate. Graphene and P(VDF-TrFE) materials with their unique properties, make them a very strong candidate for these systems, i.e., smart health monitoring and drug release, as wearable and bio-implantable devices. The graphene/P(VDF-TrFE) heterojunction based multifunctional sensor detect strain/pressure, chemical, and infrared while the piezoelectric and pyroelectric properties part generate a certain power to operate sensors and transmit the data to laptop or mobile in order to analyze it. In addition, it is a very attractive candidate for use in the growing wearable technology market, especially a wearable activity tracking device or virtual reality sensors. This sensor could function as a wearable human activity monitor and recorded multiple motions ranging from simple standing to walking and running. The variation in motion corresponding to different activities is captured well in the sensor response. Statistics like steps taken and energy expenditure can be recorded from the sensor being placed on anatomical regions that are most active during physical movement, such as joints. Because of the thin profile and flexibility of the sensor it could replace other monitoring

systems and be implemented neatly into active wear, like knee braces to acquire data without being a hazard during athletics.

REFERENCES

[1] Kim, S.K., Zhao, Y., Jang, H., Lee, S.Y., Kim, J.M., Kim, K.S., Ahn, J.-H., Kim, P., Choi, J.-Y., Hong, B. H. (2009) Large-scale pattern growth of graphene films for stretchable transparent electrodes, *Nature, 457(5),* 706-710.

[2] Georgiou, T., Jalil, R. Belle, B.D., Britnell, L., Gorbachev, R.V. Morozov, S.V., Kim, Y.-J., Gholinia, A., Haigh, S.J., Makaraovsky, O., Evaes, L., Ponomarenko, L.A., Geim, A.K., Novoselove, K.S., Mishchenko, A. (2012) Vertical field-effect ransistor based on graphene-WS_2 heterostructures for flexible and transparent electronics, *Nature Nanotechnology, 8,* 100-103.

[3] Meric I., Han, M.Y., Young, A.F., Ozyilmaz, B., Kim, P., Shepard, K.L., (2008) Current saturation in zero-bandgap, top-gated graphene field-effect transistors, *Nature Nonothechnology, 3*, 654-659.

[4] Uddin, Md A., Singh, A.K., Sudarshan, T.S., Koley, G. (2014) Functionalized graphene/silicon chemi-diode H_2 sensor with tunable sensitivity, *Nanothecnology, 25*, 125501.

[5] Wu, T., Jenkins, K.A., Valdes-Garcia, A., Farmer, D.B., Zhu, Y., Bol, A.A., Dimitrakopoulos C., Zhu, W., Xia, F., Avouris, P., Lin, Y.-M. (2012) State-of-the-art graphene high-frequency electronics, *Nano Letters, 12*, 3062-3067.

[6] Novoselov, K.S., Geim, A.K., Morozov, S.V., Jiang, D., Zhang, Y., Duonos, S.V., Grigorieva, I.V., Firsov, A.A. (2004) Electric field effect in atomically thin carbon films, *Science, 306,* 666-669.

[7] Banszerus, L., Schmitz, M., Engels, S., Dauber, J., Oellers, M., Haupt, F., Watanabe, K., Taniguchi, T., Beschoten, B., Stampfer, C. (2015) Ultrahigh-mobility graphene devices from chemical vapor deposition on reusable copper, *Sci. Adv. 1,* e1500222.

[8] Levendorf, M.P., Kim, C.-J., Brown, L., Huang, P.Y., Havener, R.W., Muller, D.A., Park, J. (2012) Graphene and boron nitride lateral heterostructures for atomically thin circuitry, *Nature, 488,* 627-632.

[9] Ghosh, S., Calizo, I. Teweldebrhan, D., Pokatilov, E.P., Nika, D.L., Balandin, A.A. Bao, W. Miao, F., Lau, C.N. (2008) Extremely high thermal conductivity of graphene: Prospects for thermal management applications in nanoelectronic circuits, *Appl. Phys. Lett. 92,* 151911.

[10] Nair, R.R., Blake, P., Grigorenko, A.N., Novoselov, K.S., Booth, T.J., Stauber, T., Peres, N.M.R., Geim, A.K. (2008) Fine structure constant defines visual transparency of graphene, Science, 320, 1308.

[11] Pereira, V.M., Neto, A.H.C., Peres, N.M.R. (2009) Tight-binding approach to uniaxial strain in graphene, *Phys. Rev. B 80,* 045401.

[12] Geim, A.K., Novoselov, K.S. (2007) The rise of graphene, *Nature Materials, 6,* 183-191.

[13] Chae, S.J., Gunes, F., Kim, K.K., Kim, E.S., Han, G.H., Kim, S.M., Shin, H.-J., Yoon, S.-M., Choi, J.-Y., Park, M.H., Yang, C.W., Pribat, D., Lee, Y.H. (2009) Syntehsis of large-area graphene layers on poly-nickel substrate by chemical vapor deposition: Wrinkle formation, *Adv. Mater. 21,* 2328-2333.

[14] Bucci, A. (2014) Gearing up for graphene, *New Jersey Business*,

https://njbmagazine.com/monthly-articles/gearing-graphene/

[15] Yazdi, G.R., Iakimov, T., Yakimova, R. (2016) Epitaxial graphene on SiC: A review of growth and characterization, *Crystals, 6,* 53

[16] Kerszberg N., Surtanarayana, P. (2015) Ab initio strain engineering of graphene: opening bandgaps up to 1 eV, *RSC Adv. 5*, 43810.

[17] Wallace, P.R. (1946) The band theory of graphite, Phys. Rev. 71, 622-634.

[18] Chen, J.-H., Jang, C., Xiao, S., Ishigami, M., Fuhrer, M.S. (2008) Intrinsic and extrinsic performance limits of graphene devices on SiO_2, *Nat. Nanotechnol. 3,* 206-209.

[19] Bolotin, K.I., Sikes, K.J., Jiang, Z., Klima, M., Fudenberg, G., Hone, J., Kim, P. Stormer, H.L. (2008) Ultrahigh electron mobility in suspended graphene, Solid. State. *Commun. 146,* 35-355.

[20] Moser, J., Barreiro, A., Bachtold, A. (2007) Current-induced cleaning of graphene, *Appl. Phys. Lett. 91*, 163513.

[21] Bonaccorso, F., Sun, Z., Hasan, T., Ferrari, A.C. (2010) Graphene photonics and optoelectronics, *Nat. Photonics, 4,* 611-622.

[22] Lee, C., Wei, X., Kysar, J.W., Hone, J. (2008) Measurement of the elastic properties and intrinsic strength of monolayer graphene, *Science 321,* 385-388.

[23] Wang, X., Zhi, L., Mullen, K., (2008) Transparent, conductive graphene electrodes for dye-sensitized solar cells, *Nano lett. 8,* 323-327.

[24] Bae, S.-H., Kahya, O., Sharama, B.K., Kwon, J., Cho, H.J., Ozyilmaz, B., Ahn, J.-H. (2013) Graphene-P(VDF-TrFE) multilayer film for flexible applications, *ACS Nano*,

7, 3130-3138.

[25] Yang, T., Jian, X., Zhong, Y., Zhao, X., Lin, S., Li, J., Li, X., Xu, J., Li, Z., Zhu, H. (2017) A wearable and highly sensitive graphene strain sensor for precise home-based pulse wave monitoring, *ACS Sens. 2,* 967-974.

[26] Tian, W., Zhang, X., Chen, Z., Ji, H. (2016) A review of graphene on NEMS, *Recent. Pat. Nanotech. 10,* 3-10.

[27] Li, Na, Chen, Z., Ren, W. Li, F., Cheng, H.-M. (2012) Flexible graphene-based lithium ion batteries with ultrafast charge and discharge rates, *PNAS, 109,* 17360-17365.

[28] Stoller, M.D., Park, S., Zhu, Y., An, J., Ruoff, R.S. (2008) Graphene-based ultracapacitors, *Nano Lett. 8*, 3498-3502.

[29] Shao, Y., Wang, J., Wu, H., Liu, J., Aksay, I.A., Lin, Y. (2010) Graphene based electrochemical sensors and biosensors: A review, *Electroanal. 22,* 1027-1036.

[30] Sun, Z., Liu, Z., Li, J., Tai, G.-A., Lau, S.-P., Yan, F. (2012) Infrared photodetectors based on CVD-grwon graphene and PbS quantum dots with ultrahigh responsivity, *Adv. Mater. 24,* 5878-5883.

[31] Simoes, R.D., Rodriguez-Perez, M.A., Saja, J.A.D., Constantino, C.J.L. (2009) Tailoring the structural properties of PVDF and P(VDF-TrFE) by using natural polymers as additives. *Polym. Eng. Sci. 47*, 2150–2157.

[32] Ducrot, P.-H., Dufour, I., Ayela, C. (2016) Optimization of PVDF-TrFE processing conditions for the fabrication of organic MEMS resonators. *Sci. Rep. 6*, 19426.

[33] Pi, Z., Zhang, J., Wen, C., Zhang, Z.-B., Wu, D. (2014) Flexible piezoelectric

nanogenerator made of poly(vinylidenefluoride-co-trifluorethylene)(PVDF-TrFE) thin film. *Nano Energy, 7*, 33–41.

[34] Lee, J.-H., Ryu, H., Kim, T.-Y., Kwak, S.-S., Yoon, H.-J., Kim, T.-H., Seung, W., Kim, S.-W. (2015) Thermally induced strain-coupled highly stretchable and sensitive pyroelectric nanognerators. *Adv. Energy Mater. 5*, 1500704.

[35] Chen, X., Tian, H., Li, X., Shao, J., Ding, Y., An, N., Zhou, Y. (2015) A high performance P(VDF-TrFE) nanogenerator with self-connected and vertically integrated fibers by patterned EHD pulling. *Nanoscale 7*, 11536–11544.

[36] Gregorio, R., Ueno, E.M. (1999) Effect of crystalline phase, orientation and temperature on the dielectric properties of poly(vinylidene fluoride) (PVDF), *J. Mater. Sci. 34*, 4489-4500.

[37] Xu, H., Shanthi, G., Bharti, V. Zhang, Q.M, Ramotowski, T. (2000) Structural, conformational, and polarization changes of poly(vinylidene fluoride-trifluorethylene) copolymer induced by high-energy electron irradiation, *Macromolecules, 33*, 4152-4131.

[38] Kondrashev, Y.D. (1962) *Trudy Gosudarst. Inst. Priklad. Khim*. *46*, 166.

[39] Gal'perin, Y.L., Strogalin, Y.V., Mlenik, M.P. (1965) *Vysokomol. Soed. 7*, 933.

[40] Lando, J.B., Olf, H.G., Peterlin, A. J. (1966) *Polym. Sci., Part A-1 4*, 941-951.

[41] Hasegawa, R., Takahashi, Y., Chatani, O., Tadokoro, H. (1972) Crystal structures of three crystalline forms of poly(vinylidene fluoride), *Polym. J. 3*, 600-610.

[42] Kawai, H. (1969) The piezoelectricity of poly(vinylidene fluoride) *Jpn. J. Appl. Phys. 8*, 975-976.

[43] Bergman Jr., J.G., McFee, J.H., Crane, G.R. (1971) Pyroelectricity and optical second harmonic generation in polyvinylidene fluoride films, *Appl. Phys. Lett. 18*, 203-205.

[44] Tashiro, K., Tadokoro, H., Kobayashi, M. (1981) Structure and piezoelectricity of poly(vinylidene fluoride), *Ferroelectrics, 32*, 167-175.

[45] Kobayashi, M., Tashiro, K., Tadokoro, H. (1975) Molecular vibrations of three crysal forms of poly(vinylidene fluoride), *Macromolecules, 8*, 158-171.

[46] Bachmann, M.A., Gordon, W.L., Koenig, J.L., Lando, J.B. (1979) An infrared stud of phase-III poly(vinylidene fluoride), *J.Appl. Phys. 50*, 6106-6112.

[47] Lovinger, A.J. (1981) Unit cell of the γ phase of poly(vinylidene fluoride), *Macromolecules*, *14*, 322-325.

[48] Hsu, S.L., Lu, F.J., Waldman, D.A., Muthukumar, M. (1985) Analysis of the crystalline phase transformation of poly(vinylidene fluoride), *Macromolecules 18*, 2583-2587.

[49] Nalwa, H.S. (1995) Ferroelectric Polymers: Chemistry, Physics, and Applications, New York, NY: CRC Press.

[50] Kabir, E., Khatun, M., Nasrin, L., Raihan, M.J., Rahman, M. (2017) Pure β–phase formation in polyvinylidene fluoride (PVDF)-carbon nanotube composites, *J. Phys. D: Appl. Phys. 50*, 163002.

[51] Yagi, T., Tatemoto, M., Sako, J. (1980) Transition behavior and dielectric properties in trifluorioethylene and vinylidene fluoride copolymer, *Polym. J. 12*, 209-223.

[52] Yamada, T., Ueda, T., Kitayama, T. (1981) Piezoelectricity of a high-content lead zirconate titanate/polymer composite, *J. Appl. Phys. 52*, 948-952.

[53] Furukawa, T., Date, M., Fukada, E., Tajitsu, Y., Chiba, A. (1980) Ferroelectric behavior in the copolymer of vinylidenefluoride and trifluoroethylene, *Jpn. J. Appl. Phys. 19*, L109-L112.

[54] Nakamura, K., Nagai, M., Kanamoto, T., Takahashi, Y., Furukawa, T. J. (2001) Development of oriented structure and properties on drawing of poly(vinylidene fluoride) by solid-state coextrusion, *Polym. Sci., Part B: Polym. Phys. 39*, 1371-1380.

[55] Xia, W.M., Gu, Y.J., You, C.Y., Cao, C.J., Xu, Z., Zhang, Z.C. (2015) A crystal phase transition and its effect on the dielectric properties of a hydrogenated P(VDF-co-TrFE) with low TrFE molar content, *RSC Adv., 5*, 107557.

[56] Ueberschlag, P. (2001) PVDF piezoelectric polymer, *Sensor rev. 21*, 118-126.

[57] Yamada, T., Ueda, T., Kitayama, T. (1981) Ferroelectric-to-paraelectric pahse transition of vinylidene fluoride-trifluoroethylene copolymer, *J. Appl. Phys. 52*, 948.

[58] Khan, F.U., Qadir, M.U., (2016) State-of-the-art in vibration-based electrostatic energy harvesting, *J. Micromech. Microeng. 26*, 103001.

[59] Lee, K.Y., Chun, J., Lee, J.-H., Kim, K.N., Kang, N.-R., Kim, J.-Y., Kim, M.H., Shin, K.-S., Gupta, M.K., Baik, J.M., Kim, S.-W. (2014) Hydrophobic sponge structure-based triboelectric nanognerator, *Adv. Mater, 26*, 5037-5042.

[60] Lee, K.Y., Kim, D., Lee, J.-H., Kim, T.Y., Gupta, M.K., Kim, S.-W. (2014) Undirectional high-power generation via stress-induced dipole alignment from $ZnSnO_3$ nanocubes/polymer hybrid piezoelectric nanognerator, *Adv. Funct. Mater, 24*, 37-43.

[61] Venkatasubramanlan, R., Sllvola, E. Colpltts T., O'qulnn, B. (2001) Thin-film

thermoelectric devices with high room-temperature figures of merit, *Nature 413*, 597-602.

[62] Shin, K.-S., Kim, T.Y., Yoon, G.C. Gupta, M.K., Kim, S.K., Seung, W., Kim, H., Kim, S. Kim, S. Kim, S.-W. (2014) Ferroelectric coupling effect on the energy-band structure of hybrid heterojunctions with self-organized P(VDF-TrFE) nanomatrices, *Adv. Mater. 26,* 5619-5625.

[63] Lee, J.-H., Yoon, H.-J. Kim, T.Y., Gupta, M.K., Lee, J.H., Seung, W., Ryu, H., Kim, S.-W. (2015) Micropatterned P(VDF-TrFE) film-based piezoelectric nanogenerators for highly sensitive self-powered pressure sensors, *Adv. Funct. Mater. 25*, 3203-3209.

[64] Lee, J.-H., Ryu, H., Kim, T.-Y., Kwak, S.-S., Yoon, H.-J., Kim, T.-H., Seung, W., Kim, S.-W., (2015) Thermally induced strain-coupled highly stretchable and sensitive pyroelectric nanognerators, *Adv. Energy Mater.* 5, 1500704.

[65] Lee, J.-H., Lee, K.Y., Gupta, M.K., Kim, T.Y., Lee, D.-Y., Oh, J., Ryu, C., Yoo, W.J., Kang, C.-Y., Yoon S.-J., Yoo, J.-B., Kim, S.-W. (2014) Highly stretchable piezoelectric-pyroelectric hybrid nanognereator, *Adv. Mater. 26*, 765-769.

[66] Fusisaki, S., Ishiwara, H., Fujisaki, Y. (2007) Low-voltage operation of ferroelectric poly(vinylidene fluoride-trifluoroethylene) copolymer capacitors and metal-ferroelectric-insulator-semiconductor diodes, *Appl. Phys. Lett. 90*, 162902.

[67] Asadi, K., DeLeeuw, D.M, Boer, B.D., Blom, P.W.M. (2008)Organic non-volatile memories from ferroelectric phase-separated blends, *Nat. Mater. 7,* 547-550.

[68] Chen, X., Li, X. Shao, J., An, N., Tian, H., Wang, C., Han, T., Wang, L., Lu, B. (2017) high-performance piezoelectric nanognerators with imprinted P(VDF-

TrFE)/$BaTiO_3$ nanocomposite micropillars for self-powered flexible sensors, *Small*, *13*, 1604245.

[69] Wu, C.G., Li, P., Cai, G.Q., Luo, W.B., Sun, X.Y., Peng, Q.X., Zhang, W.L. (2014) Quick response PZT/P(VDF-TrFE) composite film pyroelectric infrared sensor with patterned polymide thermal isolation layer, *Infrared Phys. Technol. 66*, 34-38.

[70] Kang, M., Khim, D., Park, W.-T., Kim, J., Kim, J., Noh, Y.-Y., Baeg, K.-J., Kim, D.-Y. (2015) Synergistic high charge-storage capacity for multi-level flexible organic flash memory, *Sci. Rep. 5*, 12299.

[71] Pecora, A., Maiolo, L., Maita, F. Minotti, A. (2012) Flexible PVDF-TrFE pyroelectric sensor driven by polysilicon thin film transistor fabricated on ultra-thin polyimide substrate, *Sensor. Actuat. A-Phys. 185*, 39-43.

[72] Jiang, Y., Gong, L., Hu, X., Zhao, Y., Chen, Y., Chen, H., Feng, L., Zhang, D. (2018) Aligned P(VDF-TrFE) nanofibers for enhanced piezoelectric directional strain sensing, *Polymers, 10*, 364.

[73] Novoselov, K.S., Neto, A.H.C. (2012) Two-dimensional crystals-based heterostructrues: materials with tailored properties, *Phys. Scr. T146*, 014006.

[74] Li, X., Cai, W., An, J., Kim, S., Nah, J., Yang, D., Piner, R., Velamakanni, A., Jung, I., Tutuc, E., Banerjee, S.K., Colombo, L., Ruoff, R.S. (2009) Large-area synthesis of high-quality and uniform graphene films on copper foils, *Science, 5*, 1312-1314.

[75] Deokar, G., Avila, J., Razado-Colambo, I., Codron, J.-L., Boyaval, C., Galopin, E., Asensio, M.-C. Vignaud, D. (2015) Towards high quality CVD graphene growth and transfer, *Carbon, 89*, 82-92.

[76] Reina, A., Jia, X., Ho, J., Nezich, D., Son, H., Bulovic, V., Dresselhaus, M.S., Kong, J. (2009) Large area, few-layer graphene films on arbitrary substrates by chemical vapor deposition, *Nano Lett. 9*, 30-35.

[77] Li, X., Cai, W., Colombo, L., Ruoff, R.S. (2009) Evolution of graphene growth on Ni and Cu by carbon isotope labeling, *Nano Lett. 9*, 4268-4272.

[78] Hossain, Md.M. (2017) Metal oxide semiconductor/graphene heterojunction based sensors, All Theses, 2754. https://tigerprints.clemson.edu/all_theses/2754

[79] Malard, L.M., Pimenta, M.A., Dresselhaus, G., Dresselhaus, M.S. (2009) Raman spectroscopy in graphene, *Physcis Reprots, 473*, 51-87.

[80] Kim, J., Lee, J.H., Ryu, H., Lee, J.-H., Khan, U., Kim, H., Kwak, S.S., Kim, S.-W. (2017) High-performance piezoelectric, pyrorlectric, and triboelectric nanognerator based on P(VDF-TrFE) with controlled crystallinity and dipole alignment, *Adv. Funct. Mater. 27*, 1700702.

[81] Paik, H., Choi, Y.-Y., Hong, S., No, K. (2015) Effect of Ag nanoparticle concentration on the electrical and ferroelectric properties of Ag/P(VDF-TrFE) composite films, *Sci. Rep. 5*, 13209.

[82] Ducrot, P.-H., Dufour, I., Ayela, C. (2016) Optimization of PVDF-TrFE processing conditions for the fabrication of organic MEMS resonators, *Sci. Rep. 6*, 19426.

[83] Vacche, S.D., Oliveira, F., Leterrier, Y., Michaud, V., Damjanovic, D., Manson, J.-A.E. (2012) The effect of processing conditions on the morphology, thermomechanical dielectric, and piezoelectric properties of P(VDF-TrFE)/$BaTiO_3$ composites, *J. Mater. Sci. 47*, 4763-4774.

[84] Vacche, S.D., Leterrier, Y., Michaud, V., Damjanovic, D., Aebersold, A.B., Manson, J.-A.E. (2015) Effect of interfacial interactions on the electromechanical response of poly(vinylidene fluoride-trifluoroethylene)$BaTiO_3$ composties and its time dependence after poling, Compos. *Sci. Technol. 114,* 103-109.

[85] Hwang, G.-T., Park, H., Lee, J.-H., Oh, S., Park, K.-I., Byun, M., Park, H., Ahn, G., Jeong, C.K., No, K. (2014) Self-powered cardiac pacemaker enable by flexible single crystalline PMN-PT piezoelectric energy harvester. *Adv. Mater. 26,* 4880–4887.

[86] Gafforelli, G., Corigliano, A., Xu, R., Kim, S.-G. (2014) Experimental verification of a bridge-shaped, nonlinear vibration energy harvester. *Appl. Phys. Lett. 105*, 203901.

[87] Soares dos Santos, M.P., Ferreira, J.A.F., Simoes, J.A.O., Pascoal, R., Torrao, J., Xue, X., Furlani, E.P. (2016) Magnetic levitation-based electromagnetic energy harvesting: A semi-analytical non-linear model for energy transduction. *Sci. Rep. 6,* 18579.

[88] Tao, K., Wu, J., Tang, L., Hu, L., Lye, S.W., Miao, (2017) J. Enhanced electrostatic vibrational energy harvesting using integrated opposite-charged electrets. *J. Micromech. Microeng. 27,* 044002.

[89] Alluri, N.R., Selvarajan, S., Chandrasekhar, A., Saravanakumar, B., Lee, G.M., Jeong, J.H., Kim, S.-J. (2017) Worm structure piezoelectric energy harvester using ionotropic gelation of barium titanate-clacium alginate composite. *Energy, 118*, 1146–1155.

[90] Khan, F.U., Qadir, M.U. (2016) State-of-the-art in vibration-based electrostatic energy harvesting. *J. Micromech. Microeng. 26,* 103001.

[91] Kim, D.Y., Lee, S., Lin, Z.-H., Choi, K.H., Doo, S.G., Chang, H., Leem, J.-Y., Wang,

Z.L., Kim, S.-O. (2014) High temperature processed ZnO nanorods using flexible and transparent mica substrates for dye-sensitized solar cells and piezoelectric nanogenerators. *Nano Energy, 9,* 101–111.

[92] Chen, C.Y., Huang, J.H., Zhou, Y., Lin, L., Huang, P.C., Liu, C.P., He, J.H., Wang, Z.L. (2011) Anisotropic outputs of a nanogeneator from oblique-aligned ZnO nanowire arrays. *ACS Nano, 5,* 6707–6713.

[93] Lee, K.Y., Kim, D., Lee, J.-H., Kim, T.Y., Gupta, M.J., Kim, S.-W. (2014) Unidirectional high-power generation via stress-induced dipole alignment from ZnSnO3 nanocubes/polymer hybrid piezoelectric nanogenerator. *Adv. Funct. Mater. 24*, 37–43.

[94] Wu, J.M., Xu, C., Zhang, Y., Wang, Z.L. (2012) Lead-free nanogeneator made from single ZnSnO3 microbelt. *ACS Nano 6,* 4335–4340.

[95] Park, K.-I., Son, J.H., Hwang, G.-T., Jeong, C.K., Ryu, J., Koo, M., Choi, I., Lee, S.H., Byun, M., Wang, Z.L. (2014) Highly-efficient, flexible piezoelectric PZT thin film nanogenerator on plastic substrates. *Adv. Mater. 26*, 2514–2520.

[96] Chen, X., Xu, S., Yao, N., Shi, Y. (2010) Nanogenerator for mechanical energy harvesting using PZT nanofibers. *Nano Lett. 10,* 2133–2137.

[97] Wang, X., Yang, B., Liu, J., Zhu, T., Yang, C., He, Q. (2016) A flexible triboelectric-piezoelectric hybrid nanogenrator based on P(VDF-TrFE) nanofibers and PDMS/MWCNT for wearable devices. *Sci. Rep. 6,* 36409.

[98] Han, M., Zhang, X.-S., Meng, B., Liu, W., Tang, W., Sun, X., Wang, W., Zhang, H. (2013) r-shaped hybrid nanogenerator with enhanced piezoelectricity. *ACS Nano 7,*

8554–8560.

[99] Ding, Y., Duan, Y., Huang, Y.A. (2015) Electrohydrohynamically printed, flexible energy harvester using in situ poled piezoelectric nanofibers. *Energy Technol. 3,* 351–358.

[100] Liu, Z., Zhang, S., Jin, Y.M., Ouyang, H., Zou, Y., Wang, X.X., Xie, L.X., Li, Z. (2017) Flexible piezoelectric nanogenerator in wearable self-powered active sensor for respiration and healthcare monitoring. *Semicond. Sci. Technol. 32,* 064004.

[101] Bhavanasi, V., Kumar, V., Parida, K., Wang, J., Lee, P.S. (2016) Enhanced piezoelectric energy harvesting performance of flexible PVDF-TrFE bilayer films with graphene oxide. *ACS Appl. Mater. Interfaces 8,* 521–529.

[102] Kim, S., Towfeeq, I., Bayram, F., Khan, D., Koley, G. (30 October–3 November 2016) Highly flexible P(VDF-TrFE) film-based piezoelectric self-powered energy harvester. *In Proceedings of the IEEE Sensors*, Orlando, FL, USA, pp. 1–3.

[103] Chen, S., Yao, K., Tay, F.E.H., Chew, L.L.S. (2010) Comparative investigation of the structure and properties of ferroelectric poly(vinylidene fluoride) and poly(vinylidene fluoride-trifluoroethylene) thin films crystallized on substrates. *J. Appl. Polym. Sci. 116,* 3331–3337.

[104] Ma, W., Zhang, J., Chen, S., Wang, X. (2008) Crystalline phase formation of poly(vinylidenefluoride) from tetrahydrofuran/N,N-dimethylformamide mixed solutions. *J. Macromol. Sci. B 47,* 434–449.

[105] Ko, Y.H., Nagaraju, G., Lee, S.H., Yu, J.S. (2014) PDMS-based triboelectric and transparent nanogenerators with ZnO nanorod arrays. *ACS Appl. Mater. Interfaces 6,*

6631–6637.

[106] Fan, F.-R., Tian, Z.-Q., Wang, Z.L. (2012) Flexible triboelectric generator! *Nano Energy 1,* 328–334.

[107] Sinha, T.K., Ghosh, S.K., Maiti, R., Jana, S., Adhikari, B., Mandal, D., Ray, S.K. (2016) Graphene-silver-induced self-polarized PVDF-based flexible plasmonic nanogenerator toward the realization for new class of self powered optical sensor. *ACS Appl. Mater. Interfaces 8,* 14986–14993.

[108] Kim, S., Gupta, M.K., Lee, K.Y., Sohn, A., Kim, T.Y., Shin, K.-S., Kim, D., Kim, S.K., Lee, K.H., Shin, H.-J., Transparent flexible graphene triboelectric nanogners. *Adv. Mater. 26,* 3918–3925.

[109] Xiong, J., Lin, M.-F., Wang, J., Gaw, S.L., Parida, K., Lee, P.S. (2017) Wearable all-fabric-based triboelectric generator for water energy harvesting. *Adv. Energy Mater. 1701243*, 1–10.

[110] Moyet, R.P., Stace, J., Amin, A., Finkel, P., Rossetti, G.A. (2015) Non-resonant electromechanical energy harvesting using inter-ferroelectric phase transitions. *Appl. Phys. Lett. 107,* 172901.

[111] Bonisoli, E., Repetto, M., Manca, N., Gasparini, A. (2017) Electromechanical and electronic integrated harvester for shoes application. *IEEE/ASME Trans. Mech. 22*, 1921–1932.

[112] Takhedmit, H., Saddi, Z., Karami, A., Basset, P., Cirio, L. (2017) Electrostatic vibration energy harvester with 2.4-GHz cockcroft-walton rectenna start-up. *C. R. Phys. 18*, 98–106.

[113] Liu, H., Chen, T., Sun, L., Lee, C. (2015) An electromagnetic MEMS energy harvester array with multiple vibration modes. *Micromachines 6,* 984–992.

[114] Roy, S., Podder, P., Mallick, D. (2016) Nonlinear energy harvesting using electromagnetic transduction for wide bandwidth. *IEEE Magn. Lett. 7,* 5701004.

[115] Lee, Y., Blaauw, D., Sylvester, D. (2016) Ultralow power circuit design for wireless sensor nodes for structural health monitoring. *Proc. IEEE 104,* 1529–1546.

[116] Jeong, S., Foo, Z., Lee, Y., Sim, J.-Y., Blaauw, D., Sylvester, D. A fully-integrated 71 nW CMOS temperature sensor for low power wireless sensor nodes. *IEEE J. Solid-State Circuits 49,* 1682–1693.

[117] Lim, W., Lee, I., Sylvester, D., Blaauw, D. (22–26 February 2015) Batteryless sub-nW cortex-MO+ processor with dynamic leakage-suppression logic. *In Proceedings of the 2015 IEEE International Solid-State Circuits Conference*, San Francisco, CA, USA.

[118] Liu, X., Zhu, Y., Nomani, M.W., Wen, X., Hsia, T.Y., Koley, G. (2013) A highly sensitive pressure sensor using a Au-patterned polydimethylsiloxane membrane for biosensing applications. *J. Micromech. Microeng. 23,* 025022.

[119] Koley, G., Liu, J., Nomani, M.W., Yim, M., Wen, X., Hsia, T.Y. (2009) Miniaturized implantable pressure and oxygen sensors based on polydimethylsiloxane thin films. *Mater. Sci. Eng. C 29,* 685–690.

[120] Singh, A., Uddin, M.A., Sudarshan, T., Koley, G. (2014) Tunable reverse-biased graphene/silicon heterojunction schottky diode sensor. *Small 10,* 1555–1565.

[121] Rogers, J. A. (2010) A diverse printed future, *Nature 468,* 177.

[122] Zang, Y., Zhang, F., Di, C.-A., Zhu, D. (2015) Advances of flexible pressure sensors

toward artificial intelligence and health care applications, *Mater. Horiz. 2*, 140.

[123] Deluzio, K. J., Astephen, J. L. (2007) Biomechanical features of gait waveform dta associated with knee osteoarthritis an application of principal component analysis, *Gait Posture, 25,* 86.

[124] Goldie, P. A., Mappsc, Matyas, T. A., Evans, O. M. (1996) *Arch Phys Med Rehabil, 77,* 1074.

[125] Kim, D.-H., Lu, N., Ma, R., Kim, Y.-S., Kim, R-H., Wang, S., Wu, J., Won, S. M., Tao, H., Islam, A., Yu, K. J., Kim, T.-i., Chowdhury, R., Ying, M., Xu, L., Li, M., Chung, H.-J., Keum, H., Mccormick, M., Liu, P., Zhang, Y.-W., Omenetto, F. G., Huang, Y., Coleman, T., Rogers, J. A. (2011) Epidermal electronics, *Science 333*, 838.

[126] Pandian, P. S., Mohanavelu, K., Safeer, K. P., Kotresh, T. M., Shakunthala, D. T., Gopal, P., Padaki, V. C. (2008) Smart vest: Wearable multi-parameter remote physiological monitoring system, *Med. Eng. Phys. 30*, 466.

[127] Rajagopalan, P., Singh, V., Palani, I.A. (2018) Enhancement of ZnO-based flexible nanogenerators via a sol-gel technique for sensing and energy harvesting applications, *Nanotechnology, 29,* 105406.

[128] Wu, W., Wen, X., Wang, Z.L. (2013) Taxel-addressable matrix of vertical-nanowire piezotronic transistors for active and adaptive tactile lamaging, *Science 340*, 952-957.

[129] Park, K.-I., Xu, S., Liu, Y., Hwang, G.-T., Kang, S.-J.L., Wang, Z.L., Lee, K.J. (2010) Piezoelectric $BaTiO_3$ thin film nanogenrator on plastic substrates, *Nano Lett. 10*, 4939-4943.

[130] Alluri, N.R., Selvarajan, S., Chandrasekhar, A., Saravanakumar, B., Jeong, J.H., Kim,

S.-J. (2017) Piezoelectric $BaTiO_3$/alginate spherical composite beads for energy harvesting and self-powered wearable flexion sensor, *Compos. Sci. Technol. 142,* 65-78.

[131] Joshi, A.B., Kalange, A.E., Bodas, D., Gangal, S.A. (2010) Simulations of piezoelectric pressure sensor for radial artery pulse measurement, *Mater. Sci. Eng. B 168,* 250-253.

[132] Persano, L., Dagdeviren, C., Su. Y., Zhang, Y., Girarado, S., Pisignano, D., Huang, Y., Rogers, J.A. (2013) High performance piezoelectric devices based on aligned arrays of nanofibers of poly(vinylidenefluoride-co-trifluoroethylene), *Nat. Comm. 4,* 1633.

[133] Alpuim, P., Correia, V., Marins, E.S., Rocha, J.G., Trindade, I.G., Mendez, S.L. (2011) Piezoresistive silicon thin film sensor array for biomedical applications, *Thin Solid Films, 519,* 4574-4577.

[134] Lim, H.C., Schulkin, B., Pulickal, M.J., Liu, S. Petrova, R., Thomas, G., Wagner, S., Sidhu, K., Federici, J.F. (2005) Flexible membrane pressure sensor, *Sensor. Actuat. A 119,* 332-335.

[135] Lu, M. Lu, C., Yang, S., Rogers, J. (2012) Highly sensitive skin-mountable strain gauges based entirely on elastomers, *Adv. Funct. Mater. 22*, 4044-4050.

[136] Kong, J.-H., Jang, N.-S., Kim, S.-H., Kim, J.-M. (2014) Simple and rapid micropatterning of conductive carbon composites and its application to elastic strain sensors, *Carbon, 77,* 199-207.

[137] Yamada, T., Hayamizu, Y., Yamamoto, Y., Yomogida, Y., Najafabadi, A.I., Futaba, D.N., Hata, K. (2011) A stretchable carbon ananotube strain sensor for human-motion

detection, *Nat. Nanotechnol. 6*, 296-301.

[138] Jian, M., Xia, K., Wang, Q., Yin, Zhe, Wang, H., Wang, C., Xie, H., Zhang, M., Zhang, Y., (2017) Flexible and highly sensitive pressure sensors based on bionic hierarchical structures, *Adv. Funct. Mater. 27*, 1606066.

[139] Sun, Q., Sung, W., Kim, B.J., Seo, S., Kim, S.-W., Cho, J.H. (2015) Active matrix electronic skin strain sensor based on piezopotential-powered graphene transistors, *Adv. Mater. 27*, 3411-3417.

[140] Mannsfeld, S.C.B., Tee, B.C.-K., Stoltenberg, R.M., Chen, C.V.H.-H., Baraman, S., Muir, B.V.O., Sokolov, A.N., Reese, C., Bao, Z. (2010) Highly sensitive flexible pressure sensors with mcrostructured rubber dielectric layers, *Nat. Mater. 9*, 859-864.

[141] Graz, I., Krause, M., Bauer-Gogonea, S., Bauer, S., Lacour, S.P., Ploss, B., Zirkl, M., Stadlober, B., Wagner, S. (2009) Flexible active-matrix cells with selectively poled bifunctional polymer-ceramic nanocomposite for pressure and temperature sensing skin, *J. Appl Phys. 106*, 034503.

[142] Tien, N.T., Jeon, S., Kim, D.-I., Trung, T.Q., Jang, M., Hwang, B.-U., Byun, K.-E., Bae, J., Lee, E., Tok, J.B.-H., Bao, Z., Lee, N.-E., Park, J.-J. (2014) A Flexible bimodal sensor array for simultaneous sensing of pressure and temperature, *Adv. Mater. 26*, 796-804.

[143] Pang, C., Koo, J.H., Nguyen, A., Caves, J.M., Kim, M.-G., Chortos, A., Kim, K., Wang, P.J., Tok, J.B.-H., Bao, Z. (2015) *Adv. Mater. 27*, 634-640.

[144] Park S., Kim, H., Vosguertchian, M., Cheon, S., Kim, H., Koo, J.H., Kim, T.R., Lee, S., Schwartz, G., Chang, H., Bao, Z. (2014) Stretchable energy-harvesting tactile

electronic skin capable of differentiating multiple mechanical stimuli modes, *Adv. Mater. 26*, 7324-7332.

[145] Sun, J.-Y., Keplinger, C., Whitesides, G.M., Suo, Z. (2014) Ionic skin, *Adv. Mater. 26*, 7608-7614.

[146] Pereira, V.M., Neto, A.H.C. (2009) Tight-binding approach to uniaxial strain in graphene *Phys. Rev. B 80,* 045401.

[147] Si, C., Sun, Z., Liu, F. (2016) Strain engineering of graphene: a review, *Nanoscale, 8*, 3207-3217

[148] Joo, Y., Yoon, J., Hong, Y. (2016) Elastomeric nanowire composite for flexible pressure sensors with tunable sensitivity, *Journal of Information Display, 17*, 59-64.

[149] Peng, P., Li, L., Guo, W., Hui, Z., Fu, J., Jin, C., Liu, Y., Zhu, Y. (2018) Room-temeprature joining of silver nanoparticles using potassium chloride solution for flexible electrode application, *J. Phys. Chem. C. 122*, 2704-2711.

[150] Tewari, A., Gandla, S., Bohm, S., McNeill, C.R., Gupta, D. (2018) Highly exfoliated MWNT-rGO ink-wrapped polyurethane foam for piezoresistive pressure sensor application, *ACS Appl. Mater. Interfaces, 10*, 5185-5195.

[151] Lee, C.H., Ma, Y., Jang, K.-I., Banks, A., Pan, T., Feng, X., Kim, J.S., Kang, D., Raj, M.S., McGrane, B.L., Morey, B., Wang, X., Ghaffari, R., Huang, Y., Rogers, J.A., (2015) Soft core/shell packages for stretchable electronics, *Adv. Funct. Mater. 25*, 3698-3704.

[152] Sonar, H.A., Paik, J., (2016) Soft pneumatic actuator skin with piezoelectric sensors for vibrotacile feedback, *Frontiers in Robotics and AI, 2,* 38.

[153] Liu, X., Zhu, Y., Nomani, W., Wen, X., Hsia, T.-Y., Koley, G. (2013) A highly sensitive pressure sensor using a Au-patterned polydimethylsiloxane membrane for biosensing applications, *J. Micromech. Microeng. 23,* 025022.

[154] Ren, K.N., Zheng, Y.Z., Dai, W., Ryan, D., Fung, C.Y., Wu, H.K. (3-7 October, 2010) Soft-lithography-based high temperature molding method to fabricate whole teflon microfluidic chips, 14th Internation Conference on Miniaturized Systems for Chemistry and Life Sciences, Groningen, The Netherlands.

[155] Johnston, I.D., AcCluskey, D.K., Tan, C.K.L., Tracey, M.C. (2014) Mechanical characterization of bulk sylgard 184 for microfluidics and microengineering, *J. Micromech. Microeng. 24,* 035017.

[156] Xu, Lizhi, Gutbrod, S.R., Bonifas, A.P., Su, Y., Sulkin, M.S., Lu, N., Chung, H.-J., Jang, K.-I., Liu, Z., Ying, M., Lu, Chi, Webb, R.C., Kim, J.-S., Laughner, J.I., Cheng, H., Liu, Y., Ameen, A., Jeong, J.-W., Kim, G.-T., Huang, Y., Efimov, I.R., Rogers, J.A. (2014) 3D multifunctional integumentary membranes for spatiotemporal cardiac measurements and stimulation across the entire epicardium, *Nat. Commum. 5,* 3329.

[157] Kim, J., Lee, M., Shim, H.J., Ghaffari, R., Cho, H.R., Son, D., Jung, Y.H., Soh, M., Choi, C., Jung, S., Chu, K., Jeon, D., Lee, S.-T., Kim, J.H., Choi, S.H., Hyeon, T., Kim, D.-H. (2014) Stretchable silicon nanoriboon electronics for skin prosthesis, *Nat. Commun. 5,* 5747.

[158] Singh, A.K., Uddin, M.A., Tolson, J.T., Maire-Afeli, H., Sbrockey, N., Tompa, G.S., Spencer, M.G., Vogt, T., Sudarshan, T.S., Koley, G., (2013) Electrically tunable molecular doping of graphene, *Appl. Phys. Lett. 102,* 043131.

[159] Uddin, Md.A., Singh, A.K., Sudarashan, T.S., Koley, G., (2014) Functionalized graphene/silicon chemi-diode H_2 sensor with tuanble sensitivity, *Nanotechnology, 25*, 125501.

[160] Singh, A., Uddin, Md.A., Sudarashan, T., Koley, G. (2014) Tunable reverse-biased grapehen/silicon heterojunction schottky diode sensor, *Small, 10*, 1555-1565.

[161] Pi, Z., Zhang, J., Wen, C., Zhang, Z.-B., Wu, D. (2014) Flexible piezoelectric nanogenerator made of poly(vinylidenefluoride-co-trifluoroethylene)(PVDF-TrFE) thin film, *Nano Energy, 7*, 33-41.

[162] Simoes, R.D., Perez, M.A.R., Saja, J.A.D., Constantino, C.J.L. (2009) Tailoring the structural properties of PVDF and P(VDF-TrFE) by using natural polymers as additives, *Polym. Eng. Sci.* DOI 10.1002/pen

[163] Kim, S., Towfeeq, I., Dong, Y., Gorman, S., Rao, A.M., Koley, G. (2018) P(VDF-TrFE) film on PDMS substrate for energy harvesting applications, *Appl. Sci. 8*, 213.

[164] Ducrot, P.-H., Dufour, I., Ayela, C. (2016) Optimization of PVDF-TrFE processing conditions for the fabrication of organic MEMS resonators, *Sci. Rep. 6*, 19426.

[165] Vacche, S.D., Oliverira, F., Leterrier, Y., Michaud, V., Damjanovic, D., Manson, J.-A.E. (2012) The effect of processing conditions on the morphology, thermomechanical, dielectric, and piezleectric properties of P(VDF_TrFE)/$BaTiO_2$ composties, *J. Mater. Sci. 47*, 4763-4774.

[166] Vacche, S.D., Leterrier, Y, Michaud, V., Damjanovic, D., Aebersold, A.B., Manson, J.-A.E. (2015) Effect of interfacial interactions on the electromechanical response of poly(vinylidene fluoride-trifluorthylene)$BaTiO_3$ composties and its time dependence

after poling, *Compos. Sci. Technol. 114*, 103-109.

[167] Wen, Y.-H., Yang, G. Y., Bailey, V. J., Lin, G., Tang, W. C., Keyak, J. H. (2005) Mechanically robust micro-fabricated strain gauges for use on bones, *Proc. 3rd Annu. Int. IEEE/EMBS Special Topic Conf. on Microtechnologies in Medicine and Biology (Kahuku, HI)*, 303.

[168] Yang, G. Y., Bailey, V. J., Wen, Y.-H., Lin, G., Tang, W. C., Keyak, J. H. (2004) Fabrication and characterization of microscale sensors for bone surface strain measurement, *Proc. IEEE Sensors, 3*, 1355.

[169] Fesenko, O., Dovbeshko, G., Dementjev, A., Karpicz, R., Kaplas, T., Svirko, Y. (2015) Graphene-enhanced raman spectroscopy of thymine adsorbed on singl-layer graphene, *Nanoscale Res. Lett. 10*, 163.

[170] Wang, H., Wang, Y., Cao, X., Feng, M., Lan, G., J. (2009) Vibrational properties of graphene and graphene layers, *Raman Spectrosc. 40*, 1791.

[171] Lee, J.-H., Lee, K. Y., Kumar, B., Tien, N. T., Lee, N.-E., Kim, S.-W. (2013) Highly sensitive stretchable transparent piezoelectric nanogenerators, *Energy Environ. Sci. 6*, 169.

[172] Lazzeri, M., Mauri, F. (2006) Nonadiabatic kohn anomaly in a doped graphene monolayer, *Phys. Rev. Lett. 97*, 266407.

[173] Pisana, S., Lazzeri, M., Casiraghi, C., Novoselov, K. S., Geim, A. K., Ferrari, A. C., Mauri, F. (2007) Breakdown of the adiabatic born-oppenheimer approximation in graphene, *Nat. Mater. 6*, 198.

[174] Kim, D.-S., Jeong, Y.-J., Lee, B.-K., Shanmugasundaram, A., Lee, D.-W. (2017)

Piezoresistive sensor-integrated PDMS cantilever: A new class of device for measuring the drug-induced changes in the mechanical activity of cardiomyocytes, *Sens. Actuators, B, 240,* 566.

[175] Gong, S., Schwalb, W., Wang, Y., Chen, Y., Tang, Y., Si, J., Shirinzadeh, B., Cheng, W. (2014) A wearable and highly sensitive pressure sensor with ultrathin gold nanowires, *Nat. Commun. 5,* 3132.

[176] Bae, B., Flachsbart, B. R., Park, K., Shannon, M. A. (2004) Design optimization of a piezoresistive pressure sensor considering the output signal-to-noise ratio, *J. Micromech. Microeng. 14,* 1597.

[177] Yao, H.-B., Ge, J., Wang, C.-F., Wang, X., Hu, W., Zheng, Z.-J., Ni, Y., Yu, S.-H. (2013) A flexible and highly pressure-sensitive graphene polyurethane sponge based on fractured microstructure design, *Adv. Mater.25,* 6692-6698.

[178] Sun, Q., Kim, D. H., Park, S. S., Lee, N. Y., Zhang, Y., Lee, J. H., Cho, K., Cho, J. H. (2014) Transparent, low-power pressure sensor matrix based on coplanar-gate graphene transistors, *Adv. Mater. 26,* 4735-4740.

[179] Wang, Y., Wang, L., Yang, T., Li, X., Zang, X., Zhu, M., Wang, K., Wu, D., Zhu, H. (2014) Wearable and highly sensitive graphene strain sensors for human motion monitoring, *Adv. Funct. Mater. 24,* 4666-4670.

[180] Bae, G.Y., Pak, S.W., Kim, D., Lee, G., Kim, D.H., Chung, Y., Cho, K. (2016) linearly and highly pressure-sensitive electronic skin based on bioinspired hierarchical structural array, *Adv. Mater. 28,* 5300-5306.